Title
Nitrous Acid Formation and Chemistry over Soil and Snow in a Polluted Rural Area

Author
Tsai, Catalina Juiyi

Publication Date
2016

Peer reviewed|Thesis/dissertation

UNIVERSITY OF CALIFORNIA

Los Angeles

Nitrous Acid Formation and Chemistry over Soil and Snow in a Polluted Rural Area

A dissertation submitted in partial satisfaction of the

requirements for the degree Doctor of Philosophy

in Atmospheric and Oceanic Sciences

by

Catalina Juiyi Tsai

2016

ABSTRACT OF THE DISSERTATION

Nitrous Acid Formation and Chemistry over Soil and Snow

in a Polluted Rural Area

by

Catalina Juiyi Tsai

Doctor of Philosophy in Atmospheric and Oceanic Sciences

University of California, Los Angeles, 2016

Professor Jochen Peter Stutz, Chair

Despite of decades of research, the formation mechanism of daytime HONO is still not fully understood and little is known about the daytime behavior of HONO over soil and snow surfaces in polluted rural areas. HONO measurements in two regions heavily affected by oil and gas drilling activities (in Wyoming and Utah) show high levels of daytime HONO (above 500 pptv) during the wintertime. However, questions were raised about the reliability of wintertime HONO observations as recent studies show that many in-situ HONO measurement methods suffer from pernitric acid (PNA) interferences that overestimate HONO concentrations.

The UCLA Long-Path (LP) Differential Optical Absorption Spectroscopy (DOAS) instrument measured HONO and HONO gradients in the Uintah Basin (UB), a

region highly impacted by oil and gas activities. The UCLA LP-DOAS system measured HONO on three light paths covering height intervals from 2 m to 31, 45, and 68 m above ground level (agl). Due to disparate meteorological conditions in 2012 and 2014, HONO was measured over soil in 2012 and over snow in 2014.

HONO mixing ratios averaged 74 ppt in 2012. These levels are lower than HONO measured in polluted urban areas but comparable to levels measured in rural environments. Distinct daytime negative vertical gradients of HONO were observed in 2012, with higher levels of HONO measured on the lower than upper light paths, an indication that HONO had a surface source in 2012. HONO vertical profiles were retrieved using a novel least square minimization approach, in which the average mixing ratios of HONO along the light paths were simulated using a height dependent exponential function. The HONO vertical profiles, together with NOAA micrometeorological data were used to calculate HONO fluxes at 19 m agl. Sunny days hourly average HONO fluxes show that they follow the same trend as solar irradiance, with a maximum of (1.7±0.3) $x10^{10}$ molec. cm^{-2} s^{-1} at noontime, supporting the idea of a photolytic surface HONO source in 2012.

Analysis of HONO flux and photolytic surface HONO sources show that under conditions of high NO_2 levels, conversion of NO_2 on ground surfaces is most likely the source of daytime HONO. In contrast, on days with moderate NO_2 levels, photolysis of surface-adsorbed HNO_3 and nocturnal uptake of HONO followed by daytime acid displacement might play an important role; however, additional measurements are needed to confirm this theory. Comparison of the missing source of HONO ($P_{unknwon}$) and HONO surface flux rate shows that the HONO surface flux rate accounts for (63±32%) of the

$P_{unknown}$ throughout the day indicating that photolytic surface sources of HONO were the dominant sources of HONO in 2012.

HONO mixing ratios measured in 2014 were on average 96 ppt. Comparison of DOAS HONO measurements with four in-situ instruments shows that the DOAS system consistently measured the lowest HONO levels. Preliminary analysis of PNA interferences shows that some in-situ measurements might overestimate HONO concentrations in the presence of PNA (average maximum concentration of 120 ppt measured around noontime), therefore, HONO DOAS were considered the reference measurements in the 2014 study.

2014 HONO vertical profiles also show higher HONO mixing ratios near the surface and a rapid decay of HONO mixing ratios with height. The sunny days hourly average HONO fluxes were also positive with a maximum HONO flux near noontime of $(1.1\pm0.7)x10^{10}$ molec. cm^{-2} s^{-1}. The sunny days hourly average HONO fluxes also follow a similar temporal trend as solar irradiance, further supporting the hypothesis of a photolytic surface HONO source in 2014.

Due to insufficient data, we were not able to determine which photolytic surface HONO formation pathway dominated in 2014. However, we were able to determine that the measured 2014 HONO was most probably formed at the top of the snowpack and not in the firn. This result is supported by the surprisingly similar HONO fluxes measured in 2012 and 2014, which indicate that the HONO formation mechanisms during these two years were probably very similar.

Comparison of the missing source of HONO ($P_{unknwon}$) and HONO surface flux rate shows that HONO surface flux rate accounts for (54±% 15) of the $P_{unknown}$ in the

early morning and noontime, suggesting that HONO sources at noon and early morning are light dependent and are produced on the snow surface.

The dissertation of Catalina Juiyi Tsai is approved.

Saewung Kim

Qinbin Li

Suzanne E. Paulson

Jochen Peter Stutz, Committee Chair

University of California, Los Angeles

2016

TABLE OF CONTENTS

LIST OF FIGURES ..... **x**

LIST OF TABLES ..... **xx**

ACKNOWLEDGEMENT ..... **xi**

VITA ..... **xxii**

Chapter 1 INTRODUCTION **1**

1.1 Winter Ozone Production **1**

1.2 NO_x and VOC emissions in gas drilling regions **3**

1.3 Primary radical production in gas drilling regions **5**

1.4 Nitrous Acid (HONO) **7**

1.4.1 Nighttime HONO formation 8

1.4.2 Nocturnal HONO loss 9

1.4.3 Daytime HONO formation 9

1.4.4 HONO Snow Chemistry 15

1.4.5 HONO Measurement Techniques 18

1.5 Motivation **20**

Chapter 2 METHODOLOGY AND FIELD EXPERIMENTS **22**

2.1 The Uintah Basin Winter Ozone Study (UBWOS) **22**

2.2 Differential Optical Absorption Spectroscopy Technique (DOAS) **24**

2.3 LP-DOAS Instrument **27**

2.3.1 Advantages of using active f LP-DOAS 28

2.4 UCLA LP-DOAS Set Up during UBWOS 2012, 2014 ..... **29**

2.5 DOAS Data Analysis Procedure **30**

2.6 DOAS measurement and evaluation procedure during UBWOS 2012 and UBWOS 2014 33

2.6.1 Example of Analysis Procedure 36

2.6.2 DOAS Error Analysis 37

Chapter 3 HONO VERTICAL PROFILES AND FLUXES RETRIEVAL 39

3.1 HONO Vertical Profiles Retrievals 40

3.2 HONO Flux Calculations 42

3.3 Calculation of unknown HONO source ($P_{unknown}$) 45

Chapter 4 HONO STUDY DURING UBWOS 2012 47

4.1 Introduction 47

4.2 Ancillary Measurements 48

4.2.1 Meteorological (NOAA – Earth System Research Laboratory) and Micrometeorological (NOAA-Physical Science Division) data 48

4.2.2 NO measurements (NOAA – Chemical Science Division) 49

4.2.3 Photolysis rates (NOAA – Chemical Science Division) 49

4.2.4 VOC measurements (NOAA – Chemical Science Division) 49

4.2.5 CH_4, CO, PAN, and HNO_3 measurements (NOAA-Chemical Science Division) 49

4.2.6 Aerosol Number Size Distribution (NOAA – Pacific Marine Environmental Laboratory) 50

4.3 Model Simulations 51

4.3.1 Weather Research and Forecasting model coupled with Chemistry (WRF-Chem) 51

4.3.2 RCAT 8.2 chemical and transport model description 52

4.4 Results 54

4.4.1 Meteorology during UBWOS 2012 54

4.4.2 NO_2, O_3, and HONO light path average mixing ratios 55

4.4.3 Diurnal Profile of NO_2, O_3, and HONO mixing ratios 58
4.4.4 HONO Vertical Profiles 60
4.4.5 HONO Fluxes 62
4.4.6 HONO Daytime sources 64
4.4.7 RCAT 8.2 Model Runs 68
4.5 Discussion 72
4.6 Summary and Conclusion 81
Chapter 5 HONO STUDY DURING UBWOS 2014 82
5.1 Introduction 82
5.2 Ancillary Measurements 85
5.3 Results 85
5.3.1 Meteorology during UBWOS 2014 85
5.3.2 NO_2, O_3, and HONO light path average mixing ratios 87
5.3.3 HONO measurement comparison 96
5.3.4 NO_2, O_3, and HONO mixing ratios light path gradients 102
5.3.5 HONO Vertical Profiles 104
5.3.6 HONO Fluxes 105
5.3.7 HONO Daytime sources 108
5.4 Discussion and Conclusion 112
Chapter 6 CONCLUSION AND OUTLOOK 118
6.1 Conclusion 118
6.2 Outlook 124
REFERENCES 127

LIST OF FIGURES

Figure 1.1 Schematic of photochemical formation of O_3 in the troposphere. 2

Figure 1.2 Maximum 8-hour average O_3 for 2013 measured at Ouray, Utah, a remote site in the Uintah Basin (top panel graph) and measured at Riverside, California, an urban site in the eastern Los Angeles Basin (bottom panel graph). Black dashed line represents the US national ambient air quality standard set in 2008 (75 ppb, 8-hour average). Adapted from Edwards et al. (2014). 2

Figure 1.4 Schematic of proposed daytime HONO sources. 13

Figure 2.1 UB 2011- 2012 monitoring sites (blue dots). Cities and Horse Pool site are labeled. Adapted from Lyman and Shorthill (2013) 23

Figure 2.2 Schematic of UCLA LP-DOAS system used in UBWOS 2012 and 2014..... 28

Figure 2.3 UCLA PL-DOAS system setup in 2012 and 2014. Light paths are shown in solid lines (low in black, middle in blue, and upper in red). The left panel shows the side view of the system with the DOAS instrument represented by the solid square and the retro-reflector arrays represented by the diamonds. Topography under each light path is shown in dashed lines. Map data: Google. The right panel shows the top view of the light paths with retro-reflectors located northwest of the DOAS instrument (white marker with black star). Map data: Google 30

Figure 2.4 Flowchart of DOAS linear-non-linear analysis procedure. Adapted from Platt and Stutz (2008). 33

Figure 2.5 Flowchart of UCLA LP-DOAS measurement and analysis procedure. Adapted from Platt and Stutz (2008). 34

Figure 2.6 Fitting procedure of spectrum measured on 2 February 2012 0243 hours MST using DOASIS. (a) Atmospheric spectrum with broadband features. (b) Fit of NO_2 (red line) superimposed on atmospheric spectrum without broadband features (blue line). (c) Fit of HONO (red line) superimposed on sum of fit HONO and fit residual (blue line); residual spectrum (black) shifted $7.5x10^{-4}$ on the y-axis for better comparison with fitted HONO. 37

Figure 3.1 UCLA LP-DOAS set up in CalNex 2010, Los Angeles (left panel) and in UBWOS 2012/UBWOS 2014, Utah (right panel). Solid lines depict light paths and dashed lines depict topography under the light paths. Map data: Google 40

Figure 3.2 Observed and modeled vertical profiles of daytime HONO. Top left panel shows HONO mixing ratios measured over a forested region (red dots) and potential temperature profile over land (solid lines). The black cross shows the height of the measurement tower. Adapted from Zhang et al. (2009). Top right panel shows average vertical profiles of daytime HONO measured during NACHTT. Adapted from VandenBoer et al. (2013). Lower panel plot shows modeled daytime HONO vertical profiles at 0800, 1200, and 1600 hours CST. The model runs included a photolytic HONO source at the ground and on aerosols. Adapted from Wong et al. (2013). 41

Figure 4.1 Horse Pool site during UBWOS 2012. Left panel shows Horse Pool site looking from South to North. Photo from Lyman and Shorthill (2013). Right panel shows the tent that housed the UCLA LP-DOAS during UBWOS 2012. 48

Figure 4.2 Time Series of Horse Pool wind speed measured 19 m agl by NOAA. Daytime is between 0700 – 1800 hours (red) and nighttime is between 1800 – 0700 hours (black). 54

Figure 4.3 Hourly average meteorological data measured by NOAA: (a) temperature measured at 13 m agl, (b) wind speed measured at 19 m agl, and (c) relative humidity measured at 13 m agl. 55

Figure 4.4 Lower, middle, and upper LP-DOAS light paths averages of (a) NO_2, (b) O_3, and (c) HONO during UBWOS 2012. 56

Figure 4.5 Wind speed and NO_2 mixing ratios measured from 1 February to 3 February 2012. (a) Wind speed measured at 13 m agl. (b) LP-DOAS lower light path NO_2 mixing ratios. 57

Figure 4.6 Hourly average light path averaged mixing ratios of (a) O_3, (b) NO_2, and (c) HONO in the lower (black), middle (blue), and upper (red) light paths throughout the study. Grey shadow shows 1σ spread of average value. 60

Figure 4.7 Sunny days hourly average retrieved vertical profiles of HONO using least square fitting methodology. 62

Figure 4.8 Hourly median (a) friction velocity and (b) Monin Obukhov lengths measured at 16 m agl. 62

Figure 4.9 Calculated (a) eddy diffusivity coefficients, (b) HONO gradients, and (c) HONO flux on 6 February 2012. 64

Figure 4.10 Sunny days hourly average HONO fluxes during UBWOS 2012. 64

Figure 4.11 Sunny days hourly average lower light path HONO (black) and sunny days hourly average $HONO_{ss}$ (HONO steady-state concentration) calculated using equation 1.1. 65

Figure 4.12 Sunny days hourly average HONO rates. HONO production (red line, equation 3.13a), HONO photolysis (green line, equation 3.13b), HONO oxidation (blue line, equation 3.13c), $P_{unknown}$ (black line, equation 3.11) and HONO flux rate (magenta line, equation 3.11). Grey boxes show the time range when the pseudo-steady state assumption was not valid. 66

Figure 4.13 Shows height H (black dot). The vertical profiles are the differences between HONO mixing ratios modeled with HONO surface flux and the HONO mixing ratio modeled without HONO surface flux. 67

Figure 4.14 Modeled Vertical profiles of HONO loss rates (green line: HONO photolysis; blue line: HONO oxidation), HONO production rates (red line: NO oxidation, cyan line: aerosol photolytic pathway), HONO vertical transport (magenta line), and HONO total rate (black line) for 27 January 2016. 68

Figure 4.15 Top panels compare DOAS lower light path HONO mixing ratios with HONO mixing ratios outputted by three 1-D model runs: a base run (blue line and dots), a photolytic run with $\gamma_{NO2} = 1.4x10^{-5}$ (red line and dots), and a HONO flux run (green line and dots). Lower panels compare retrieved HONO fluxes (black) with modeled HONO fluxes at 19 m agl (red). Left panels show results from 4 February 2016 and right panels show results from 27 January 2012. 70

Figure 4.16 Hourly average retrieved vertical profiles of HONO using least square fitting methodology (solid lines) for Feb 7, 2012 near noontime. Modeled vertical profiles of HONO at near noon using 1-D model (dotted lines). 71

Figure 4.17 shows sunny days hourly average HONO fluxes (black dots and line), product of NO_2 mixing ratios measured in the lowest light path and solar radiation (blue line), product of gas-phase nitric acid and UV solar radiation (green line). ... 74

Figure 4.18 Correlation plots of (a) HONO flux vs. [NO_2] x solar radiation and (b) HONO flux vs. [HNO_3] x UV solar radiation..... 75

Figure 4.19 LP-DOAS NO_2 and SO_2 lower light path average mixing ratios. (a) Time series of NO_2 (red line) and SO_2 (black line) from 4 February 2012 to 5 February 2012. (b) Correlation plot between NO_2 and SO_2 with linear fit (red line), fit equation, and R^2 displayed on the plot..... 76

Figure 4.20 Modeled and measured NO_2, HONO, and HNO_3 mixing ratios. NO_2 mixing ratios are shown on the upper panels (a and b), HONO mixing ratios are shown on middle panels (c and d), and HONO fluxes are shown on lower panels (e and f). Left panels show analysis from 4 February 2012 (a, c, and e) and right panel shows analysis from 27 January 2012 (b, d, and f). LP-DOAS lower light path NO_2 and HONO mixing ratios and errors are shown in black, modeled NO_2 and HONO mixing ratios in the lower light path interval using RCAT 8.2 base run are shown in blue, HONO flux run results are shown in green, photolytic run results are shown in red (with NO_2 uptake coefficient of $1x10^{-6}$ for 4 February and $1.4x10^{-5}$ for 27 January). HNO_3 mixing ratios measured by NOAA are shown in magenta lines on the upper panels plots (a and b). 78

Figure 5.1 Left panel shows comparison of the concentration of HONO measured in 2012 and 2013 at Horse Pool site. Middle and right panels show diurnal variations of HONO in 2012 (middle panel) and 2013 (right panel) at Horse Pool site. Adapted from Stoeckenius and McNally (2014). 83

Figure 5.2 Left photo shows Horse Pool site during UBWOS 2014 looking from North to South (left panel). Right photo shows the trailer that housed the UCLA LP-DOAS in 2014..... 85

Figure 5.3 Time series of snow depth (blue line), total UV radiation (sum of upwelling and downwelling UV-A and UV-B) radiation (red line), and average UB-A and UV-B albedo (green line) during winter 2013-2014 at Horse Pool site. Adapted from Stoeckenius (2015)..... 86

Figure 5.4 Hourly average meteorological data measured during UBWOS 2014 at 10 m agl (shown in red) and UBWOS 2012 measured at 9 m agl (shown in black). (a) shows temperature (K), (b) shows wind speed (m s^{-1}), and (c) shows relative humidity. 87

Figure 5.5 LP-DOAS lower light path time series of (a) NO_2, (c) O_3, and upper light path time series of (e) HONO measured during UBWOS 2014. Hourly average mixing ratios of (b) NO_2, (d) O_3, and (f) HONO measured during UBWOS 2014 on the lowest light path (NO_2 and O_3) and upper light path (HONO). Empty circles in plot (a) represent the NO_2 mixing ratios that correlate with SO_2 peaks measured on the lower light path. Empty circles in plot (b) show the hourly average NO_2 mixing ratios calculated without the NO_2 mixing ratios that correlated with SO_2. 88

Figure 5.6 Time series of SO_2, NO_2, 8-hr average O_3, CO_2, and wind speed measured at the Horse Pool site. (a) LP-DOAS lower light path SO_2 mixing ratios in red and NO_2 mixing ratios in black. (b) LP-DOAS lower light path 8-hr average O_3 mixing in black. Red line represents the NAAQS O_3 standard (75 ppb) of winter of 2014. (c) CO_2 mixing ratios measured by NOAA. (d) Wind speed measured at 9 m agl..... 90

Figure 5.7 NO_2 (a and b), O_3 (c and d), wind speed (e and f), and wind directions (g and h) measured at the Horse Pool site on 27 January 2014 (left panels) and 4 February 2014 (right panels). 91

Figure 5.8 LP-DOAS lower light path time series of (a) NO_2, (c) O_3, and (e) HONO measured during UBWOS 2012 (black) and UBWOS 2014 (red). Hourly average mixing ratios of (b) NO_2, (d) O_3, and (f) HONO measured during UBWOS 2012 and 2014 on the lowest light path. Empty circles (a) represent NO_2 mixing ratios that correlate with SO_2 mixing ratios measured by LP-DOAS on the lower light path. Empty circles in plot (b) show the hourly average NO_2 mixing ratios calculated without the empty circles shown in plot (a). 92

Figure 5.9 Average NO_x mixing ratios measured at the Horse Pool site versus time of day for the three UBWOS intensive studies. Adapted from Stoeckenius (2015)..... 93

Figure 5.10 Time series of LP-DOAS measurements of HONO on the (a) lower light path, (c) middle light path, and (e) upper light path. Filled circles represent outliers, open circles represent positive HONO and negative data within the 2 σ error of the respective measurement. The red line shows zero. Hourly average HONO mixing ratios calculated from (b) lower, (d) middle, and (f) upper light paths data sets in

which outliers were removed (black markers and line) or outliers were substituted by zero (red markers and line). 95

Figure 5.11 The Horse Pool HONO measurement site as configured during the 2014 intensive study. Adapted from Stoeckenius (2015). 97

Figure 5.12 Comparison of the four in situ and DOAS upper light path HONO measurements in the 'common period'. 98

Figure 5.13 Correlation of the four in situ with DOAS lower light path HONO measurements in the 'common period'. 98

Figure 5.14 Timelines of the short and long inlets tests performed with the iCIMS for (a) HONO and (b) HO_2NO_2. Adapted from Stoeckenius (2015). 99

Figure 5.15 Correlation plot between daytime ACIMS HONO and iCIMS PNA in UBWOS 2014. Adapted from Stoeckenius (2015). 100

Figure 5.16. Left panel shows the diurnal profile of ACIMS HONO (pink) and DOAS HONO (green). Right panel shows the diurnal profile of ACIMS HONO minus PNA (assuming 1:1 PNA to HONO conversion) in pink, compared to DOAS HONO (green). Adapted from P. Veres, personal communication, 26 November 2014. ... 100

Figure 5.17 Left panel shows average diurnal profiles of HONO observed by the LOPAP (in purple), and PNA observed by the iCIMS (yellow). Right panel shows diurnal profile of corrected ACIMS HONO, corrected LOPAP HONO, and DOAS HONO (green). The corrected ACIMS and LOPAP HONO were determined by subtracting PNA to HONO concentrations. Adapted from P. Veres, personal communication, 26 November 2014. 101

Figure 5.18 Hourly average light path average mixing ratios of (a) O_3, (b) NO_2, and (c) HONO in the lower (black), middle (blue), and upper (red) light paths throughout the study. 102

Figure 5.19 Hourly average light path averages mixing ratios of HONO in the lower (black), middle (blue), and upper (red) light paths measured in 2012 (empty circles) and 2014 (filled circles). 103

Figure 5.20 Sunny days hourly average retrieved vertical profiles of HONO using least square fitting methodology (section 3.1). 104

Figure 5.21 Hourly median micrometeorological data measured at 16 m agl: (a) Friction velocity, and (b) Monin Obukhov lengths. 106

Figure 5.22 HONO fluxes on 24 January 2014. Top panel shows eddy diffusivity coefficients calculated using equation 3.5, middle panel shows HONO gradients calculated using equation 3.8, and lower panel shows HONO fluxes calculated using equation 3.4. 107

Figure 5.23 Sunny days hourly average HONO fluxes in 2014 (black dots and line) and 2012 (red dots and line). 108

Figure 5.24 HONO mixing ratios measured on the lower light path (black dot and line) and calculated $HONO_{ss}$ (red line and dots). 108

Figure 5.25 Sunny days hourly average 2014 HONO rates. HONO production (red line, equation 3.13a), HONO photolysis (green line, equation 3.13b), HONO oxidation (blue line, equation 3.13c), $P_{unknown}$ (black line, equation 3.11) and HONO flux rate (magenta line, equation 3.11). Grey box highlights the time when HONO lifetimes are too long to assume pseudo steady state conditions. 110

Figure 5.26 Comparison of 2012 (red dots and line) and 2014 (black dots and line) sunny days hourly average (a) eddy diffusivity coefficients and (b) HONO photolysis rates. 111

Figure 5.27 Height H for 2012 (black dot) and for 2014 (red dot). The vertical profiles are the differences between HONO mixing ratios modeled with HONO surface flux and the HONO mixing ratios modeled without HONO surface flux. 112

Figure 5.28 Sunny days hourly average HONO fluxes (black dots and line), product of NO_2 mixing ratios measured in the lowest light path and solar radiation (red line), product of gas-phase nitric acid and UV solar radiation (green line), product of gas-phase nitric acid, UV solar radiation, and wind speed squared. 114

Figure 5.29 Comparison of model predicted HONO for three day model run (10 – 13 June 2008) for the base run ($3.3x10^{-4}$ of Br^- and $8.8x10^{-3}$ NO_3^- in QLL), noNit (no nitrate in QLL), and noBro (no bromine in QLL) cases with mist chamber measurements of soluble nitrite with one inlet 1.5 m above the snow surface (upper panel) and one inlet 10 cm below the snow surface (lower panel). Adapted from Thomas et al. (2012) 116

Figure 5.30 Correlation plot of (a) sunny days hourly average HONO flux vs. [NO_2] x solar radiation, (b) sunny days hourly average HONO flux vs. [$HONO_3$] x UV solar radiation, and (c) sunny days hourly average HONO flux vs. [HNO_3] x UV solar radiation x u^2. 117

LIST OF TABLES

Table 2.1 Fit parameters for retrieval of gases during UBWOS 2012 and UBWOS 2014.....35

Table 3.1 Rate coefficient and rate coefficient uncertainty for HONO formation and at 275 K ...46

Table 5.1 Summary of the HONO measurements during UBWOS 2014.....97

ACKNOWLEDGEMENTS

I would like to express my gratitude to my advisor Prof. Stutz for his continuous support of my research in atmospheric chemistry and air pollution. His patience, immense knowledge, and guidance helped me to develop the scientific skills needed to write this thesis. Besides my advisor, I would like to thank the rest of my thesis committee: Prof. Suzanne E. Paulson, Prof. Qinbin, Li, and Prof. Saewung, Kim for their encouragement and support. I also owe acknowledgement to Dr. James Roberts, Dr. Patrick Veres, Dr. Ahmadov, Dr. Hans Osthoff, and Dr. Robert Zamora for providing collaboration in my research. I thank the members in my research group, Dr. Fedele Colosimo, Ross Cheung, Dr. Katja Grossmann, Katie Tuite, Nathaniel Brockway, Dr. Steve Hurlock, James Festa, Dr. Clare Wong, and Dr. Olga Pikelnaya for the stimulating discussions and their companionship. Last but not the least, I would like to thank my parents, my brother, and my good friends Cecilia Lin, Ayesha Bulegoda, Daniel Sun, and Sakar Shivakoti for their support throughout this thesis.

VITA

2008	B.S., Chemistry
	University of California, Los Angeles
2010 – present	Graduate Student Researcher
	Department of Atmospheric and Oceanic Sciences
	University of California, Los Angeles
2011	M.S., Atmospheric and Oceanic Sciences
	University of California, Los Angeles

PUBLICATIONS

Edwards, P.M., Brown, S.S., Roberts, J.M., Ahmadov, R., Banta, R.M., DeGouw, J.A., Dubé, W.P., Field, R.A., Flynn, J.H., Gilman, J.B., Graus, M., Helmig, D., Koss, A., Langford, A.O., Lefer, B.L., Lerner, B.M., Li, R., Li, S.-M., McKeen, S.A., Murphy, S.M., Parrish, D.D., Senff, C.J., Soltis, J., Stutz, J., Sweeney, C., Thompson, C.R., Trainer, M.K., **Tsai, C.,** Veres, P.R., Washenfelder, R.A., Warneke, C., Wild, R.J., Young, C.J., Yuan, B., Zamora, R., 2014. High winter ozone pollution from carbonyl photolysis in an oil and gas basin. Nature 514, 351–354. doi:10.1038/nature13767

Mielke, L.H., Stutz, J., **Tsai, C**., Hurlock, S.C., Roberts, J.M., Veres, P.R., Froyd, K.D., Hayes, P.L., Cubison, M.J., Jimenez, J.L., Washenfelder, R.A., Young, C.J., Gilman, J.B., de Gouw, J.A., Flynn, J.H., Grossberg, N., Lefer, B.L., Liu, J., Weber, R.J., Osthoff, H.D., 2013. Heterogeneous formation of nitryl chloride and its role as a nocturnal NOx reservoir species during CalNex-LA 2010. J. Geophys. Res. Atmos. 118, 10,638–10,652. doi:10.1002/jgrd.50783

Pikelnaya, O., Flynn, J.H., **Tsai, C.,** Stutz, J., 2013. Imaging DOAS detection of primary formaldehyde and sulfur dioxide emissions from petrochemical flares. J. Geophys. Res. 118, 1–13. doi:10.1002/jgrd.50643

Pinto, J.P., Dibb, J., Lee, B.H., Rappenglück, B., Wood, E.C., Levy, M., Zhang, R.-Y., Lefer, B., Ren, X.-R., Stutz, J., **Tsai, C.,** Ackermann, L., Golovko, J., Herndon, S.C., Oakes, M., Meng, Q.-Y., Munger, J.W., Zahniser, M., Zheng, J., 2014.

Intercomparison of field measurements of nitrous acid (HONO) during the SHARP campaign. J. Geophys. Res. Atmos. 119, 5583–5601. doi:10.1002/2013JD020287

Pusede, S.E., VandenBoer, T.C., Murphy, J.G., Markovic, M.Z., Young, C.J., Veres, P., Roberts, J.M., Washenfelder, R.A., Brown, S.S., Ren, X., **Tsai, C.,** Stutz, J., Brune, W.H., Browne, E.C., Wooldridge, P., Graham, A.R., Weber, R., Goldstein, A.H., Dusanter, S., Griffith, S., Stevens, P.S., Lefer, B., Cohen, R.C., 2015. An atmospheric constraint on the NO2 dependence of daytime near-surface nitrous acid (HONO). Environ. Sci. Technol. 49, 12774–12781. doi:10.1021/acs.est.5b02511

Ren, X., van Duin, D., Cazorla, M., Chen, S., Mao, J., Zhang, L., Brune, W.H., Flynn, J.H., Grossberg, N., Lefer, B.L., Rappenglück, B., Wong, K.W., **Tsai, C.,** Stutz, J., Dibb, J.E., Jobson, B.T., Luke, W.T., Kelley, P., 2013. Atmospheric oxidation chemistry and ozone production: Results from SHARP 2009 in Houston, Texas. J. Geophys. Res. Atmos. 118, 5770–5780. doi:10.1002/jgrd.50342

Tsai, C., Wong, C., Hurlock, S., Pikelnaya, O., Mielke, L.H., Osthoff, H.D., Flynn, J.H., Haman, C., Lefer, B., Gilman, J., de Gouw, J., Stutz, J., 2014. Nocturnal loss of NOx during the 2010 CalNex-LA study in the Los Angeles Basin. J. Geophys. Res. Atmos. 119, 13004–13025. doi:10.1002/2014JD022171

Wong, K.W., **Tsai, C.,** Lefer, B., Grossberg, N., Stutz, J., 2013. Modeling of daytime HONO vertical gradients during SHARP 2009. Atmos. Chem. Phys. 13, 3587–3601. doi:10.5194/acp-13-3587-2013

Wong, K.W., **Tsai, C.,** Lefer, B., Haman, C., Grossberg, N., Brune, W.H., Ren, X., Luke, W., Stutz, J., 2011. Daytime HONO vertical gradients during SHARP 2009 in Houston, TX. Atmos. Chem. Phys. Discuss. 11, 24365–24411. doi:10.5194/acpd-11-24365-2011

Ye, C., Zhou, X., Pu, D., Stutz, J., Festa, J., Spolaor, M., **Tsai, C.,** Cantrell, C., Mauldin III, R.L., Campos, T., Weinheimer, A., Hornbrook, R.S., Apel, E.C., Guenther, A., Kaser, L., Yuan, B., Karl, T., Haggerty, J., Hall, S., Ullmann, K., Smith, J.N., Ortega, J., Knote, C., 2016. Rapid cycling of reactive nitrogen in the marine boundary layer. Nature 532, 489–491. doi:10.1038/nature17195

Young, C.J., Washenfelder, R.A., Roberts, J.M., Mielke, L.H., Osthoff, H.D., **Tsai, C.,** Pikelnaya, O., Stutz, J., Veres, P.R., Cochran, A.K., VandenBoer, T.C., Flynn, J., Grossberg, N., Haman, C.L., Lefer, B., Stark, H., Graus, M., de Gouw, J., Gilman, J.B., Kuster, W.C., Brown, S.S., 2012. Vertically resolved measurements of nighttime radical reservoirs in Los Angeles and their contribution to the urban radical budget. Environ. Sci. Technol. 46, 10965–10973. doi:10.1021/es3022

Chapter 1 INTRODUCTION

1.1 Winter ozone production

Ozone (O_3) is an air pollutant that has serious repercussions on human health. Breathing ozone can result in reduction of lung function, inflammation of airways, and can cause respiratory symptoms such as throat irritation, shortness of breath, and chest tightness (http://www3.epa.gov/ozonepollution/health.html). Ozone's national ambient air quality standard (8-hour average) was revised in October 2015 and reduced from 75 ppb to 70 ppb.

Ozone pollution has traditionally been considered a summertime, urban phenomenon (Logan, 1989; Trainer et al., 1987). Its precursors, NO_x (NO_2 + NO) and VOCs (Volatile Organic Carbons), are predominantly emitted in urban areas as byproducts of fossil fuel combustion and evaporation of chemicals like solvents. Photolysis of NO_2 produces NO and atomic oxygen (O^3P) (R1 in Figure 1.1), which reacts with molecular oxygen to form O_3 (R2 in Figure 1.1). No net production of O_3 results from these reactions as NO reacts with O_3 to regenerate NO_2 (R3 in Figure 1.1). However, in the presence of VOCs, radical catalyzed oxidation of VOCs converts NO into NO_2 without destroying O_3 resulting in a net increase of O_3 concentrations (Figure 1.1). Hence, radicals and their formation processes play an important role in the production of tropospheric O_3. In the summertime, longer sunlit hours and greater actinic flux enhance photolytic production of OH explaining the high levels of O_3 observed in polluted urban areas during the summer (Figure 1.2, lower panel).

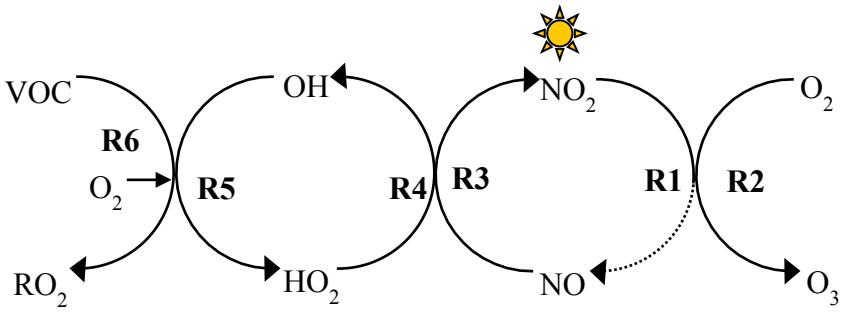

Figure 1.1 Schematic of photochemical formation of O_3 in the troposphere.

However, recent field studies in rural areas impacted by oil and gas activities in the western United States show unusual high levels of O_3 (up to 150 ppb) during the winter (Figure 1.2, upper panel) (Edwards et al., 2014; Schnell et al., 2009). These high levels of O_3 are comparable to summertime O_3 levels observed in polluted urban environments (Figure 1.2, lower panel plot).

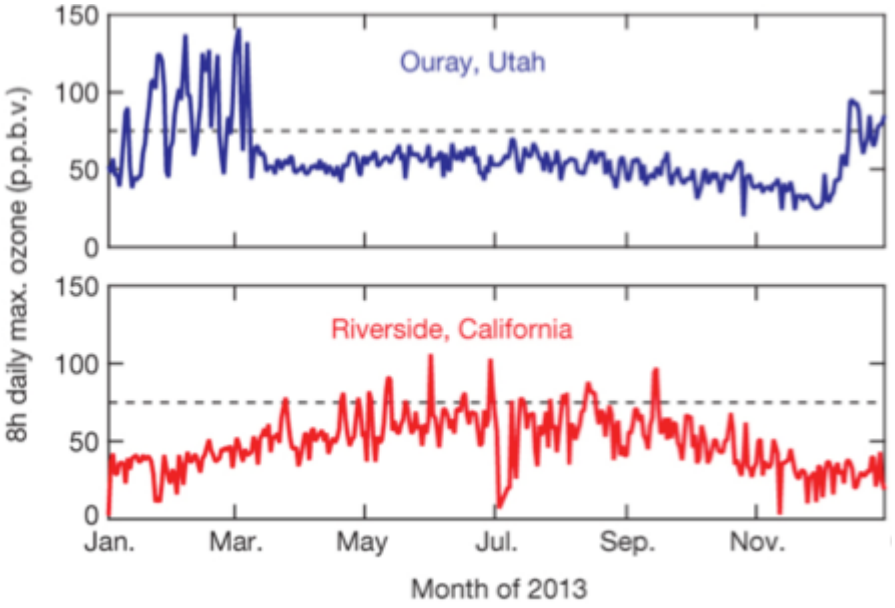

Figure 1.2 Maximum 8-hour average O_3 for 2013 measured at Ouray, Utah, a remote site in the Uintah Basin (top panel graph) and measured at Riverside, California, an urban site

in the eastern Los Angeles Basin (bottom panel graph). Black dashed line represents the US national ambient air quality standard set in 2008 (75 ppb, 8-hour average). Adapted from Edwards et al. (2014).

Studies in the Upper Green River Basin (UGRB) in southwestern Wyoming and the Uintah Basin (UB) in northeast Utah show that high levels of winter ozone were only observed in the presence of snow-covered ground. Cold temperatures and significant snow cover can cause strong temperature inversions that decrease atmospheric mixing and accumulate ozone and its precursors in a shallow layer near the ground. Temperature inversions over snow occur when the high albedo of snow inhibits surface heating, and together with the efficient IR emission by snow, lead to a cooling of the surface compared to the air above. Martin et al. (2011) measured mixed layer heights of 20-80 m during ozone-producing conditions in the UB in winter of 2010-2011. The presence of snow also increases UV actinic flux, which enhances the photochemical formation of O_3. Martin et al. (2011) reported an increase of UV flux by a factor of about 1.6 to 1.9 in the UB during snow cover periods, making the radiative flux comparable to levels found typically in the tropics (Simpson et al., 2002).

1.2 NO_x and VOC emissions in gas drilling regions

Similar to summer O_3 episodes in polluted urban areas; winter ozone formation is the result of photochemical reactions of VOCs and NO_x. VOC data collected in the UB (Lyman and Shorthill, 2013) show that in contrast to urban areas, but similar to other areas with significant oil and gas extraction activities, VOC were weighted towards light

alkanes (Figure 1.3). The most abundant VOC species in the UB were alkanes, followed by aromatic VOCs and minor amount of alkene (relative to alkanes and aromatics) (Figure 1.3). Despite of the greater reactivity of aromatics and alkenes, alkane contributed more to ozone formation than the other VOC species (Stoeckenius and McNally, 2014).

Analysis of VOCs measured in the UB indicates that the majority of VOCs are from natural gas releases from venting, leaks, and other fugitive sources. The equipment required for hydraulic fracturing operations releases VOCs at each stage of production (Stoeckenius, 2015). The equipment used at the exploration, production, and delivery stages also emits NO_x (Goldan et al., 2004). According to an emission inventory for winter 2011-2012 in the UB, oil and gas-related emissions account for 98-99% (9200 tons $month^{-1}$) of VOC emissions and 58-62% (1000 – 1200 tons $month^{-1}$) of NO_x emissions in the basin (Lyman and Shorthill, 2013).

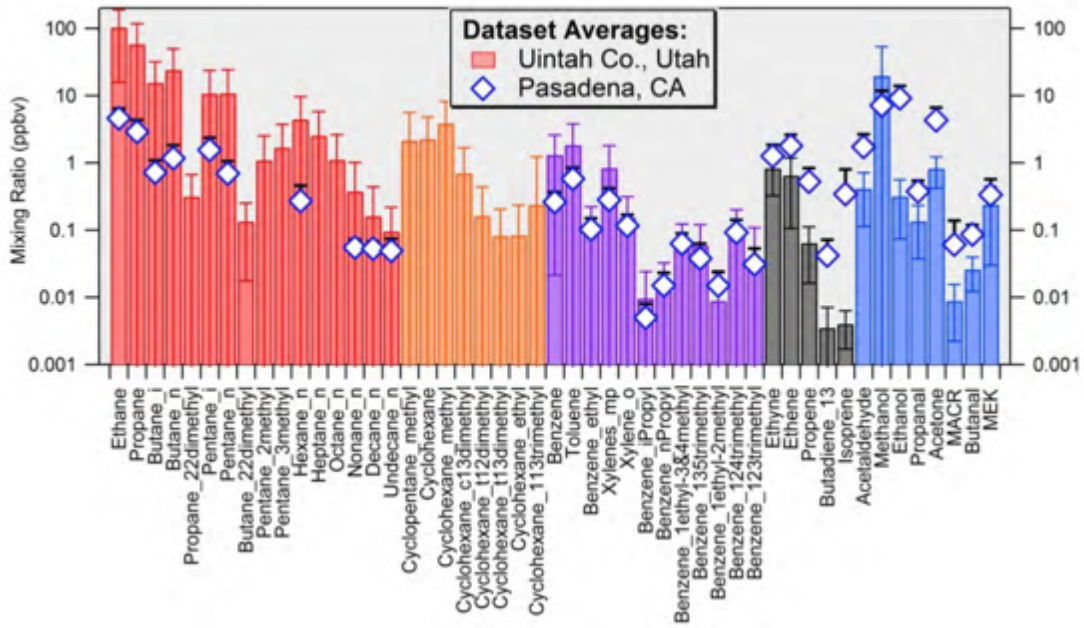

Figure 1.3 Mean mixing ratios of VOCs collected using NOAA GCMS from 15 January 2012 to 29 February 2012 at Horse Pool and from May 2010 to June 2010 at Pasadena, California. Adapted from (Lyman and Shorthill, 2013)

1.3 Primary radical production in gas drilling regions

The main production pathway of radicals in the troposphere is the photolysis of O_3 (R7) which yields a small amount of electronically excited oxygen molecules ($O(^1D)$) that can react with water vapor to produce two hydroxyl radicals (OH) (R8) (Levy, 1972). Other primary radical production mechanisms in the troposphere are the photolysis of formaldehyde (HCHO) (R9), photolysis of nitryl chloride ($ClNO_2$) (R10), photolysis of nitrous acid (HONO) (R11), and reaction of O_3 with alkenes (R12)

$$O_3 \xrightarrow{h\nu(\lambda \leq 340nm)} O_2 + O(^1D) \qquad (R7)$$

$$O(^1D) + H_2O \rightarrow 2\,OH \qquad (R8)$$

$$HCHO \xrightarrow{h\nu, O_2} CO + HO_2 + HO_2 \qquad (R9)$$

$$ClNO_2 \xrightarrow{h\nu} NO_2 + Cl^{\cdot} \qquad (R10)$$

$$HONO \xrightarrow{h\nu\ (\lambda \leq 400\ nm)} NO + OH \qquad (R11)$$

$$O_3 + alkene \rightarrow \cdots \rightarrow OH + products \qquad (R12)$$

HCHO is produced mainly through the gas phase oxidation of a broad variety of VOCs (Fried et al., 2003). Other sources of HCHO include its primary emissions from incomplete combustion (Olaguer et al., 2009) and snowpack photochemistry (Grannas et al., 2007). The photolysis of $ClNO_2$ produces chlorine (Cl) radical, a highly reactive

molecule which fast reactions with hydrocarbons can start the HO_x radical chain mentioned previously. $ClNO_2$ is mainly produced by the uptake of N_2O_5 onto chlorine containing aerosol (Simon et al., 2009). Elevated levels of tropospheric O_3 makes O_3-alkene reactions a significant removal process for alkenes in the lower atmosphere. The first step in the O_3-alkene reaction is the addition of O_3 to the double bond to form a primary ozonide, which is not stable and splits to give a carbonyl compound and Criegee intermediate. The Criegee intermediate eliminates its excess energy by stabilizing or decomposing. In the case of O_3 reaction with highly branched alkenes, the OH yield approach to unity (Paulson and Orlando, 1996). Paulson and Orlando (1996) predicted that O_3-alkene reaction contributed ~10-15% to the production of total radicals in forested rural site in the southeastern United States. Their and other studies argue that O_3-alkene reactions could be an important OH source at times when photolytic sources of OH are minimal (Bey et al., 1997; Paulson and Orlando, 1996).

Ozone photolysis (R7), which is the main radical production mechanism in the formation of summertime ozone, usually plays a minor role in mid-latitude winter. Both ultraviolet light and water vapor are less abundant in winter, leading to a 15-60-fold decrease in primary OH production through this mechanism (Edwards et al., 2014). Studies in remote polar region identified a number of processes that could enhance production of radical precursors over snow and could be of importance in these regions. These processes include the formation of atmospheric HCHO from oxidation of organics in the snow (Barret et al., 2011; Jacobi et al., 2002) and the release of HONO (Honrath et al., 2002; Zhou et al., 2001) originated from the photolysis of snow nitrate. Sensitivity analyses of winter ozone formation in the UGRB (Carter and Seinfeld, 2012) show that

daytime production of HONO via heterogeneous reaction on the snow could contribute significantly to ozone production under VOC limited conditions. This hypothesis was supported by measurements of elevated HONO mixing ratios (up to 1.5 ppb of HONO in the morning and about 200 ppt during the day) in Wyoming during a winter field experiment in 2011 (Rappenglueck et al., 2014). This thesis focuses on the role of HONO in the production of wintertime O_3 therefore an overview of HONO is given in the following sections.

1.4 Nitrous Acid (HONO)

HONO has been actively studied since its detection in 1979 (Perner and Platt, 1979) due to its impact on photo-oxidation processes in the lower atmosphere. It has long been established that the photolysis of nitrous acid (HONO) is an important source of OH during the day, especially in the early morning when other OH sources, such as photolysis of ozone and formaldehyde, are still small (Alicke et al., 2003; Alicke et al., 2002; Harrison et al., 1996). Observations made in urban and rural areas in the spring-summer season show that morning HONO photolysis can contribute up to 55% to the daytime radical budget (Alicke et al., 2003; Elshorbany et al., 2009; Kleffmann et al., 2005; Volkamer et al., 2010; Young et al., 2012). After sunrise, HONO mixing ratios tend to decrease rapidly due to photolysis and enhanced vertical mixing. In the past, it was believed that HONO reaches pseudo-steady state during the day; however, field observations have shown that daytime HONO mixing ratios tend to be 10 to 100 times higher than the pseudo-steady state HONO concentrations ($[HONO]_{SS}$) (Elshorbany et al., 2012; Stark et al., 2011; Wong et al., 2012; Zhou et al., 2011) pointing toward the

existence of unknown sources of daytime HONO in the atmosphere. A number of gas-phase (Bejan et al., 2006; Li et al., 2008), aerosol (Zhou et al., 2003), and ground surface (George et al., 2005; Su et al., 2011) chemistry mechanisms have been proposed to explain the higher than expected levels of daytime HONO, but a conclusive mechanism has not yet been found.

The following sections review the current understanding of HONO chemistry in various environments and discuss the current analytical methods to measure atmospheric HONO concentrations.

1.4.1 Nighttime HONO formation

Measurements show that HONO accumulates readily during the night and decreases during the day. In the absence of light, the dominant HONO formation process is the heterogeneous disproportionation of NO_2:

$$2\,NO_2 + H_2O \xrightarrow{surface} HONO + HNO_3 \qquad (R13)$$

This reaction has been studied on a variety of surfaces (Lammel and Cape, 1996) and was found to be first order with respect to both NO_2 and water vapor (Pitts et al., 1984; Sakamaki and Akimoto, 1988; Sakamaki et al., 1983; Svensson et al., 1987). Gutzwiller (2002) argued that heterogeneous reaction of NO_2 with adsorbed hydrocarbons is also important under atmospheric conditions:

$$2\,NO_2 + HC_{red} \rightarrow HONO + HC_{ox} \qquad (R14)$$

Other dark HONO formation reactions have been proposed (AndresHernandez, 1996; Calvert et al., 1994; Saliba et al., 2001) but have found to be irrelevant in the real atmosphere (Gustafsson et al., 2008; Kleffmann et al., 1998; Svensson et al., 1987).

1.4.2 Nocturnal HONO loss

Field observations have shown that while the formation rate of HONO is constant during the night, surface-level HONO increases more slowly later at night (Stutz, et al., 2002), suggesting a loss process that establishes an approximate steady state (VandenBoer et al., 2013; VandenBoer et al., 2014). By using high resolution vertical profiles of HONO, VandenBoer et al. (2013) shows that significant amounts of HONO deposit to the ground at night with ground uptake coefficients of HONO ($\gamma_{(HONO,ground)}$) in the $2x10^{-5}$ – $2x10^{-4}$ range. These uptake coefficients are comparable to those reported by Donaldson et al. (2014) ($2.5x10^{-4}$) and Wong et al. (2013) ($6x10^{-5}$). Donaldson et al. (2014) found that $\gamma_{(HONO, ground)}$ decrease with increasing RH, reporting $\gamma_{(HONO, ground)}$ of $(2.5\pm0.4)\ x10^{-4}$ under dry conditions to $(1.1\pm0.4)\ x10^{-5}$ at 80% RH.

1.4.3 Daytime HONO formation

The established formation and loss processes of HONO in the daytime atmosphere are the reaction of OH and NO (R15), photolysis of HONO (R11), and oxidation of HONO (R16):

$$OH + NO \xrightarrow{M} HONO \qquad (R15)$$

$$HONO + OH \rightarrow H_2O + NO_2 \qquad (R16)$$

Comparison between the room temperature rate constant of R16 ($4.5x10^{-12}$ cm^3 $molecule^{-1}$ s^{-1} (DeMore et al., 1997) and the first-order photolysis rate constant of HONO photolysis (~$1.3x10^{-3}s^{-1}$ at solar zenith angle of 40° (R8) (Calvert et al., 1994) show that, even at an OH concentration of $1x10^7$ radicals cm^{-3}, R16 is much slower than R11 leading to the conclusion that daytime HONO's main loss pathway is its photolysis.

Until recently it was believed that HONO reaches a pseudo-steady state (HONOss) with its gas-phase formation reaction and photolysis rate:

$$[HONO]_{SS} = \frac{k_{OH+NO}[NO][OH]}{j_{HONO}+k_{HONO+OH}[OH]} \quad \text{(equation 1.1)}$$

However, numerous studies have shown that measurements of daytime HONO mixing ratios were often one to two orders of magnitudes higher than the calculated $[HONO]_{SS}$ (Elshorbany et al., 2012; Wong et al., 2012; Zhou et al., 2011), pointing toward the existence of unknown sources of daytime HONO in the atmosphere. Numerous formation mechanisms based on laboratory and field experiments were proposed to explain this higher than expected level of daytime HONO. The suggested gas phase formation pathways of HONO include the dissociation of HONO from photolyzed ortho-nitrophenols (pathway 1 in Figure 1.4) (Bejan et al., 2006) and reaction of electronically excited NO_2 with water vapor (Li et al., 2008). Reaction of electronically excited NO_2 with water vapor has shown to be a two-photon process with little relevance under atmospheric conditions (Soergel et al., 2011; Wong et al., 2012). Laboratory experiments suggest that photolysis of ortho-nitrophenols can contribute to the formation of daytime HONO in more polluted urban atmospheres (Bejan et al., 2006) however this mechanisms has not yet been evaluated via direct measurement.

Studies have shown that solar irradiance enhances heterogeneous NO_2 to HONO conversion on surfaces (pathway 3 in Figure 1.4) such as TiO_2 (Bedjanian and El Zein, 2012; Langridge et al., 2009; Ndour et al., 2008) , soot (Ammann et al., 1998; Aubin and Abbatt, 2007; Gerecke et al., 1998; Khalizov et al., 2010), humic acid (Bartels-Rausch et al., 2010; Stemmler et al., 2006; Stemmler et al., 2007) and organic films (George et al., 2005; Gutzwiller et al., 2002). George et al. (2005) and Stemmler et al. (2006) found that

NO_2 conversion to HONO on aromatic compounds was 1 – 2 order of magnitude greater than dark reaction when irradiated with light between 300 – 420 nm. They also conclude that formation of HONO occurs not only when irradiated with light in the UV-A spectral region but also when irradiated with visible light, in contrast to the photolysis of nitrate, which was proposed to be a daytime source of HONO:

$$NO_2 + organics \xrightarrow{h\nu} + HONO + products \qquad (R17)$$

Based on Stemmler et al. (2006) laboratory observations, formation of HONO from NO_2 to HONO conversion on surface adsorbed humic acid is first order in NO_2 at low NO_2 mixing ratios and linearly dependent on irradiance:

$$P_{HONO}\ \alpha\ surface\ area * [NO_2] * Irradiance \qquad \text{(equation 1.2)}$$

An alternate proposed daytime HONO source is the photolysis of surface adsorbed HNO_3 (pathway 2 in Figure 1.4) (Zhou et al., 2003). The work of Zhou et al. (2002, 2003) show that the production of HONO through photolysis of surface adsorbed HNO_3 is greatly enhanced by the presence of water. Their study show that between RH of 20% and 80% the production yield of HONO is almost independent of RH suggesting that the photolysis of surface adsorbed HNO_3 is the rate-limiting step in the process leading to HONO formation. They show a linear relationship between HONO production rate and the amount of HNO_3 adsorbed on the surface. The proposed mechanism for HNO_3 photolysis on surfaces (Zhou et al., 2002, 2003) is similar to that in aqueous nitrate photolysis (Mack and Bolton, 1999) :

$$HNO_3(ads) + h\nu \longrightarrow [HNO_3]^*(ads) \qquad (R18)$$

$$[HNO_3]^*(ads) \longrightarrow HNO_2(ads) + O(^3P)(ads) \qquad (R19)$$

$$[HNO_3]^*(ads) \longrightarrow NO_2(ads) + OH \qquad (R20)$$

Under humid conditions, the produced NO_2(ads) may react with surface adsorbed H_2O to produce HONO(ads). The HONO(ads) may desorb from the surface and be released into the gas phase. Their study shows that the average HONO production rate normalized to the amount of adsorbed HNO_3 on surface is about two orders of magnitude greater than the nitrate photolysis rate in aqueous solutions (Jankowski et al., 1999; Mack and Bolton, 1999) and HNO_3 photolysis rate in the gas phase (Finlayson-Pitts and Pitts, 2000).

Su et al. (2011) show in their study that soil nitrite can serve as a strong source of atmospheric HONO. They suggest that nitrite produced by biological nitrification and denitrification processes can undergo reversible acid-base reaction and partitioning between air and the aqueous phase of humid soil to produce HONO (pathway 4 in Figure 1.4). Their chamber experiment shows that fertilized soils with low pH are particularly strong sources of HONO, thus this pathway is expected to be important in environments with strong agricultural and land-use changes.

VandenBoer et al. (2012, 2014, 2015) proposed that HONO deposited on the surface during the night could act as a HONO source the following day. The displacement of HONO from surface nitrate by atmospheric strong acids, such as HCl and HNO_3, has the potential of being an important daytime HONO source (specially in the mid-to-late day).

The aforementioned daytime HONO formation pathways are shown in Figure 1.4 with non-photolytic HONO sources in purple arrows and the photolytic HONO sources in yellow arrows. The red show the fate of NO_2 and HNO_3 as a precursor of HONO. Despite of years of research, the daytime HONO formation mechanism is still unknown.

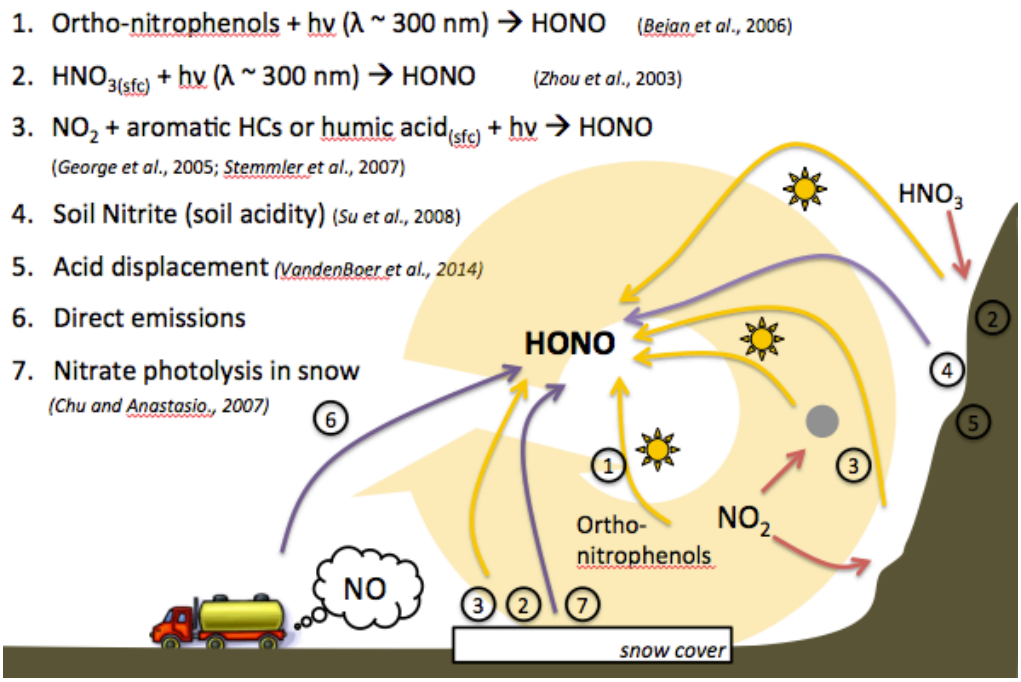

Figure 1.4 Schematic of proposed daytime HONO sources.

The heterogeneous HONO sources, i.e. photolysis on surface adsorbed HNO_3 and photo-enhanced conversion of NO_2 on surfaces can occur both on aerosols and at the ground. A number of studies have evaluated the relative importance of aerosol and ground surfaces in the production of daytime HONO using lab experiments (Broske et al., 2003), HONO vertical profiles (Sörgel et al., 2011; Villena et al., 2011; Wong et al., 2012; Zhang et al., 2009), and fluxes (Ren et al., 2011; Zhou et al., 2011).

Stemmler et al. (2007) and Bröske et al. (2003) found that photo-enhanced conversion of NO_2 on secondary organic aerosols (pathway 3) is most likely not important in the atmosphere, as the uptake coefficients observed in the laboratory are too small. Nevertheless, HONO formation through the aerosol phase cannot be completely excluded, as there might be unrecognized HONO formation mechanisms that involve aerosols.

The vertical distribution of HONO in the daytime boundary layer can be used to determine if the unknown HONO source is formed in the gas-phase, on aerosols, or at the ground. While a ground source of HONO would lead to higher HONO levels near the ground than aloft, HONO formed on aerosols or through gas-phase chemistry in a well mixed daytime boundary layer would have a relatively constant vertical distribution. While some studies did not observed discernable vertical daytime gradients of HONO (Kleffman et al., 2007; Sörgel et al., 2011), others, such as Zhang et al. (2009), Villena et al. (2011), Wong et al. (2012), and Vandenboer et al. (2013), measured negative gradients of HONO during the day, suggesting that daytime production of HONO occurs at the ground and mixed throughout the daytime boundary layer. Zhang et al. (2009) estimated a missing HONO source of ~ 150 ppt h^{-1} in the upper boundary layer and ~ 57 ppt h^{-1} in the free troposphere using aircraft HONO flux measurements made at a forested region in northern Michigan during the summer. Zhou et al. (2011) also measured HONO fluxes in a forest area in Michigan during the summer and found a HONO missing source of about 140 ppt h^{-1}. Even though studies concur about the existence of a ground source of daytime HONO, they disagree on its production mechanism. While Zhou et al. (2011) supports the hypothesis that the dominant daytime HONO formation pathway is the photolysis of HNO_3 on the canopy, Wong et al. (2012) favors the HONO chemical formation mechanism proposed by Stemmler et al. (2006) in which HONO is formed through a photo-enhanced NO_2 conversion humic acid; their calculated missing HONO source (for four sunny days in a urban environment) ranged between 730-1300 ppt h^{-1}. Additionally, VanderBoer et al. (2013) determined the missing source of HONO to be 165-600 ppt h^{-1} in a semi-rural area and showed that the amount of HONO deposited on

the ground during the night is comparable to the unknown daytime source of HONO. These studies show that the magnitude and formation mechanism of the unknown source of HONO varies significantly with height and location. Vertical profiles of HONO, such as those measured by the UCLA LP-DOAS, can help to determine if daytime HONO is formed in the gas-phase, aerosol, or at the ground. In addition, the profiles can also be used to quantify the potential surface flux of HONO.

1.4.4 HONO snow chemistry

In the past, measurements of trace gas chemistry at high latitudes served to examine tropospheric concentrations of trace gases in a clean background atmosphere. Concentrations of trace gases, such as NO_x, were expected to be comparable to levels seen in the remote marine boundary (i.e., in the low few pptv (Logan, 1983)), hence, it was a surprise when scientists measured elevated levels of NO_x within the snowpack (NO_x was 3 to >10 times higher than in ambient air) at Summit, Greenland (Honrath et al., 1999). A number of studies at other high latitude locations were subsequently conducted (Beine et al., 2002b; Dibb et al., 2002; Jacobi et al., 2004); all of them came to the same underlying conclusion that exposing natural snow to light release NO and NO_2 into the boundary layer (Beine et al., 2002b). Several of the studies extended measurements to include HONO. Their results indicated a photochemical source of HONO from snow and showed no significant HONO levels in locations where the snow was alkaline (Arnoroso et al., 2006; Beine et al., 2006). The ratio of photochemical production of HONO to NO_2 ranged between 1-3 at Summit Greenland and the emission ratio of NO_x to HONO was roughly 1 in Alert (Beine et al., 2002a).

1.4.4.1 Production mechanisms of NO_x and HONO over snow

Controlled studies in the laboratory and field suggest that reactions leading to the production of NO_x and HONO occur in the disordered air-ice interface, also referred as the Quasi-Liquid Layer (QLL), within the ice structure (Döppenschmidt and Butt, 2000). In their study, Chu and Anastasio (2007) found that the temperature-dependence of the NO_3^- quantum yield efficiency in both solution and ice are the same, suggesting that photolysis of NO_3^- on ice occurs in the QLL and not in the bulk ice. NO_3^- photolysis in the aqueous phase is presumed to proceed via two channels:

$$NO_3^- \xrightarrow{h\nu > 290\ nm} NO_2 + O^- \qquad (R21)$$

$$NO_3^- \xrightarrow{h\nu > 290\ nm} NO_2^- + O(^3P) \qquad (R22)$$

The nitrite (NO_2^-) produced in R21 can go through photolysis (R22) or react with O_3 or OH (R24) (Jacobi and Hilker, 2007; Chu and Anastasio, 2007):

$$NO_2^- \xrightarrow{h\nu} NO + O^- \qquad (R23)$$

$$NO_2^- + OH \rightarrow NO_2 + OH^- \qquad (R24)$$

The dominant product of NO_3^- photolysis is gaseous NO_2, a result supported by field observations that have found NO_2 production to exceed that of NO (Dibb et al., 2002). However, the work of Dubowski et al. (2000) argues that only NO_2 produced near the ice crystal-air interface is released from the snow, the rest of the produced NO_2 undergoes secondary chemistry (Boxe et al., 2005).

A number of mechanisms have been proposed for the formation of HONO within snow. Under the assumption that the acid/base equilibria for liquid water can be applied to snow, it follows that NO_2^- formed in snow can be protonated to produce HONO, which can then be released into the gas phase:

$$NO_2^- + H^+ \rightarrow HONO \qquad (R25)$$

The work of Jacobi and Hilker (2007) suggest that formation of HONO within snow is greatly dependent on the pH of the QLL; because the pKa of HONO is 2.8 in solution, HONO production is not expected in snow with pH > 5. This agrees with Beine et al. (2003, 2005) and Amoroso et al. (2005) field measurements, which show no HONO production in alkaline snow (at this time, the pH of melted is acidic except in regions influenced by dust or sea salt). However, studies at Browning Pass, Antarctica show small emissions of HONO even though the snow is acidic (Beine et al., 2006).

Another possible HONO production mechanism within snow interstitial air is the reaction of NO_2 (from NO_3^- photolysis) with photosensitized organics (George et al., 2005; Stemmler et al., 2006). This pathway could explain variations of HONO productions from snow in coastal Antarctica where high levels of impurities were present in snow (Grannas et al., 2007).

Recent laboratory and model studies show low direct yield of HONO from nitrate photolysis and proposed HONO formation by secondary heterogeneous chemistry, such as reduction of NO_2 by photosensitized organics (George et al., 2005; Stemmler et al., 2006), as a possible HONO production mechanism in Polar Regions (Jacobi and Hiker, 2007). Reduction of NO_2 (R21) was observed in laboratory studies on ice and snow surfaces containing traces concentrations of humic acids (Beine et al., 2008; Bartels-Rausch et al., 2010). The fast kinetics of reaction R21 coupled with the ubiquitous presence of organic compounds on snow makes this pathway a likely HONO source in Polar Regions.

1.4.4.2 HONO measurements over snow

In general, HONO measurements at polar sites were difficult to reconcile with observations of HO_x and NO_x (Grannas et al., 2007). Furthermore, when mist chamber measurements of HONO (~30 pptv average) were used in a modeling study of ISCAT 1998 (Chen et al., 2001), it over-predicted boundary layer OH observations by a factor of 2 to 5. These HONO measurements also conflicted with ambient NO_x concentrations (Chen et al., 2001), which raised questions about the validity of the mist chamber HONO measurements. Results from the Spring 2004 study in Summit Greenland also raised questions about the reliability of their HONO measurements. Their HO_2 + RO_2 observations were in great agreement with model predictions only when HONO observations were not taken into account in the model (Grannas et al., 2007). On the other hand, by using ambient air measurements from Alert, Zhou et al. (2002) found that a significant photochemical source of HONO exists, making HONO the dominant OH source in the boundary layer at times. These results agree with Grannas et al. (2002) model results with the caveat that the model predictions were not verified with HO_x observations.

1.4.5 HONO measurement techniques

A number of analytical techniques are currently in use to measure ambient HONO. This section briefly describes the most common techniques used to measure HONO.

Incoherent Broad Band Cavity-Enhanced Absorption Spectroscopy (ACES or IBBCEAS)

IBBCEAS is a spectroscopic in-situ technique, which uses the UV absorption in a cavity to identify and quantify HONO. In this technique, light is trapped between two

highly reflective dielectric mirrors, resulting in a long effective absorption path length. Data retrieval involves absorption spectral fittings of absorbing species using light transmitted by the cavity in the absence and presence of the absorbing species (Wu et al., 2012). A study on aircraft measurements of HONO, glyoxal, and other trace gases reported a detection limit of ~200 ppt for HONO (Min et al., 2016). Details about this technique can be found in Min et al. (2016).

Chemical Ionization Mass Spectroscopy (CIMS)

CIMS is an in-situ technique that uses a reagent to chemically ionize HONO molecules so that they can be identified in a mass spectrometer. The HONO molecule can be ionized through iodide ion transfer reaction (iCIMS or Iodide Chemical Ionization Mass Spectrometry) or through a negative proton transfer reaction (NI-PT-CIMS or Negative Ion Proton Transfer Mass Spectrometry). The ionized HONO is analyzed by a mass spectrometer. High sensitivity (detection limit ~10-25 pptv) and time resolution (1s) have been achieved through this measurement method (Roberts et al., 2010).

Long Path Absorption Photometry (LOPAP)

LOPAP is a wet chemical in situ instrument, which directly samples gaseous HONO in a stripping coil. In general, no sampling lines are used with this instrument minimizing sampling artifacts on surfaces. The stripping reagent is converted to an azo dye. Absorption of light from a light emitting diode is measured in long-path absorption tubes. Two stripping coil are used, the first channel determines HONO and possible interferences and the second channel only quantifies the interferences. The HONO signal

is obtained by taking the difference of these two channels (Kleffmann et al., 2002; Pinto et al., 2014).

Differential Optical Absorption Spectroscopy (DOAS)

DOAS is a measurement technique that quantifies HONO based on its narrowband absorption structures in the UV spectral region. The theory behind DOAS is to separate an absorption spectrum into narrowband and broadband absorption features. By calculating the differential absorption the concentration of a specific trace gas can be derived (Platt and Stutz, 2008). This technique is described in detail in Chapter 2.

1.5 Motivation

Despite of decades of research, the formation mechanism of daytime HONO is still unknown and there is no consensus on whether daytime HONO is formed on the ground, aerosol surfaces or through gas phase reactions. Furthermore, little is known about daytime HONO's behavior over soil and snow surfaces in polluted rural areas as most measurements were performed in urban, semi-urban, polar, or forested regions. Moreover, the validity of HONO measurements over snow, and the role it plays on the HO_x budget are also under debate. The primary objective of my dissertation is to advance the knowledge of wintertime HONO concentrations, sources, and vertical distribution in polluted rural areas influenced by oil and gas development. By better understanding the behavior of HONO in these environments, we can determine its role and the magnitude of its influence in the formation of wintertime ozone. To accomplish the aforementioned objectives we participated in the UBWOS 2012 and UBWOS 2014

field studies where we measured wintertime HONO concentrations at different vertical heights using the UCLA LP-DOAS. The measurement site, located within the Uintah Basin, Utah, was highly influenced by gas and oil extraction activities. Different meteorological conditions in the winter of 2012 and 2014 granted us the opportunity to study HONO over soil (UBWOS 2012) and snow surfaces (UBWOS 2014).

The objective of this dissertation is to address the following questions regarding HONO chemistry in a polluted rural environment:

- What are the HONO source mechanisms over wintertime soil and snow?
- Can proposed surface HONO sources close the HONO budget?
- Is NO_3 photolysis the main source of daytime HONO, as it is in the Polar Regions?

Chapter 2 gives a brief description of the UBWOS (Uintah Basin Winter Ozone Studies) field studies with a focus on UBWOS 2012 and UBWOS 2014. The DOAS technique, the experimental set up of the UCLA LP-DOAS system and the evaluation of the data is also described in this Chapter. Chapter 3 describes how HONO vertical profiles were retrieved, HONO fluxes were calculated, and formation rates of HONO determined. Chapter 4 presents results from the UBWOS 2012 study, which includes the observations of light path averaged HONO, the retrieved daytime vertical profile of HONO, calculated HONO fluxes, and daytime HONO budget. Chapter 5 presents results from the UBWOS 2014 study, which includes the observations of light path average HONO, retrieved daytime vertical profile of HONO, calculated HONO fluxes, and

daytime HONO budget. A brief inter-comparison of HONO measurements is also described in this chapter. Chapter 6 gives the conclusion and outlook of this dissertation.

Chapter 2 Methodology and Field Experiments

Chapter 2 gives a brief description of the UBWOS (Uintah Basin Winter Ozone Studies) field studies with a focus on UBWOS 2012 and UBWOS 2014. The experimental setup of the UCLALP-DOAS DOAS system, the DOAS technique, and the evaluation of the data are also described in this Chapter.

2.1 The Uintah Basin Winter Ozone Study (UBWOS)

UBWOS was a multi-year study that took place in the Uintah Basin, Utah, during the winters of 2011-2012 (UBWOS 2012), 2012-2013 (UBWOS 2013), and 2013-2014 (UBWOS 2014). The main purpose of the study was to identify the emission sources and photochemical processes that lead to elevated wintertime O_3 formation, and to identify effective strategies to mitigate winter ozone.

The Uintah Basin is located in the northeast corner of Utah and is part of the Colorado Plateau. It is bound by the Uintah mountain range in the north, the Book and Roan Cliffs in the south, the Wasatch Range in the West, and elevated terrain in the East (Figure 2.1). The floor of the Basin is about 1570 m above sea level (Lyman and Shorthill, 2013; Stoeckenius 2015). The basin is mostly rural, with a population of about 50,000, concentrated mainly in three towns: Duchesne, Roosevelt, and Vernal (Figure 2.1). The economy of the Basin is primarily based of energy production from petroleum resources with approximately 10,000 active oil and gas wells, sparsely distributed in the

southern corner of the Basin. The Basin also houses a 500-megawatt coal-fired power plant (Bonanza), which is about 12 miles southeast of the UBWOS main measurement site.

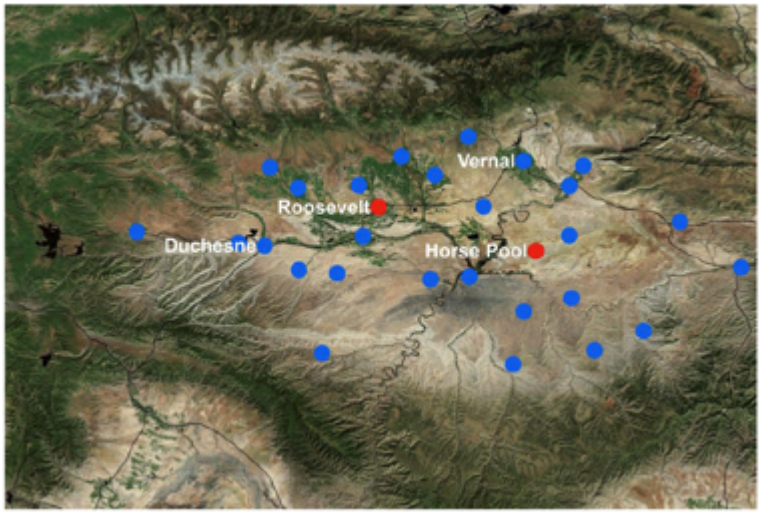

Figure 2.1 UB 2011- 2012 monitoring sites (blue dots). Cities and Horse Pool site are labeled. Adapted from Lyman and Shorthill (2013)

The UBWOS 2012 field study took place between January and early March 2012. The most detailed measurements were conducted at the main site (also known as Horse Pool site) located in the northern part of the UB, about 35 km south of Vernal (Figure 2.1). Meteorological conditions were not conducive for snow cover; preventing O_3 levels to surpass the NAAQS (the highest eight-hour average was 63 ppb and the median values ranged from 28-46 ppb at the measuring site). The lack of ozone formation conditions during UBWOS 2012 motivated a second winter ozone study in 2013 at the same location and time of year. Storms during December and early January produced abundant snow that favored ozone formation during UBWOS 2013 and numerous 8-hour average ozone concentrations above the NAAQS were observed. By comparing measurements

made during UBWOS 2012 and UBWOS 2013, scientists concluded that snow cover, calm weather conditions, and significant emissions of ozone precursors (i.e. VOCs and NO_x) are required for winter ozone formation. HONO measurements made with an Acid CIMS instrument during UBWOS 2013 show larger daytime average HONO mixing ratios (0.55±0.58 ppb) than those measured in 2012 (0.05±0.04 ppb), suggesting that daytime HONO might be the primary chemical driver of winter ozone formation in the UB. However, further analysis brought into question the accuracy of the observed HONO concentrations, as concerns about a positive bias in HONO measurements were raised. As a result, a follow up study during winter of 2013-2014 (UBWOS 2014) was performed to obtain reliable and representative HONO measurements from a variety of analytical techniques. Four different in-situ measurement techniques including the ACES (Incoherent broadband absorption spectroscopy), iCIMS (Iodide ion chemical ionization mass spectrometry), LOPAP (Long Path Absorption Photometer), Negative Ion Proton Transfer Mass Spectrometry/ToF), and the UCLA LP-DOAS were used to measure HONO during UBWOS 2014. These techniques will be described in the following sections, with a particular focus on the UCLA LP-DOAS from which most of the data in this thesis was derived.

2.2 Differential Optical Absorption Spectroscopy (DOAS)

The differential optical absorption spectroscopy (DOAS) technique has been widely used to detect tropospheric trace gases since its first application in the late 1970's. Perner and Platt (1979) measured atmospheric OH reliably for the first using the DOAS method.

The DOAS technique, like all absorption-spectroscopy methods, is based on the Lambert-Beer's law, which states that the intensity of a collimated beam passing through a uniform transparent medium decreases exponentially as a function of the length and properties of the medium.

$$I(\lambda) = I_0(\lambda) * \exp(-\sigma(\lambda, T) * c * L) \quad \text{(equation 2.1)}$$

$I_0(\lambda)$ represents the initial intensity emitted by a light source and $I(\lambda)$ denote the intensity of the beam after passing through a medium of length L populated by an absorber with uniform concentration c. $\sigma(\lambda)$ represents the absorption cross-section (a characteristic property of a species) of the absorber at wavelength λ . The amount of light absorbed by a layer of a species, also called optical density (D), is linearly related to c. Here, optical density is defined as the natural logarithm of the ratio between $I_0(\lambda)$ and $I(\lambda)$ and c can be calculated using D:

$$D(\lambda) = \ln\left(\frac{I_0(\lambda)}{I(\lambda)}\right) \quad \text{(equation 2.2)}$$

$$c = \frac{D(\lambda)}{\sigma(\lambda,T)*L} \quad \text{(equation 2.3)}$$

To apply equation 2.1 to light absorption in the atmosphere it is necessary to take into consideration other light attenuation substances and phenomena. Equation 2.4 shows an expanded version of equation 2.1 that includes various trace gases concentrations (c_j) and absorption cross-sections ($\sigma_j(\lambda,T)$), Rayleigh ($\varepsilon_R(\lambda)$) and Mie ($\varepsilon_M(\lambda)$) extinction, and instrumental and turbulence effects (summarized in $A(\lambda)$):

$$I(\lambda) = I_0(\lambda) * \exp\left[-L * \left(\sum\left(\sigma_j(\lambda, T) * c_j\right) + \varepsilon_R(\lambda) + \varepsilon_M(\lambda)\right)\right] * A(\lambda) \quad \text{(equation 2.4)}$$

One of the challenges in applying Beer's law in the atmosphere is the inability of removing the absorbing gases from the atmosphere to obtain $I_0(\lambda)$. A solution to this problem is to separate the broadband and narrowband spectral structures in an absorption spectrum. While aerosol extinction processes, the effect of turbulence, and many trace gas absorption show broad spectral features, certain trace gases, such as NO_2, O_3, and HONO, show narrowband spectral structures; hence the spectral data can be split into a high frequency ($\sigma_j'(\lambda, T)$) and a low frequency ($\sigma_{j0}(\lambda, T)$) part:

$$\sigma_j(\lambda, T) = \sigma_{j0}(\lambda, T) + \sigma_j'(\lambda, T) \qquad \text{(equation 2.5)}$$

Substitution of $\sigma_j(\lambda, T)$ with $\sigma_j'(\lambda, T)$ and $\sigma_{j0}(\lambda, T)$ in equation 2.4 results in

$$I(\lambda) = I_0(\lambda) * \exp\left[-L * \left(\sum\left(\sigma_j'(\lambda, T) * c_j\right)\right)\right] * \exp\left[-L(\sum\left(\sigma_{j0}(\lambda, T) * c_j\right) + \varepsilon_R(\lambda) + \varepsilon_M(\lambda))\right] * A(\lambda) \qquad \text{(equation 2.6)}$$

The broad spectrum can be used as a new intensity spectrum ($I_0^{'}(\lambda)$, equation 2.7) to allow Lambert-Beer's law to be applied to the narrowband trace gas absorption:

$$I_0^{'}(\lambda) = I_0(\lambda) * \exp\left[-L\left(\sum\left(\sigma_{j0}(\lambda, T) * c_j\right) + \varepsilon_R(\lambda) + \varepsilon_M(\lambda)\right)\right] * A(\lambda) \qquad \text{(equation 2.7)}$$

Hence atmospheric trace gas concentrations can be calculated using:

$$c_j = \frac{D^{'}(\lambda)}{\sigma_j'(\lambda,T) * L} = \frac{\ln\left(\frac{I_0^{'}(\lambda)}{I(\lambda)}\right)}{\sigma_j'(\lambda,T) * L} \qquad \text{(equation 2.8)}$$

The split of spectra data into broad and narrow structures and the separation of the various absorbers in equation 2.6 require that radiation intensity be measured at multiple wavelengths. One of the advantages of using differential absorption over an extended

wavelength range is that no calibration of the optical properties is needed because transmissions of optical instruments typically show broad spectral characteristics.

2.3 LP-DOAS instrument

The UCLA Long-Path DOAS, referred hereafter as LP-DOAS, is an active DOAS system that consists of a Newtonian telescope that sends and receives a collimated light beam of a high-pressure Xe arc lamp. The light beam is folded once by retro-reflector arrays mounted at about 2.5 km distance. Each array consists of approximately 30 corner cube quartz retro-reflectors with angular precision in the order of 2 arc-seconds. The retro-reflectors return the incident light almost exactly into the direction of incidence, reducing the effects of atmospheric turbulence on the light beam. The spectrometer and the telescope are coupled by a 350 μm quartz fiber that is connected to a mode mixer (Figure 2.2). The purpose of the mode mixer is to produce a uniform intensity distribution at the spectrometer's field of view by bending and shaking the fiber. This step is necessary as non-uniform illumination of the field of view of the spectrometer can cause structures in the spectra that can limit the minimum detectable optical density (Stutz and Platt, 1997).

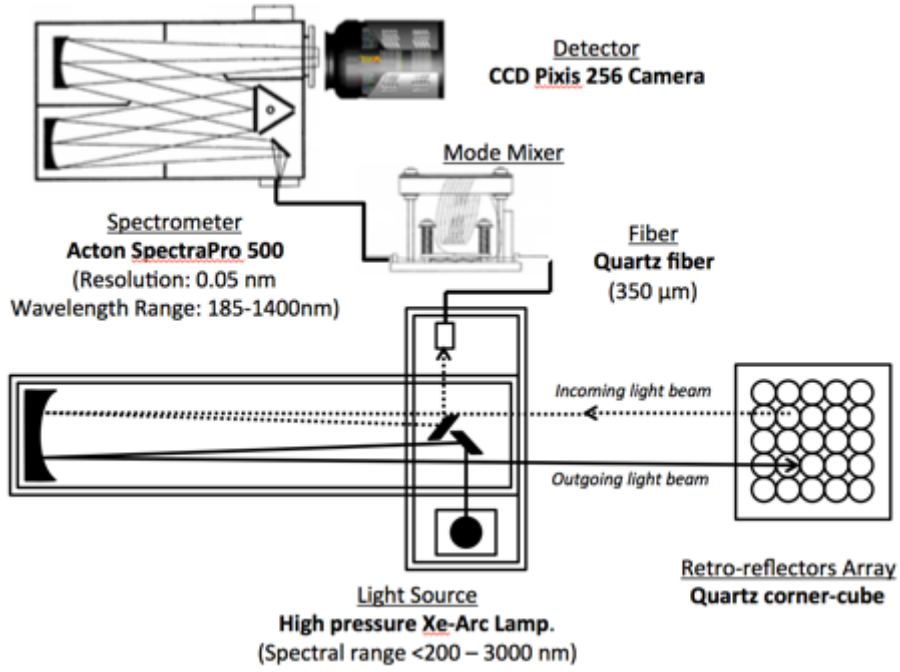

Figure 2.2 Schematic of UCLA LP-DOAS system used in UBWOS 2012 and 2014

Spectra were recorded at a resolution of about 0.5 nm by a Czerny-Turner/Acton Spectra Pro 500 spectrometer with a focal length of 0.5 m in the wavelength range of 300-380 nm. A Princeton Instrument Pixis 256 CCD camera was used for the detection of the spectra. A downside of using a solid-state detector, such as a CCD, is the diode-to-diode variability, which depends on the wavelength of the incoming light and can vary from 1% to several percent between the diodes of one array (Stutz, 1996; Platt and Stutz, 2008). Fortunately, the diode-to-diode sensitivity is usually systematic and can be corrected using the multichannel scanning technique (MCST)(Knoll et al.,1990; Stutz and Platt, 1996). A more detailed description of the MCST technique is given in section 2.6.

2.3.1 Advantages of using active LP-DOAS

The benefits of measuring a multitude of wavelengths, such as in the DOAS technique, include the unique identification of trace gas absorptions, simultaneous

measurements of various trace gases, and ability to observe and quantify trace gases with weak absorptions. In addition, measuring long light paths in the atmosphere increases the sensitivity of the instrument, provides spatially averaged values, eliminates the need of calibrations, and avoids interferences generated by chemistry on instrument surfaces.

2.4 UCLA LP-DOAS setup during UBWOS 2012, 2014

The UCLA LP-DOAS system measured mixing ratios of NO_2, O_3, HONO, HCHO, and SO_2 in the Uintah Basin at the Horse Pool site (40° 8' 37.339'' N; 109° 28' 1.849'' W; 1569 m above sea level) from January 22 to February 28, 2012 (UBWOS 2012) and January 20 to February 14, 2014 (UBWOS 2014). The UCLA LP-DOAS system consisted of the LP-DOAS telescope, set up in a tent (2012) or container (2014) at the Horse Pool site at about 2 m above ground level, and three retro-reflector arrays installed on a bluff located at about 2.5 km northwest of the main site (Figure 2.3, right panel). The retro-reflector arrays were set up at the base, midway, and top of the bluff at about 31 m, 45 m, and 68 m above the height of the LP-DOAS instrument. Figure 2.3 shows the location of the retro-reflectors relative to the location of the instrument, the three light paths (lower, middle, and upper), and the surface topography under each light path. Figure 2.3 (left panel) shows similar surface topographies under the three light paths. The retro-reflectors arrays were installed relatively close to each other to reduce the effects of horizontal inhomogeneity. The maximum horizontal distance between the light paths was ~64 m. The light- paths cross natural soil and dry wintertime vegetation.

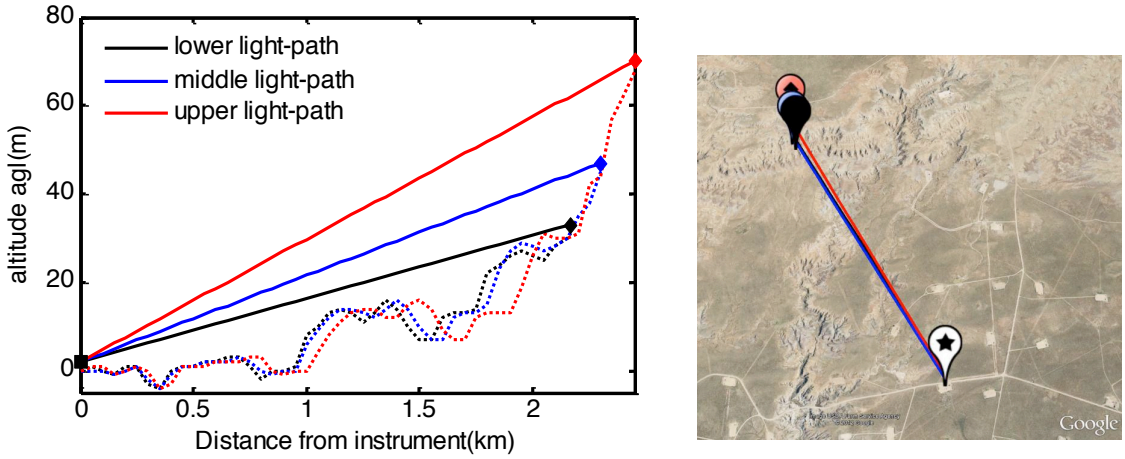

Figure 2.3 UCLA PL-DOAS system setup in 2012 and 2014. Light paths are shown in solid lines (low in black, middle in blue, and upper in red). The left panel shows the side view of the system with the DOAS instrument represented by the solid square and the retro-reflector arrays represented by the diamonds. Topography under each light path is shown in dashed lines. Map data: Google. The right panel shows the top view of the light paths with retro-reflectors located northwest of the DOAS instrument (white marker with black star). Map data: Google.

2.5 DOAS data analysis procedure

Measuring light intensity, $I(\lambda, L)$, changes I in two ways: first, the shape of $I(\lambda, L)$ changes due to the limited resolution of the spectroscopic instruments. This process can be mathematically described by a convolution of $I(\lambda, L)$ with the spectrograph instrument function H:

$$I^*(\lambda, L) = I(\lambda, L) * H \qquad \text{(equation 2.9)}$$

Second, I^* is digitized by the detector. The wavelength range is mapped onto n discrete pixels/channels, numbered by i. Each pixel integrates the light in a wavelength interval from $\lambda(i)$ to $\lambda(i+1)$.

$$I'(i) = \int_{\lambda(i)}^{\lambda(i+1)} I^*(\lambda')d\lambda' \qquad \text{(equation 2.10)}$$

The λ interval is given by the wavelength-pixel mapping of the instrument. In our case, the wavelength-pixel mapping of the instrument is approximated by the linear dispersion equation:

$$\Gamma_I = \lambda(i) = \gamma_0 + \gamma_1 \times i \qquad \text{(equation 2.11)}$$

While γ_0 describes the spectral shift of the spectrum, γ_1 squeezes or stretches the spectrum linearly.

The DOAS data analysis procedure starts with the linearization of $I'(i)$ in equation 2.10 by calculating the logarithm $J(i) = \ln(I'(i))$:

$$J(i) = J_0(i) + \sum_{j=1}^{m} a_j' * S_j'(i) + B'(i) + R'(i) + A'(i) + N'(i) \qquad \text{(equation 2.12)}$$

Where:

$S_j'(\lambda) = \ln(\exp(-\sigma_j'(\lambda))) * H$: describes the trace gases narrow band absorptions calculated from the convolution of individual trace gases (j) cross-sections and the instrument function H.

$a_j' = c_j \times L$: denotes the scaling factors, which are a product of the average number densities c_j over the path-length L.

$B'(i)$: represents the broadband absorptions of trace gases.

$R'(i)$: represents the extinction caused by Mie and Rayleigh scattering.

$A'(i)$: summarizes the variation in the spectral sensitivity due to the detector.

$N'(i)$: is the detector noise and photon statistics.

The sum in equation 2.12 describes the overlaying absorption structures of m absorbers with absorption structures sufficiently strong to be detectable with the UCLA LP-DOAS. For a detailed derivation of equation 2.12 please refer to Platt and Stutz (2008) page 163.

The purpose of the DOAS analysis is to solve for $S_j'(\lambda)$ and coefficient a_j' by minimizing the difference between our measured $J(i)$ and $F(i)$, a function that describes the dependence of $J(i)$ on the parameters ($S_j'(\lambda)$). In our DOAS evaluation, the logarithm of the measured intensity $J(i)$ is modeled by:

$$F(i) = P_r(i) + \sum_{j=1}^{m} a_j \times S_j\left(d_{j,0}, d_{j,1}\right)(i) \qquad \text{(equation 2.13)}$$

where S_j are the absorption structures of trace gases inputted into the procedure and a_j are the result of the fit, which are used to calculate the concentration c_j. The polynomial $P_r(i)$ describes the broad spectral structures caused by the lamp, scattering processes, spectral sensitivity, and trace gas broadband absorptions.

The model function is determined by two sets of parameters: (1) a_j, which scales the cross section and is linear in $F(i)$; (2) $d_{j,0}$ and $d_{j,1}$, which shifts and squeezes each reference spectrum and can only be fitted through a non-linear method, such as a Levenberg-Marquardt procedure. The fitting process starts by determining a_j through a linear least-squares method using the measured spectrum $J(i)$ and a reasonable starting value for $d_{j,0}$ and $d_{j,1}$; then, $d_{j,0}$ and $d_{j,1}$ are estimated by performing a Levenberg-Marquardt fit with the a_j term obtained in the preceding step. The fitting process continues by alternating the two fitting methods, using the result of the previous method as new values for the next fit, until χ^2 in the last step is smaller than 10^{-6} (Platt and Stutz,

2008). The light path average concentrations of trace gases can be calculated using the scaling factor (a_j) and absorption cross-sections (σ_j):

$$c_j = \frac{a_j}{\sigma_j \times L} \qquad \text{(equation 2.14)}$$

Figure 2.4 shows a flowchart describing the linear and non-linear fitting procedure.

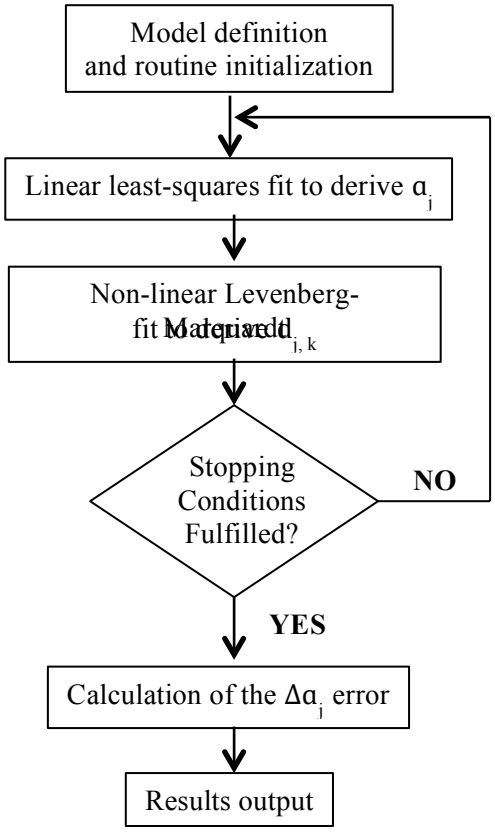

Figure 2.4 Flowchart of DOAS linear-non-linear analysis procedure. Adapted from Platt and Stutz (2008).

2.6 DOAS measurement and evaluation procedure during UBWOS 2012 and UBWOS 2014

In order to remove diode sensitivity variations, we used the Multichannel Scanning Technique (MCST) introduced by Knoll et al., (1990). Our implementation of the MCST technique consisted of repeating the light intensity and background measurements nine

times but shifting the wavelength by 0.8 nm on each repetition (starting from 341.8 nm to 348.2 nm center wavelength). After subtracting the background spectrum from its corresponding light spectrum, the atmospheric spectra were co-added to give a sensitivity curve of the individual diodes. Each atmospheric spectrum was divided by the sensitivity curve and shifted to 345 nm center wavelength. Finally, the nine shifted spectra were added to obtain a MCST spectrum.

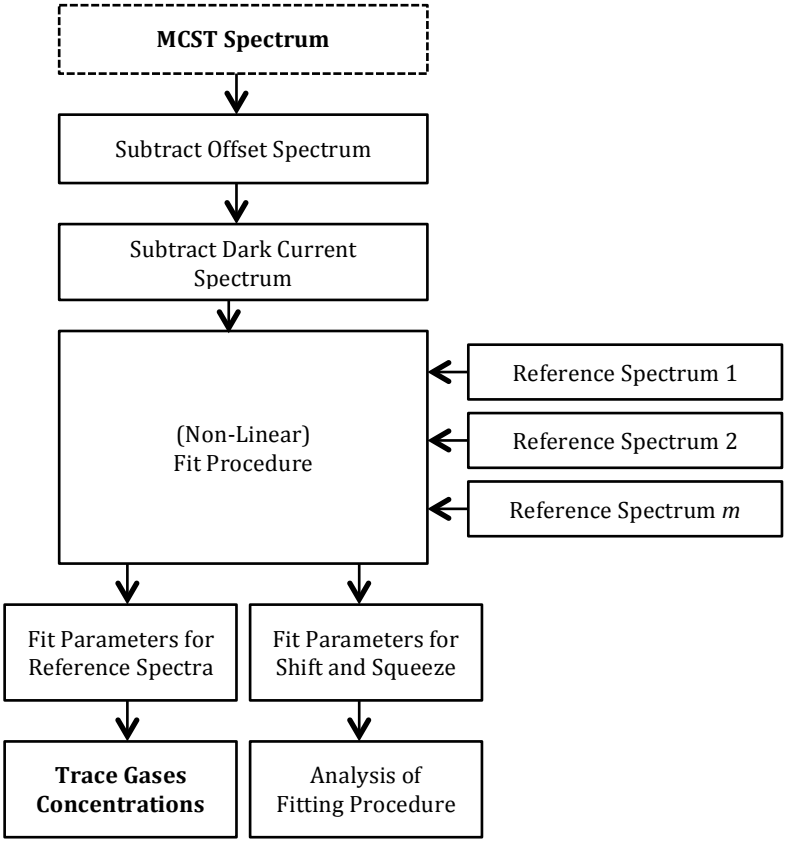

Figure 2.5 Flowchart of UCLA LP-DOAS measurement and analysis procedure. Adapted from Platt and Stutz (2008).

Figure 2.5 shows the evaluation process that we employed to retrieve trace gases concentrations from MCST spectra. The MCST spectra were analyzed using a combination of linear and non-linear least squares procedure, which fitted reference

spectra of trace gases, lamp spectra, and a polynomial (Figure 2.5). The light path average concentrations of NO_2, HONO, HCHO, O_3, and SO_2 were calculated using the scaling factors of the reference spectra and the absorption cross sections (a detailed explanation of the fit procedure and the calculation of light path average concentrations can be found in Chapter 2 section 2.2). The reference spectra used in the fit were calculated from literature absorption cross sections, which were run through a MCST procedure to match the observations. Table 2.1 lists the wavelength range, literature cross-sections, and species used to retrieve light path averaged trace gas concentrations. The detection limits of each retrieved trace gas measured during UBWOS 2012 and 2014 are also shown in Table 2.1.

Table 2.1 Fit parameters for retrieval of gases during UBWOS 2012 and UBWOS 2014

Trace gases	**Wavelength Range (nm)**	**Literature Cross Sections (Uncertainty in parenthesis)**	**Fit Spectral References**	**Average Detection Limits UBWOS 2012**	**Average Detection Limits UBWOS 2014**
HCHO	324-346	*Meller and Moortgat, 2000* (280K) – UBWOS 2012 (5%) *Chance and Orphal*, 2011 (263K) – UBWOS 2014 (5%)	NO_2, HONO, HCHO, O_3, and O_4*	0.3 ppb	0.3ppb
HONO	338-344 351-371	*Stutz* et al., 2000 (298K) – UBWOS 2012 and 2014 (5%)	NO_2, HONO, HCHO, O_3, and O_4*	0.03 ppb	0.075 ppb
NO_2	338-344 351-371	*Vandaele et al., 1998* (294K) – UBWOS 2012 (2% - 5%) *Voigt* et al., 2002 (260K) – UBWOS 2014 (4% - 6%)	NO_2, HONO, HCHO, O_3, and O_4*	0.07 ppb	0.22 ppb
O_3	324-346	*Serdyunchenko et al*., 2014 (273K) – UBWOS 2012 and 2014 (3%)	NO_2, HONO, HCHO, O_3, and O_4*	1.4 ppb	3.3 ppb
SO_2	305-310 313-321	*Vandaele et al., 1994* (296K) – UBWOS 2012 (2.4%) *Bogumil* et al., 2003 (273K) – UBWOS 2014 (3%)	NO_2, HCHO, O_3, and SO_2	0.05 ppb	0.16 pbb

*O_4 literature cross-section: Fally et al. (2000) (298K) - UBWOS 2012and 2014.

2.6.1 Example of analysis procedure

The spectral fitting analysis was performed using DOASIS UI 3.2 (Lehmann, 2008), a versatile software created to work with spectral data. Figure 2.6 shows the spectral analysis of NO_2 and HONO for an atmospheric spectrum taken during UBWOS 2012. Figure 2.6a shows the raw atmospheric spectrum and Figure 2.6b shows the same spectrum as in Figure 2.6a but with the broad spectral features removed (blue line) by a high-pass filter. NO_2 and HONO fit results are shown in Figure 2.6b (red line) and Figure 2.6c (red line) respectively. The residual spectrum of the fit is shown in Figure 2.6c (black line). The general effect of residuals is to determine the error of the derived trace gas concentrations.

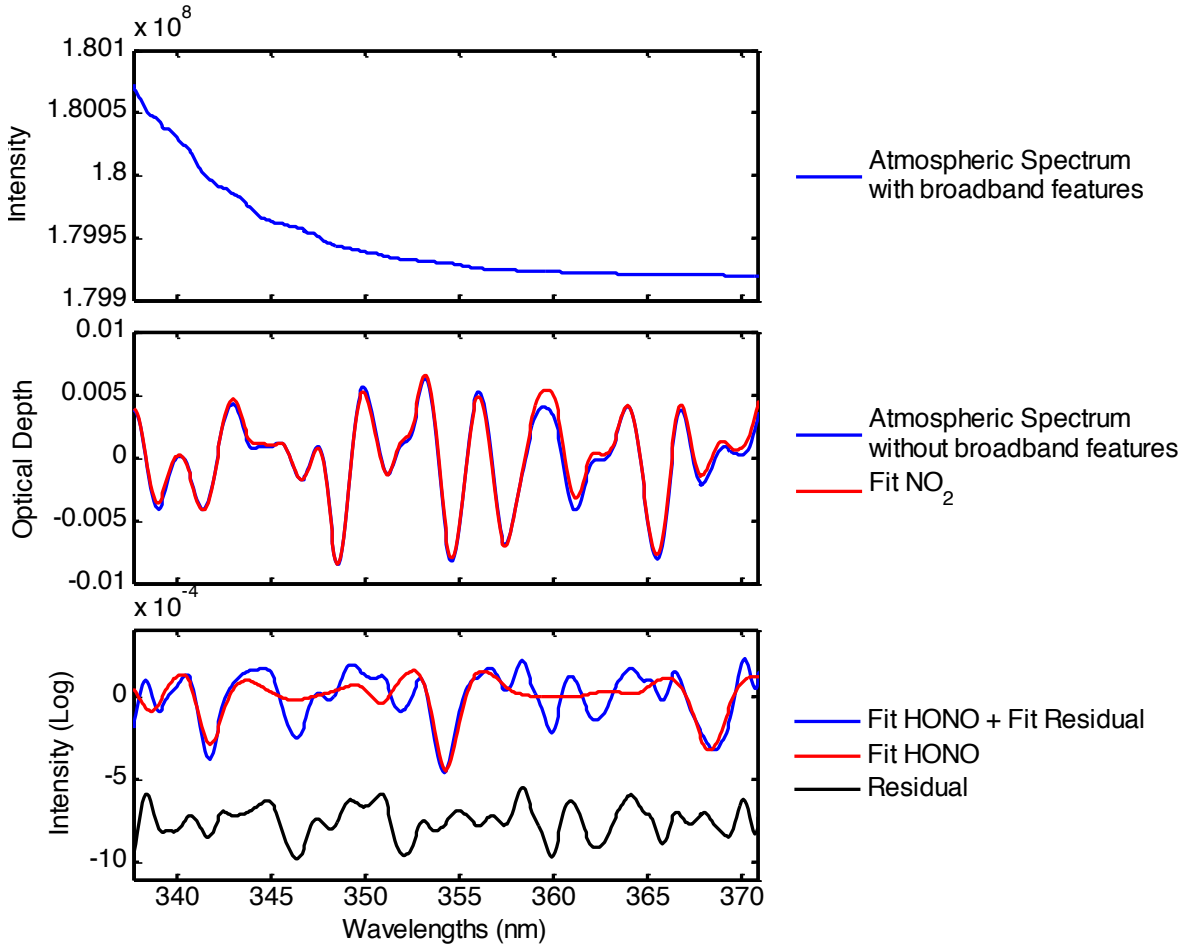

Figure 2.6 Fitting procedure of spectrum measured on 2 February 2012 0243 hours MST using DOASIS. (a) Atmospheric spectrum with broadband features. (b) Fit of NO_2 (red line) superimposed on atmospheric spectrum without broadband features (blue line). (c) Fit of HONO (red line) superimposed on sum of fit HONO and fit residual (blue line); residual spectrum (black) shifted 7.5×10^{-4} on the y-axis for better comparison with fitted HONO.

2.6.2 DOAS error analysis

The inability to repeat measurements under the same experimental condition in the atmosphere hinders the derivation of errors based on the statistical behavior of

measured concentrations. Therefore, DOAS uses spectroscopic information and the quality of analysis of each spectrum to derive an error for each measured concentration.

The fit procedure described in section 2.1.2 calculates the error for a_j (Δa_j), which is derived from the linear least squares part of the fit. Stutz and Platt (1996) have shown that the error of the trace gas concentrations calculated by the least square fitting procedure underestimates statistical errors; therefore, we followed the practice of other studies that uses LP-DOAS measurements (Wong et al., 2012; Tsai et al., 2014) and corrected this bias by multiplying the error with a factor of two.

An important aspect of the DOAS analysis is the accurate description of the reference spectra S_j as poor quality reference spectra introduces systematic biases in the analysis. The uncertainty of the cross sections used in the UBWOS 2012/2014 analysis varied between 2% to 6%; more specifically, the errors were: 5% for the HCHO cross sections (Meller and Moortgat, 2000; ChanceOrphal, 2011), 5% for the HONO cross section (Stutz et al., 2000), 2-5 % (Vandaele et al., 1998) and 4-6% (Voigt et al., 2002) for the NO_2 cross sections, 3% for the O_3 cross sections (Serdyunchenko et al., 2014), and 2.4% (Vandaele et al., 1994) and 3% (Bogumil et al., 2003) for the SO_2 cross sections. The systematic error of the DOAS spectrometer was determined to be less than 3% by Stutz and Platt (1996). The average detection limit for each retrieved trace gas (shown in Table 2.1) was calculated by doubling the field study average error of each trace gas.

Chapter 3 HONO Vertical Profile and Fluxes Retrieval

Active DOAS instruments, such as the UCLA LP-DOAS, have been previously used to retrieve vertical distribution of trace gases (Stutz et al., 2004; Tsai et al., 2014; Wang et al., 2006; Wong et al., 2012). This method has been used to determine SO_2 deposition velocities (U. Platt, 1979), study nocturnal chemical processes (Stutz et al., 2004; Tsai et al., 2014), and daytime HONO chemistry (Wong et al., 2012). In short, trace gas concentrations averaged in vertical boxes (shown in Figure 3.1) are calculated using path-averaged trace gases concentrations observed on multiple light paths.

The set-up of the LP-DOAS system during the UBWOS studies was similar to studies that took place in cities such as Los Angeles, CA and Houston, TX. However, due to topographic limitations, the UBWOS light paths were on average shorter and closer to the ground than light paths used in some urban areas. Furthermore, the terrain under the light paths exhibited significant topographical variations (Figure 3.1). Because heterogeneous HONO formation on the ground plays an important role in HONO chemistry, it is necessary to take topography into account when retrieving HONO vertical distributions. Because this was not done in previous studies, a different approach to retrieve the HONO vertical distributions was developed for the UBWOS studies (section 3.1).

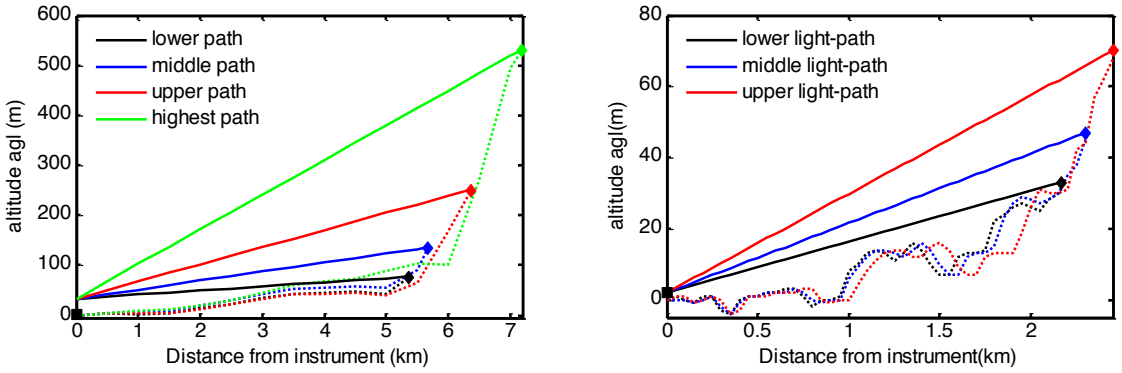

Figure 3.1 UCLA LP-DOAS set up in CalNex 2010, Los Angeles (left panel) and in UBWOS 2012/UBWOS 2014, Utah (right panel). Solid lines depict light paths and dashed lines depict topography under the light paths. Map data: Google.

3.1 HONO vertical profiles retrievals

HONO vertical profiles were retrieved using a least square minimization approach, where the average concentration of HONO along the light paths were simulated using a height (z) dependent exponential function:

$$F(z) = C_0 + C_1 \times \exp\left(-\frac{z}{c_2}\right) \qquad \text{(equation 3.1)}$$

C_0, C_1, and C_2 represent the HONO background concentrations, HONO surface concentrations, and a scale height, respectively. Our decision to use an exponential function to simulate the HONO mixing ratios along the light paths was based on our measured hourly average HONO mixing ratios (Figure 4.1 and Figure 5.1), which show noticeable negative gradient, and results from observational (VandenBoer et al., 2013; Zhang et al., 2009) and modeling (Wong et al., 2013) studies, which also showed negative HONO gradients and daytime vertical profiles that bare a resemblance to an exponential decay (Figure 3.2).

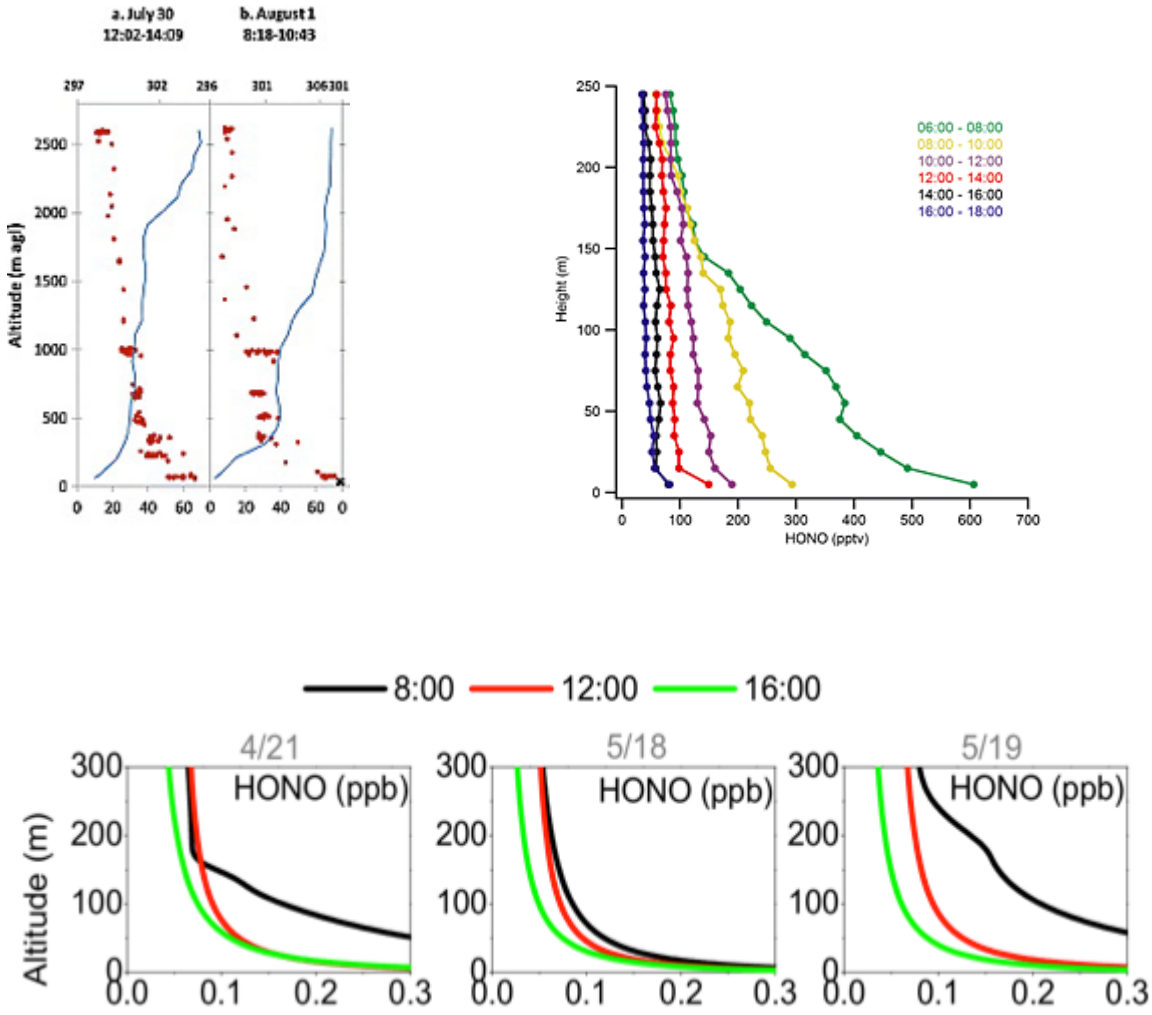

Figure 3.2 Observed and modeled vertical profiles of daytime HONO. Top left panel shows HONO mixing ratios measured over a forested region (red dots) and potential temperature profile over land (solid lines). The black cross shows the height of the measurement tower. Adapted from Zhang et al. (2009). Top right panel shows average vertical profiles of daytime HONO measured during NACHTT. Adapted from VandenBoer et al. (2013). Lower panel plot shows modeled daytime HONO vertical profiles at 0800, 1200, and 1600 hours CST. The model runs included a photolytic HONO source at the ground and on aerosols. Adapted from Wong et al. (2013).

The model parameters C_0, C_1, and C_2 were retrieved by minimizing χ^2:

$$\chi^2 = \sum_i (F_{TOPOG} - ydata_i)^2 \quad \text{(equation 3.2)}$$

where i is the light path index (lower, middle, and upper light path), $ydata_i$ are the measured HONO light path concentration averages, and $xdata_i$ are the simulated HONO light path averages based on equation 3.3. When calculating the HONO light path averages, the topography under each light path was taken into account:

$$F_{TOPOG} = \frac{1}{L_i} \sum_{j=1}^{L_i/50} \frac{50}{\cos(\alpha_i)} * (C_0 + C_1 \times \exp(-\frac{h_j}{c_2})) \quad \text{(equation 3.3)}$$

where L represents the length of the light path, α is the elevation angle, and h_j is the height between the light path and the surface at each j, or 50 m interval, in the horizontal distance between the instrument and the retro-reflector arrays. The model parameters, C_0, C_1, and C_2, were retrieved using Matlab's lscurvefit which uses the trust-region-reflective algorithm and is based on the interior-reflective Newton method described in (Thomas et al., 1994; Coleman and Li, 1996). We specified a lower allowable bound of 0 for both C_0 (HONO background) and C_1 (HONO surface concentrations) in the fit and left the decay term C_2 unbounded (going from –infinity to +infinity).

3.2 HONO flux calculations

We used the gradient method (Businger, 1986) to calculate HONO surface fluxes during the UBWOS studies. The gradient method assumes that atmospheric surface layer fluxes can be described using the product of the vertical gradient of the concentration of a compound, $(\frac{d\bar{c}}{dz})$,and the eddy diffusivity coefficient (K_c):

$$F_c = -K_c \frac{d\bar{c}}{dz}$$ (equation 3.4)

where the turbulent exchange coefficient K at a specific height (z) can be calculated using the Von Kaman constant ($k = 0.37$) (Telford and Businger, 1986), Monin Obhukov length (L), friction velocity (u^*), displacement height (D), and the dimensionless wind shear, which is a function of stability:

$$K = \frac{k \times u^* \times (z-D)}{\Theta\left(\frac{z}{L}\right)}$$ (equation 3.5)

$$\Theta\left(\frac{z}{L}\right) = \left(1 - \frac{16\,(z-D)}{L}\right)^{-\frac{1}{2}} \quad for\ \frac{z}{L} < 0$$ (unstable conditions)

(equation 3.6)

$$\Theta\left(\frac{z}{L}\right) = \left(1 + \frac{5\,(z-D)}{L}\right) \quad for\ \frac{z}{L} > 0$$ (stable conditions)

The displacement height was estimated using the zero-plane displacement height equation shown in Stanhill (1969):

$$\log(\mathrm{D}) = 0.9793 \log(h) - 0.1536$$ (equation 3.7)

where h is the vegetation height. The displacement height of eleven popular vegetation species in the Southern UB (mainly shrubs and grass; Butler and England, 1979) was calculated and averaged to obtain the D (0.39±0.17 m) used for the UBWOS 2012 study. The same D was used for UBWOS 2014, because the maximum snow depth (~ 0.145 m) was lower than the average height of the vegetation in the UB (0.55 m).

The uncertainty of K was calculated by propagating the random error of friction velocity, Monin-Obukhov length, and D.

By retrieving the vertical profiles of HONO in section 3.3, we were able to calculate the HONO gradients needed to determine HONO fluxes. First, the average

mixing ratios of HONO in two vertical boxes (named lower box and upper box) were calculated. The lower box extended from 2 m (height of the instrument agl) to 16 m agl (height of the anemometer agl) and upper box extended from 16 m to 40 m agl (maximum height difference between the upper light path and the ground). Coincidently, 16 m agl is also the geometric mean height of the boxes. The difference between the average HONO mixing ratios in each box is divided by the box average heights ($\bar{z}_{boxUpper}$ = 28 m, $\bar{z}_{boxLower}$ = 9 m):

$$\frac{d\overline{HONO}}{dz} = \frac{\overline{HONO}_{boxUpper} - \overline{HONO}_{boxLower}}{\bar{z}_{boxUpper} - \bar{z}_{boxLower}} \quad \text{(equation 3.8)}$$

The uncertainty of the HONO gradient was determined by propagating the uncertainty associated with the average concentration of HONO in the lower and upper box. Because the uncertainty of the HONO vertical profile is constant, the equation used to calculate the HONO gradient uncertainty was:

$$\frac{d\overline{HONO}}{dz} error = \frac{\sqrt{2}}{dz} \overline{HONO}_{boxLower}\, error \quad \text{(equation 3.9)}$$

Finally, HONO fluxes were calculated by multiplying K (equation 3.5) and $\frac{d\overline{HONO}}{dz}$ (equation 3.8). The uncertainty of HONO fluxes was calculated by propagating the uncertainties of the HONO gradient and K:

$$HONO\ flux_{error} = abs(HONO\ flux) \times \sqrt{\left(\frac{\frac{d\overline{HONO}}{dz}\ error}{\frac{d\overline{HONO}}{dz}}\right)^2 + \left(\frac{K_{error}}{K}\right)^2} \quad \text{(equation 3.10)}$$

HONO flux rates, which is the HONO formation rate from HONO flux in a box, was calculated by dividing HONO flux by H (the height of the box agl):

$$HONO flux\ rate = \frac{HONO\ Flux}{H} \quad \text{(equation 3.11)}$$

$$HONO\ flux\ rate_{\ error} = abs(flux\ Rate\ HONO) \times \sqrt{\left(\frac{HONO\ flux_{error}}{HONO\ flux}\right)^2 + \left(\frac{H_{error}}{H}\right)^2}$$

(equation 3.12)

3.3 Calculation of unknown HONO source ($P_{unknown}$)

We used a pseudo-steady state (PSS) approach, similar to that used in (Wong et al., 2012), to quantify the unknown source of daytime HONO. The photolysis frequencies of HONO, which show that HONO had a short lifetime of about half an hour in the early morning and less than 15 min at noon, justifies the use of the PSS approach (equation 3.13). It is assumed that HONO reaches a pseudo steady state between the known (equation 3.13a) and unknown ($P_{unknown}$) sources of HONO and loss rates of HONO (equation 3.13b and equation 3.13c) . Direct emissions of HONO are not considered in these studies because our measurements are not significantly influenced by traffic.

$$\frac{d[HONO]}{dt} = P_{unknown} + HONO_{formation} - HONO_{phtolysis} - HONO_{oxidation} = 0$$

(equation 3.13)

$$HONO_{formation} = k_{NO+OH}\,[NO][OH]$$ (equation 3.13a)

$$HONO_{photolysis-loss\,rate} = j_{HONO}\,[HONO]$$ (equation 3.13b)

$$HONO_{oxidation-loss\,rate} = k_{HONO+OH}\,[HONO][OH]$$ (equation 3.13c)

The bimolecular and termolecular reaction constants needed to calculate $HONO_{formation}$, $HONO_{oxidation}$, and $[OH]_{ss}$ were determined using Sander et al. (2011). Their uncertainty, as shown in Sander et al. (2011) were calculated based on the uncertainty of the rate constants measured at 298 K and an arbitrary factor that describes

the increase in uncertainty in K (due to fewer data and/or increasing measurement difficulties) when measuring at temperatures above or below 298. Sander et al. (2011) also shows that for most rate constants this uncertainty is symmetric with respect to temperature. However, in a few cases the rate constant uncertainties are asymmetric. In our calculations the only rate constant without an uncertainty factor below 298 K was $k_{HONO+OH}$. Burkholder et al. (1992) measured HONO + OH rate constants from 298 to 373 K and showed that there is a slight negative temperature dependence of HONO oxidation with temperature. $k_{HONO+OH}$ was calculated assuming that the uncertainty of HONO oxidation is symmetric therefore using the uncertainty factor above 298 K for temperatures below 298 K.

Table 3.1 Rate coefficient and rate coefficient uncertainty for HONO formation and at 275 K

Reaction	**Rate Coefficient**	**Rate coefficient (cm^3 $molecule^{-1}$ s^{-1}) T = 275 K**	**Uncertainty (cm^3 $molecule^{-1}$ s^{-1})**
$NO + OH \xrightarrow{M} HONO$	k_{NO+OH}	1.8×10^{-13} (P = 843.5)	4×10^{-14}
$HONO + OH \rightarrow H_2O + NO_2$	$k_{HONO+OH}$	4.3×10^{-12}	2.6×10^{-12}

Following equation 3.13, the unknown production of HONO, or $P_{unknown}$ was calculated using:

$$P_{unknown} = J_{HONO}[HONO] + k_{HONO+OH}[HONO][OH] - k_{NO+OH}[NO][OH]$$

(equation 3.14)

The uncertainty of $P_{unknown}$ was determined by propagating the errors calculated for each term:

$$P_{unknown\ error} =$$

$$\sqrt{HONO_{formation-error}{}^2 + HONO_{photolysis-error}{}^2 + HONO_{oxidation-error}{}^2}$$

(equation 3.15)

Chapter 4 HONO STUDY DURING UBWOS 2012

4.1 Introduction

The UBWOS 2012 study took place in the Uintah Basin located in the northeast corner of Utah where significant oil and gas production activities occur. The main site (known also as Horse Pool site) consisted of 6 trailers clustered around a sampling tower (a 20 m scaffold with an enclosure that contained instruments at about 10 m agl) and a tent that housed the UCLA LP-DOAS (Figure 4.1). The measurement period started on 15 January 2012 and ended on 29 February 2012. Many instruments, including the UCLA LP-DOAS, covered a shorter time period.

Figure 4.1 Horse Pool site during UBWOS 2012. Left panel shows Horse Pool site looking from South to North. Photo from Lyman and Shorthill (2013). Right panel shows the tent that housed the UCLA LP-DOAS during UBWOS 2012.

4.2 Ancillary measurements

Extensive chemical and meteorological measurements were made at the Horse Pool site. This section describes the supplemental measurements that were used in this study. A summary of all the UBWOS 2012 measurements can be found in the work of (Lyman and Shorthill, 2013).

4.2.1 Meteorological (NOAA – Earth System Research Laboratory) and Micrometeorological (NOAA-Physical Science Division) data

Temperature, relative humidity, wind direction, and wind speed were measured at the top (about 19 m agl) and 13.5 m agl of the sampling tower. Temperature and relative humidity were measured with a Vaisala model HMP45AC and pressure was measured with a Vaisala model PTB101B at 13.5 m agl. Wind direction and wind speed were measured with a RM Young, model 05103 (at 19 m agl) and a 3-dimensional sonic anemometer model 81000 (at 13.5 m agl). All the data are one-minute averages and the uncertainty was ± 3%.

Turbulent heat flux, Monin-Obukhov length, and friction velocity were calculated using micrometeorological data collected by a sonic anemometer installed at a site adjacent to Horse Pool site at16 m agl (Persson et al., 2002). Persson et al., 2002 estimated a random error of ± 3 W m^{-2} for turbulent heat flux and ± 0.05 m s^{-1} for friction velocity. No errors were reported for the Monin-Obukhov length in their study.

4.2.2 NO measurements (NOAA – Chemical Science Division)

NO_x measurements were made with a pair of O_3-NO chemiluminescence detectors. One of the detectors determined NO and the other measured NO plus a fraction of NO_2 that had been converted to NO by a photolytic converter. The total uncertainty of NO was determined to be 4% with a detection limit of 6 pptv (one minute average).

4.2.3 Photolysis rates (NOAA – Chemical Science Division)

Photolysis rates of NO_2 and O_3 (O^1D channel) were measured by commercial filter radiometers (Metcon, Inc.) mounted at about 10 m agl. The rates were measured at 1 Hz from 15 January until 22 February, when strong wind gust toppled the tower that held the instrument. Total uncertainties for one-minute average data were ±15% for jNO_2 and ± 25% for $jO(^1D)$. The uncertainty of jHONO was ±14%.

4.2.4 VOC measurements (NOAA – Chemical Science Division)

A complete set of volatile organic compounds (VOCs) was measured in-situ by a gas chromatograph-mass spectrometer instrument (GC-MS). The inlet of the GC-MS was set up at approximately 20 m agl. A total of 65 VOCs were measured including alkanes, alkenes, cycloalkanes, aromatics, oxygenated VOCs, and nitrogen and halogen containing species. Uncertainties were about 15-25% for hydrocarbons and 20-25% for oxygenates compounds. A detailed description of the instrument is described in the work of (Gilman et al., 2010) and (Goldan et al., 2004).

4.2.5 CH_4, CO, PAN, and HNO_3 measurements (NOAA-Chemical Science Division)

Carbon monoxide (CO) was measured with a commercial vacuum–UV resonance fluorescence instrument; the accuracy and precision of the CO measurements were ±4% and ±0.5 ppbv respectively.

Methane (CH_4) was measured by a wavelength-scanned cavity ring-down analyzer (Picarro 1301-m) (Crosson, 2008); the uncertainty was estimated to be ±1 ppbv for CH_4 mixing ratios between 1790 and 2500 ppbv and ±(0.2 ppb + 0.5% of CH_4 mixing ratio) for CH_4 mixing ratios greater than 2500 ppbv.

Acyl peroxynitrate (PAN) was measured by gas chromatography with electron capture detection GC/ECD (Flocke et al., 2005; Williams et al., 2000). Calibrations were done in field with acetone/NO photolysis sources (Flocke et al., 2005; Zheng et al., 2011). The overall uncertainty of PAN was ±(20% + 5 pptv).

Nitric acid (HNO_3) was measured by negative ion proton transfer chemical ionization mass spectrometry (NI-PT-CIMS), with acetate as the reagent ion. Acetic acid is usually the weakest gas-phase acid amongst the measured compounds, therefore acetate ion exchanges a proton with the organic and inorganic acids of interest forming an ion, which is detected by the NI-PT-CIMS. This method is described in detailed by (Roberts et al., 2010) and (Veres et al., 2008). The NI-PT-CIMS was placed on the tower at 10 m agl. HONO was also measured using this method; interferences in the HONO signal due to inlet effects from NO_2 in the presence of humidity were corrected using laboratory-determined responses. The uncertainties for both HNO_3 and HONO were ±20%.

4.2.6 Aerosol number size distribution (NOAA – Pacific Marine Environmental Laboratory)

Aerosol number size distribution was measured with a Scanning Mobility Particle Sizer (SMPS, TSI 3080 coupled to a TSI 3010 CN counter) and an Aerodynamic Particle Sizer (APS, TSI 3321). Aerosol particles were sampled about 12 m agl. The SMPS counted particles ranging from 20 nm to 50 nm geometric diameter; the APS collected particles into 34 size bins with aerodynamic diameters between 0.7 and 10.37 micrometers. The number size distributions were collected every 5 minutes.

4.3 Model Simulations

This study uses the outputs of two models for its data analysis: a one dimension chemical and transport model (RCAT 8.2, run for this study) and the Weather Research and Forecasting model coupled with Chemistry (WRF-Chem run by NOAA). This section gives a short description of both models.

4.3.1 Weather Research and Forecasting model coupled with Chemistry (WRF-Chem)

A recent version of the WRF-Chem model (version 3.5.1 http://ruc.noaa.gov/wrf/WG11/) was used to simulate O_3 levels during UBWOS 2012 (Ahmadov et al., 2015). The gas-phase chemistry mechanisms are based on the Regional Atmospheric Mechanism (RACM) (Stockwell et al., 1997) and the photolysis rates were simulated using the Tropospheric Ultraviolet and Visible (TUV) photolysis scheme (Madronich, 1987). The initial meteorological and boundary conditions were based on the North American Mesoscale analysis fields (www.emc.ncep.noaa.gov). This study makes use of the planetary boundary layer heights (PBLHs) and OH mixing ratios output from WRF-Chem. A detailed description of the model results for UBWOS 2012 can be found in (Ahmadov et al., 2015).

4.3.2 RCAT 8.2 chemical and transport model description

RCAT8.2 is a vertically resolved model based on a system of one-dimensional transport-kinetics equations. The change of trace gas concentrations is expressed as the sum of the rate of concentration change caused by vertical flux, total chemical production, total chemical loss, and the emission of the compound; concentration changes by advection are neglected in the model. The vertical transport of inert or slowly reacting gases is calculated using a first order linear flux-gradient relationship where the vertical flux only depends on the vertical concentration gradient of the gas and the altitude dependent eddy diffusivity (Dearellano et al., 1995; Fitzjarrald and Lenschow, 1983). In the case of NO, RCAT8.2 uses a modified eddy diffusivity model (Hamba, 1993) that simulates the vertical transport of NO considering both the NO vertical concentration profile and the concentration profiles of the gases that it reacts with. The vertical profile of eddy diffusivity coefficients are calculated using Monin-Obukhov similarity theory (Stull, 1988). Laminar diffusion is considered near the surface and effects of surface structures are parameterized by surface roughness and the displacement height. RCAT 8.2 includes the RACM which contains 77 species and 237 reactions and aggregates atmospheric VOCs into 23 classes: 4 alkanes, 4 alkenes, 3 biogenic, 3 aromatics, and 9 carbonyls (Stockwell et al., 1997). RCAT8.2 also includes biogenic and anthropogenic emissions and the Mainz Isoprene Mechanism (MIM) (Geiger et al., 2003). The aerosol uptake rates in RCAT 8.2 are calculated using the mass-transfer equation by (Fuchs and Sutugin, 1970). Uptake rates were calculated based on the vertical profile of the aerosol surface to air volume ratio and a particle diameter of 150 nm. Interactions of gases with the ground are modeled through direct molecular interactions.

4.3.2.1 RCAT 8.2 model initialization

RCAT8.2 was run for all sunny days and was set up to subdivide the lowest 2000 m into 23 boxes with logarithmic spacing below 1 m to account for the inefficient vertical transport near the ground. The box altitudes were $1x10^{-4}$, $1x10^{-3}$, $1x10^{-2}$, 0.1, 1, 2, 6, 10, 20, 33, 47, 70, 90, 110, 121, 150, 175, 255, 300, 556, 750, 1000 and 2000 m. Vertical fluxes and other meteorological parameters were calculated based on hourly varying temperatures (from NOAA in-situ measurements), PBLs heights (WRF-Chem model), Prandtl layer heights, and wind speeds at 50 meters (WS50). The stability of the atmosphere was assumed to be neutrally stable. The canopy height was set to 3 m; the displacement height was set to 4.27 m, and the surface roughness length was 0.03 m. The chemistry portion of the model was initialized at sunset with NOAA in-situ measurements of hydrocarbons (HCs), CO, CH_4, and PAN, and UCLA LP-DOAS measurements of NO_2, O_3, HCHO, HONO, and SO_2. The initial concentrations of the trace gases changed depending on the modeled day, with sunny days averages at sunset of 2320 ppm for CH_4, 92.68 ppb for alkanes, 4.09 ppb for aromatic VOCs, 1.57 ppb for carbonyls, 0.45 ppb for PAN, and negligible biogenic VOC. Because the purpose of this model is to study HONO chemistry, the hourly NO emissions in the 0.1- 1 m height box were constrained to reproduce the LP-DOS NO_2 observations in the lower light path. The hourly aerosol surface area density diurnal values were calculated using Scanning Mobility Particle Sizer (SMPS) and Aerodynamic Particle Sizer (APS) measurements. The aerosol surface vertical profiles were assumed to be constant up to the PBL height and decreased exponentially, to one-third of its surface concentration, above the PBL. Soil NO emissions were assumed to be $1x10^{10}$ molecules cm^{-2} s^{-1}. The aerosol and

ground uptake coefficients adopted in RCAT 8.2 were $2x10^{-3}$ for NO_3, $2x10^{-5}$ for NO_2, 10^{-4} for HONO, 0.1 for HO_2 and $5x10^{-5}$ for O_3.

4.4 Results

4.4.1 Meteorology during UBWOS 2012

Snow cover was almost absent during UBWOS 2012; only two small snow events were observed (on 19 and 29 February), which left about an inch of snow on the ground. During these periods, the surface albedo at Horse Pool increased from its average of 0.25 to above 0.3.

UBWOS 2012 was dominated by weak-wind periods (< 4 m s^{-1}) (Figure 4.2) with average wind speeds ranging between 2.5 m s^{-1} during the night to 4 m s^{-1} in the evening (Figure 4.3b). Lidar observations shows that for most of the light-wind days at Horse Pool, easterly flows occur at night and westerly upslope flow occur during the day. During strong-wind periods, large-scale meteorological systems dominated the wind fields with stronger winds aloft driving the near-surface winds.

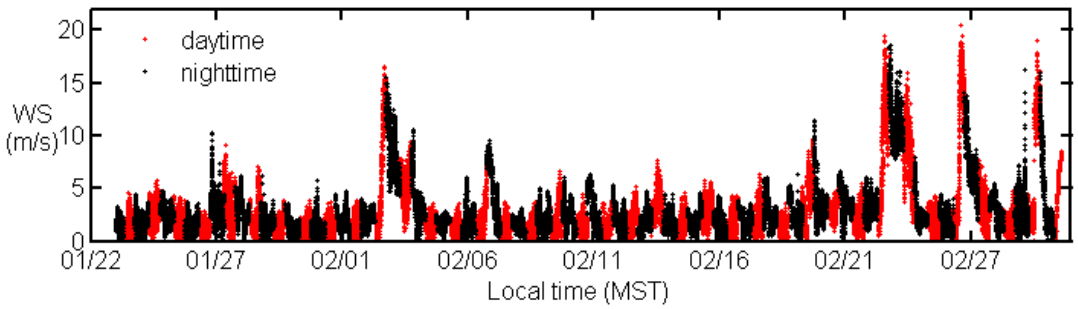

Figure 4.2 Time Series of Horse Pool wind speed measured 19 m agl by NOAA. Daytime is between 0700 – 1800 hours (red) and nighttime is between 1800 – 0700 hours (black).

Horse Pool temperatures ranged between 259K and 286K with hourly average temperature varying between 270 K in the early morning and 277 K in the mid afternoon (Figure 4.3a). Hourly average relative humidity (Figure 4.3c) decreased from about 68% in the early morning to 39% in the mid afternoon. Temperature measurements across the UB showed that daytime temperature inversions conducive for ozone formation were rare.

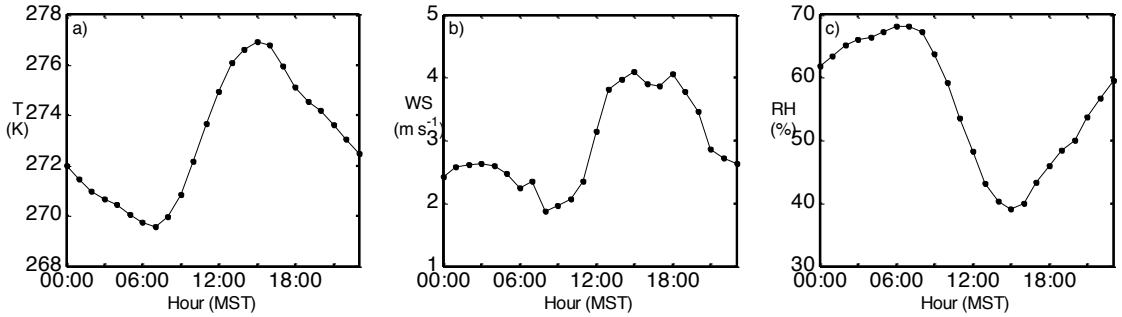

Figure 4.3 Hourly average meteorological data measured by NOAA: (a) temperature measured at 13 m agl, (b) wind speed measured at 19 m agl, and (c) relative humidity measured at 13 m agl.

4.4.2 NO_2, O_3, and HONO light path average mixing ratios

NO_2, O_3, and HONO were measured continuously on all three light paths except for short intervals when the instrument was misaligned or the visibility was low. Figure

4.4 shows an overview of NO_2, O_3, and HONO path-averaged concentrations.

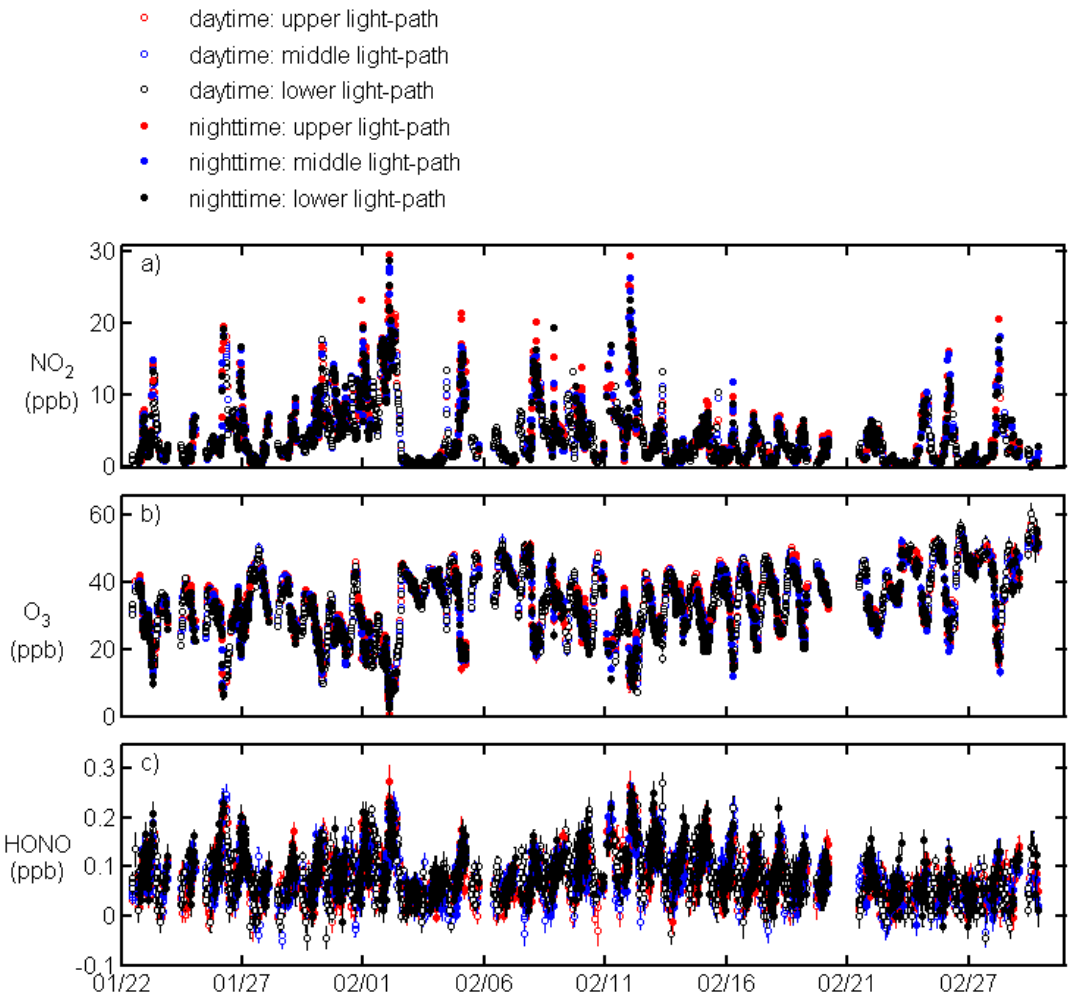

Figure 4.4 Lower, middle, and upper LP-DOAS light paths averages of (a) NO_2, (b) O_3, and (c) HONO during UBWOS 2012.

Daytime and nighttime NO_2 mixing ratios were on average about 2 ppb and ranged from 0.10 ± 0.069 ppb to 28.84 ± 0.078 ppb in the lowest light path. While these high levels of NO_2 are comparable to NO_2 levels found in some polluted urban areas, their sources are different. In general, transportation is the main source of NO_2 pollution

in urban areas, but in the UB NO_x was mainly emitted from oil and gas operations (57-61%) followed by emissions from a Power Plant (33-36%) (Lyman and Shorthill, 2013).

Comparison of wind speed (Figure 4.2) and NO_2 mixing ratios show that NO_2 tends to built up within the basin during periods of light winds and drops significantly under high wind episodes; for example, NO_2 mixing ratios gradually accumulated in the basin from 28 January to 2 February, when most of the wind speeds were below 5 m s^{-1}; then, around noontime of 2 February, as wind speed increased to 15 m s^{-1} (Figure 4.5a), NO_2 mixing ratios dropped from about 28 ppb to below 1 ppb (Figure 4.5b).

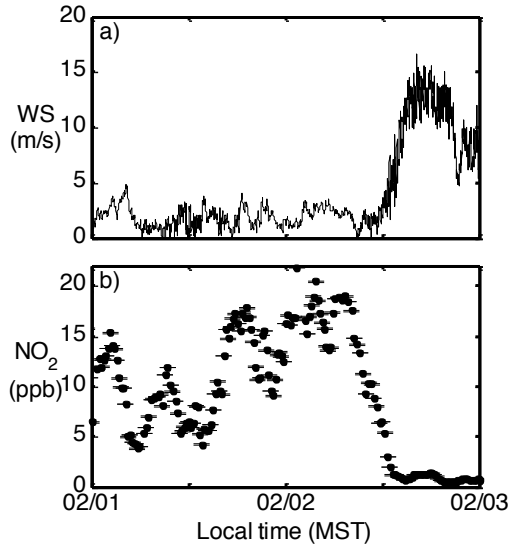

Figure 4.5 Wind speed and NO_2 mixing ratios measured from 1 February to 3 February 2012. (a) Wind speed measured at 13 m agl. (b) LP-DOAS lower light path NO_2 mixing ratios.

O_3 levels during UBWOS 2012 were considerably lower than levels observed in polluted urban areas in summertime, with O_3 mixing ratios measured in the lower light

path ranging from 2.43±1.7 ppb to 60.45±3.3 ppb (Figure 4.4b). O_3 levels measured in the UB in 2012 were also lower than O_3 levels measured in the UB in the previous two winters. While the O_3 8-hr maxima were 124 ppb and 139 ppb and the number of NAAQS O_3 exceedances were 36 and 25 during the winter of 2009-10 and 2010-11 respectively, the O_3 8-hr maximum during UBWOS 2012 was 63 ppb and no O_3 exceedances were encountered. Unlike the two previous winters, meteorological conditions during UBWOS 2012 were not conductive for snow formation and daytime temperature inversions were rare, resulting in consistently low ozone levels.

HONO levels (Figure 4.4c) were also low compared to HONO levels measured in polluted urban areas in summertime. The nighttime and daytime path-averaged HONO mixing ratios were 78 ppt and 56 ppt respectively and HONO measured in the lower light path ranged from below the detection limits to 274 ± 33 ppt. These HONO levels are comparable to those measured in a rural area in New York, about 60 ppt of daytime HONO (Zhou et al., 2002), but lower than HONO levels measured in polluted environments. For example, VanderBoer et al., (2013) measured about 100 pptv of HONO in a semi-urban area in Boulder CO, Wong et al., (2012) measured about 250 pptv of daytime HONO in Houston Texas, and Su et al., (2008) measured up to 1 ppb of HONO in a polluted rural area in South Eastern China.

4.4.3 Diurnal profile of NO_2, O_3, and HONO mixing ratios

To examine the diurnal trend and vertical gradients of O_3, NO_2, and HONO, the mixing ratios of these trace gases were hourly averaged. Figure 4.6 shows the diurnal profile of NO_2 (Figure 4.6a), O_3 (Figure 4.6b), and HONO (Figure 4.6c) on each light

path (lower light path in black, middle light path in blue, and upper light path in red) and their respective 1σ spread (represented by the grey shadow).

NO_2 diurnal profile (Figure 4.6a) indicates that Horse Pool was influenced predominantly by stationary rather than mobile sources. NO_2 mixing ratios shows a slow build-up at night that continues until morning when daytime atmospheric mixing starts. The lowest hourly average NO_2 mixing ratios (about 2.6 ppb) were observed in the late afternoon when atmospheric mixing was the greatest; maximum hourly average NO_2 was observed around midnight (6.5 ppb). While NO_2 shows no gradients during the day, it exhibits positive gradients during the night. The absence of daytime gradient was likely due to enhanced daytime vertical mixing, which reduced NO_2 gradients below the LP-DOAS detection limit. The NO_2 nighttime gradient is most likely the result of ground deposition.

O_3 diurnal profile (Figure 4.6b) follows its photochemical formation trend reaching maximum O_3 levels (about 41 ppb) in the afternoon and minimum levels (about 25 ppb) in early morning. During the day, O_3 did not exhibit vertical stratification due to well-mixed daytime atmospheric conditions; during the night, O_3 depletions of about 20 ppb occur frequently; most likely due to surface deposition (Sillman, 1999).

HONO diurnal profiles (Figure 4.6c) show a distinctive decrease after sunrise due to its efficient photolysis and daytime mixing. After sunset, HONO forms through heterogeneous reactions and accumulates slowly throughout the night. Maximum hourly average HONO levels of 120 ppt were observed in the early morning (at about 0600 hours) and minimum HONO levels of 50 ppt were observed in the late afternoon (around 1600 hours). These HONO mixing ratios are lower than HONO levels measured in most

polluted urban areas; for example, during CalNex 2010, which took place in Los Angeles, UCLA LP-DOAS measured about 100 ppt of daytime HONO on its lowest light path (33-78 m agl).

The complex terrain of the UB and low daytime HONO mixing ratios near the Horse Pool site made measurement of HONO challenging. HONO mixing ratios were often within the detection limits and varied drastically from data point to data point resulting in HONO gradients to alternate between positive and negative values. Despite of this, the hourly average diurnal profile of HONO show, in general, higher HONO mixing ratios in the lower than in the upper light path, for both day and night (Figure 4.6c). A possible explanation for the HONO gradient observed in Figure 4.6c is the presence of a surface HONO source.

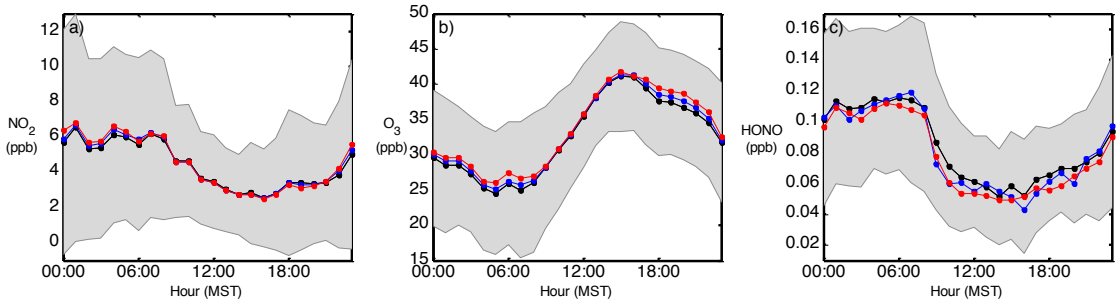

Figure 4.6 Hourly average light path averaged mixing ratios of (a) O_3, (b) NO_2, and (c) HONO in the lower (black), middle (blue), and upper (red) light paths throughout the study. Grey shadow shows 1σ spread of average value.

4.4.4 HONO vertical profiles

In this study, the HONO analysis was performed for sunny days (27 January, and 17 February, 6 February, 7 February, and 17 February) when the photolytic lifetime of HONO was about 13 minutes at noon and the steady state assumption can be applied. In comparison, the average photolytic lifetime of HONO for the entire study was about 21 minutes at noontime and the lifetimes of HONO on sunny days increased significantly before 0900 (from about 52 minutes to about 21 minutes between 0800 and 0900 hours) and decreased after 1500 (from about 19 minutes to 46 minutes from 1500 to 1600 hours).

HONO vertical profiles were retrieved using the least square minimization method described in section 3.1. The retrieved sunny days HONO vertical profiles were averaged hourly (from 1100 to 1500 hours) and plotted in Figure 4.7. HONO vertical profiles show higher HONO mixing ratios near the surface than aloft and a rapid decay of HONO mixing ratios above 100 m agl. HONO mixing ratios decrease as the day progresses due to photolysis and vertical mixing.

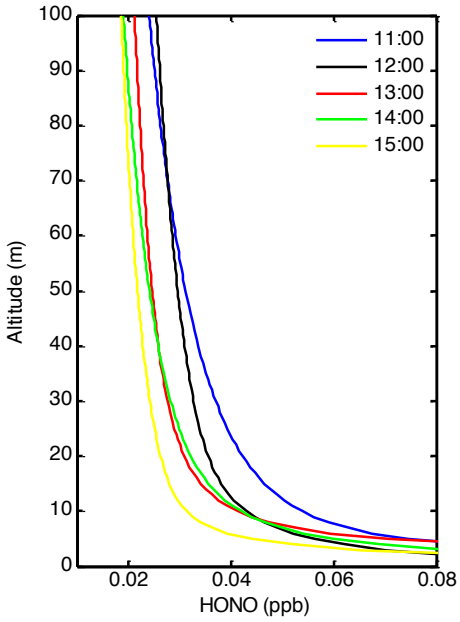

Figure 4.7 Sunny days hourly average retrieved vertical profiles of HONO using least square fitting methodology.

4.4.5 HONO fluxes

HONO fluxes were calculated using the gradient method described in section 3.2 of the thesis. The equations to calculate eddy diffusivity coefficients (K) (equation 3.5) and HONO gradients (equation 3.8) can also be found in section 3.2. The eddy diffusivity coefficient was calculated at 19 m agl using friction velocities (u^*) and Monin Obhukov lengths (L) derived by NOAA. With the exception of a few days (when u^* reached up to 1 m/s), u^* peaked around noontime with an average of about 0.3 m s^{-1} (Figure 4.8a). Monin Obukhov lengths varied significantly day-to-day ranging from -514 to 519 m during the daytime (Figure 4.8b).

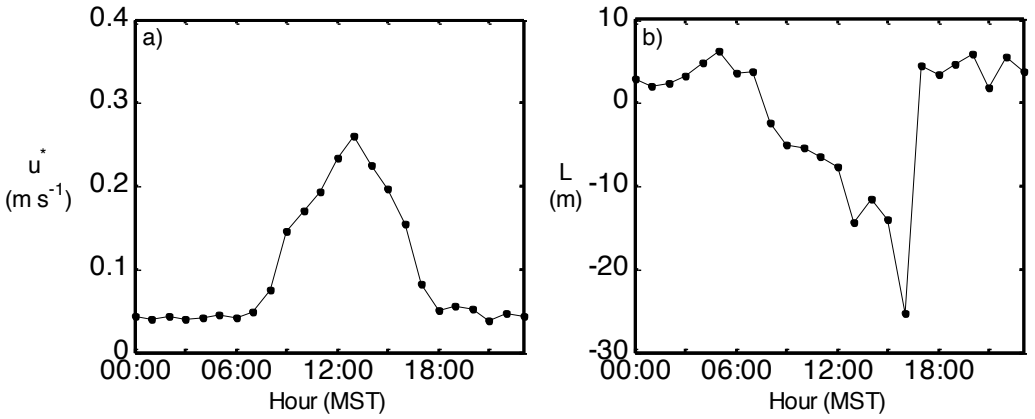

Figure 4.8 Hourly median (a) friction velocity and (b) Monin Obukhov lengths measured at 16 m agl.

The eddy diffusivity coefficient (K), HONO gradient, and HONO fluxes calculated for one of the sunny days (6 February, 2012) are shown in Figure 4.9. The

HONO flux on this day was relatively high, with a maximum of $(4.9\pm0.2)\times10^{10}$ molec. cm^{-2} s^{-1} near noontime. The hourly average sunny days HONO fluxes were also calculated and are shown in Figure 4.10. The average sunny days HONO flux somewhat follows solar irradiance, with a maximum of $(1.7\pm0.3)\times10^{10}$ molec. cm^{-2} s^{-1} occurring at noontime. This value is comparable to the average HONO flux (about 1.15×10^{10} molec. cm^{-2} s^{-1}) measured above a northern Michigan forest canopy (Zhang et al., 2009 and Zhou et al., 2011) and lower than average noontime HONO flux (3.01×10^{10} molec. cm^{-2} s^{-1}) measured over an agricultural field in Bakersfield (Ren et al. 2011). The upward HONO fluxes observed during sunny days supports the idea that daytime HONO formation occurs at the ground.

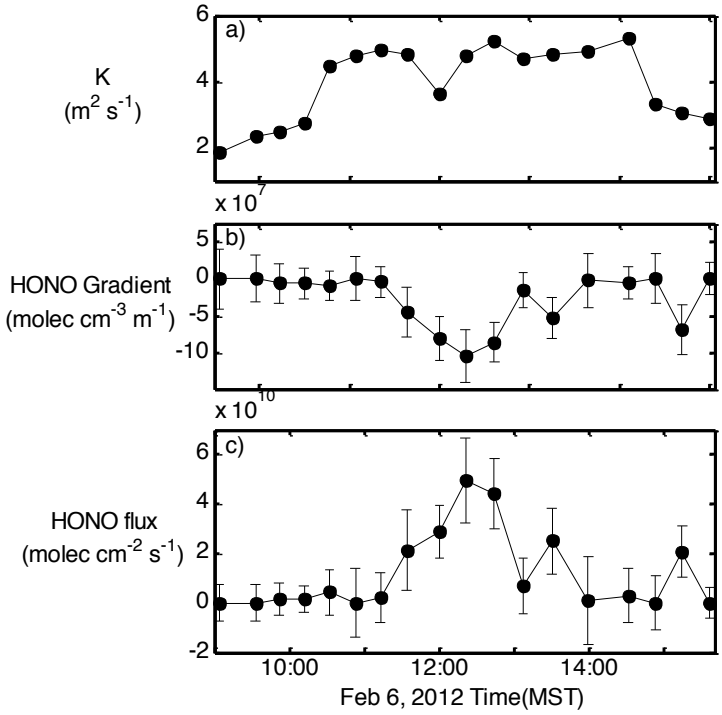

Figure 4.9 Calculated (a) eddy diffusivity coefficients, (b) HONO gradients, and (c) HONO flux on 6 February 2012.

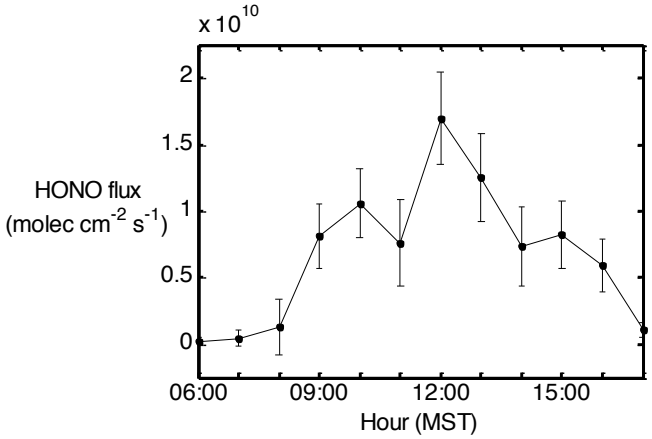

Figure 4.10 Sunny days hourly average HONO fluxes during UBWOS 2012.

4.4.6 HONO daytime sources

Similar to numerous field studies, the measured daytime HONO levels exceeded that of its photochemical steady state levels. The difference between the calculated $HONO_{ss}$ (Figure 4.11 red line) and HONO measured in the lowest light path (Figure 4.11 black line) points towards the presence of an unknown HONO source during the day. The production rate of this unknown daytime source ($P_{unknown}$) was calculated using the pseudo-steady state approach described in Chapter 3, section 3.3.

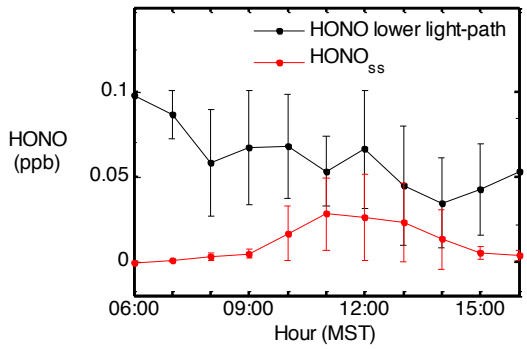

Figure 4.11 Sunny days hourly average lower light path HONO (black) and sunny days hourly average $HONO_{ss}$ (HONO steady-state concentration) calculated using equation 1.1.

The HONO production and loss rates were calculated using in-situ NO measurements, jHONO derived by NOAA, and lower light path LP-DOAS HONO mixing ratios. Due to the lack of OH in-situ measurements, we used the surface OH mixing ratios outputted by WRF-Chem (section 4.2.7). An uncertainty of 20% was assigned to the WRF-Chem OH mixing ratios. This number was obtained by calculating the percent difference between OH mixing ratios output from RCAT 8.2 and WRF-Chem during sunny days. The uncertainties of the formation and loss rates of HONO and $P_{unknown}$ were calculated by propagating the uncertainties of their rate constants and measurements errors (Chapter 3, section 3.3).

Figure 4.12 shows the sunny days hourly average of $HONO_{formation}$ (red line), $HONO_{photolysis}$ (green line), $HONO_{oxidation}$ (blue line), and $P_{unknown}$ (black line). To determine whether surface fluxes of HONO can explain the calculated $P_{unknown}$, the sunny days HONO fluxes shown in section 4.4.5 were converted into column HONO flux rates (Figure 4.12, magenta line) by dividing HONO fluxes by H, the height at which the

influence of HONO surface fluxes on the total HONO column becomes negligible (equation 3.9).

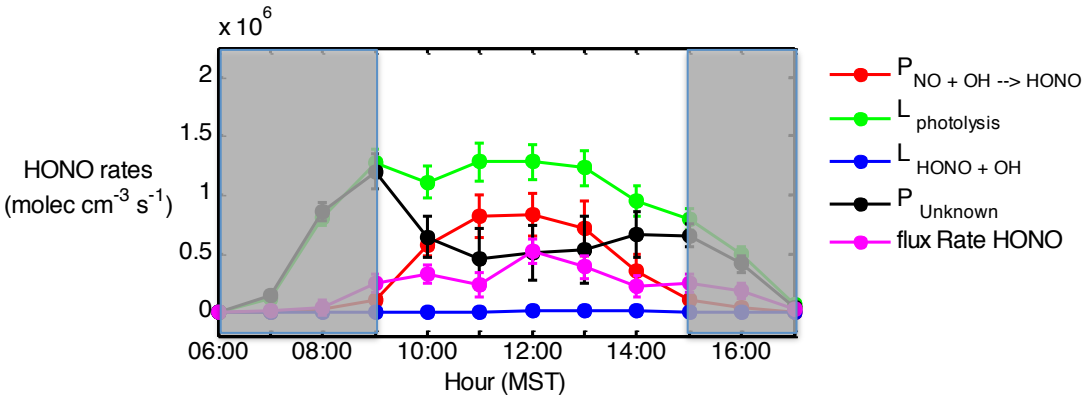

Figure 4.12 Sunny days hourly average HONO rates. HONO production (red line, equation 3.13a), HONO photolysis (green line, equation 3.13b), HONO oxidation (blue line, equation 3.13c), $P_{unknown}$ (black line, equation 3.11) and HONO flux rate (magenta line, equation 3.11). Grey boxes show the time range when the pseudo-steady state assumption was not valid.

To determine height (H), two RCAT 8.2 model runs for 27 January were performed, one with and one without HONO surface fluxes (the model runs are described in section 4.4.7). For each hour, an H was set at the height where the difference between the HONO modeled with and without HONO surface fluxes was less than 1 ppt (Figure 4.13). The average H between 0900 and 1500 hours (273±113 m) was used for the calculation of the HONO surface flux rate. The uncertainty of H is the 1 σ deviation of H from 0900 to 1500 hours. The uncertainty of HONO flux rate was calculated by propagating the uncertainty of HONO flux and H.

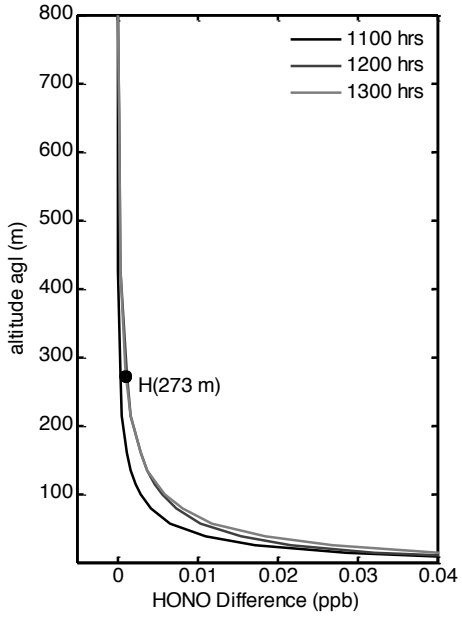

Figure 4.13 Shows height H (black dot). The vertical profiles are the differences between HONO mixing ratios modeled with HONO surface flux and the HONO mixing ratio modeled without HONO surface flux.

The height H is validated by the vertical transport profile of HONO (Figure 4.14; magenta line), which shows that vertical transport plays an important role up to about 200 meters agl. In addition to vertical transport, Figure 4.14 also shows the different HONO production and loss rates. According to the model, the main loss mechanism of HONO, as expected, is its photolysis.

Figure 4.12 shows one of the main findings in this study, when the steady-state approach is valid, the daytime HONO flux rate and missing HONO source agree within the errors near noontime, indicating that missing daytime HONO is formed through a photolytic formation pathway at the ground.

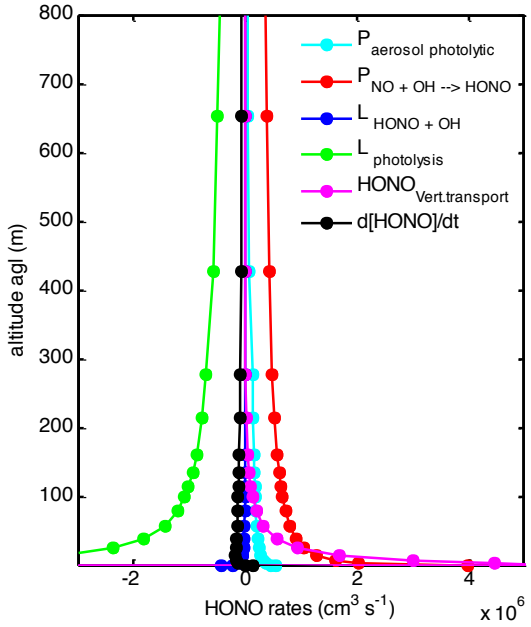

Figure 4.14 Modeled Vertical profiles of HONO loss rates (green line: HONO photolysis; blue line: HONO oxidation), HONO production rates (red line: NO oxidation, cyan line: aerosol photolytic pathway), HONO vertical transport (magenta line), and HONO total rate (black line) for 27 January 2016.

4.4.7 RCAT 8.2 model runs

The main purpose of using RCAT 8.2 in this study was to help understand how HONO changes with altitude and distinguish its different formation processes rather than to model the entire boundary layer chemical system. Three types of scenarios were run for this study: base, photolytic, and HONO flux.

The base scenario included direct emissions of HONO from cars between 0.1 and 1 m altitude (emission ratio of HONO/NOx = 0.008; Kurtenbach et al., 2001), gas phase formation of HONO from reaction of NO with OH and dark conversion of NO_2 on aerosol and ground surfaces (with a yield of 50%; Trick 2004), and HONO loss reactions

which included HONO photolysis, reaction with OH, and uptake on aerosol and ground surfaces (with reactive uptake coefficients of 10^{-3} and $2x10^{-5}$ respectively; Wong et al., 2011). Photo-enhanced conversion of NO_2 was no included in this model run.

The HONO flux scenario consisted of adding the calculated hourly average sunny days HONO fluxes (4.15) to the base scenario. The HONO surface flux was included in the model as a ground surface release, which was multiplied by a constant factor, f, to account for the difference between HONO fluxes at the surface and at 19 m agl, height at which HONO fluxes were calculated. To ensure that the HONO flux was described correctly in the model, factor f was adjusted to make the modeled (red line in Figure 4.15 lower panel plots) and calculated (black line in Figure 4.15 lower panel plots) HONO fluxes comparable. The modeled HONO flux was calculated using the gradient method (equation 3.4) shown in section 3.3. The modeled HONO gradient (equation 3.7) and eddy diffusivity coefficient (equation 3.5) were determined using the 1-D model outputs. As expected, the HONO flux model run (green line) shows higher levels of HONO than the base model run (blue line). Factor f was150 for both 27 January and 4 February model runs.

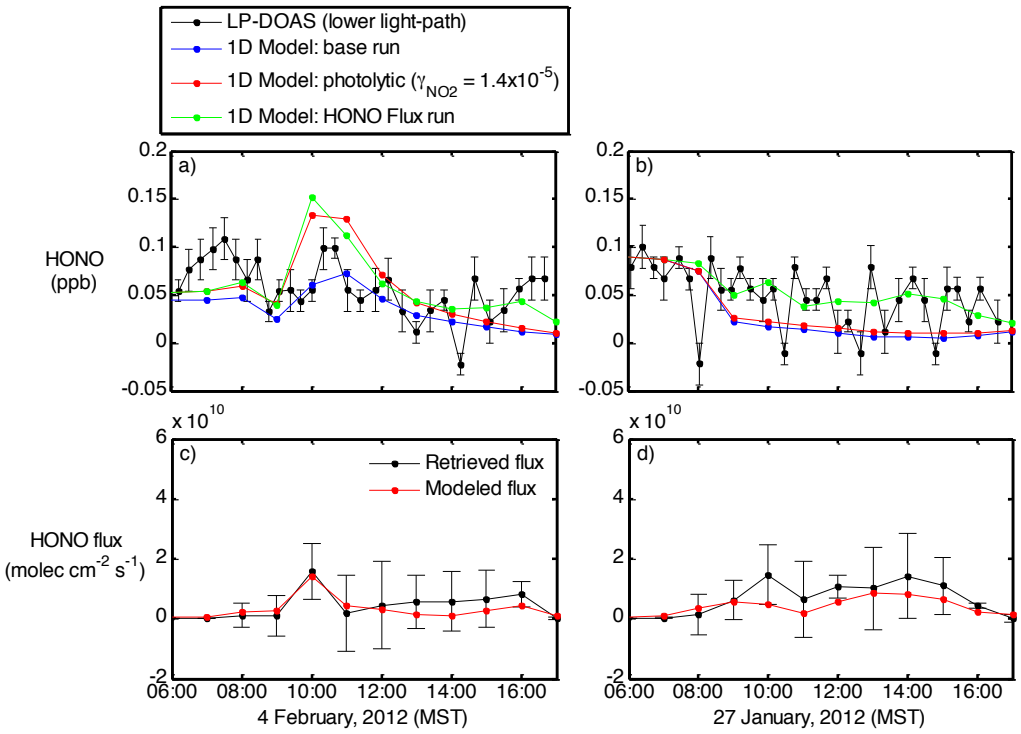

Figure 4.15 Top panels compare DOAS lower light path HONO mixing ratios with HONO mixing ratios outputted by three 1-D model runs: a base run (blue line and dots), a photolytic run with $\gamma_{NO2} = 1.4\text{x}10^{-5}$ (red line and dots), and a HONO flux run (green line and dots). Lower panels compare retrieved HONO fluxes (black) with modeled HONO fluxes at 19 m agl (red). Left panels show results from 4 February 2016 and right panels show results from 27 January 2012.

Figure 4.16 shows the sunny days hourly average HONO vertical profiles (thick lines) and modeled hourly average vertical profiles of HONO for 27 January and 4 February (dotted lines). The modeled HONO vertical profiles compare very well to the retrieved HONO vertical profiles, showing higher mixing ratios near the surface than aloft.

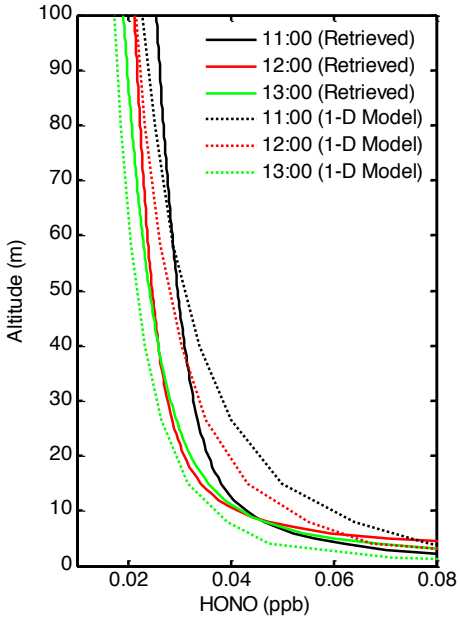

Figure 4.16 Hourly average retrieved vertical profiles of HONO using least square fitting methodology (solid lines) for Feb 7, 2012 near noontime. Modeled vertical profiles of HONO at near noon using 1-D model (dotted lines).

Finally, the photolytic scenario consisted of adding a photolytic surface source of HONO to the basic scenario. We used Wong et al., (2012) parameterization of the reactive uptake coefficient of NO_2 (γ_{NO_2}), which describes the photo-enhanced conversion of NO_2 on ground and aerosol surfaces using:

$$\gamma_{NO_2\ ground} = 6\times10^{-5} \cdot \frac{{J_{NO_2}}^3}{{J_{NO_2\ noon}}^3} \qquad \text{(equation 4.1)}$$

$$\gamma_{NO_2\ aerosol} = 4\times10^{-4} \cdot \frac{J_{NO_2}}{J_{NO_2\ noon}} \qquad \text{(equation 4.2)}$$

Their parameterization is solar irradiance dependent and the multiplicative factors in their equations were chosen based on their observations. Their NO_2-to-HONO uptake coefficient of $6\text{x}10^{-5}$ is larger but on the same order of magnitude to the one we

calculated for UBWOS 2012 of (1.4±1)x10^{-5} using equation 4.3, which was comparable to the laboratory values of 2x10^{-5} reported by Stemmler et al., (2006). The 2012 sunny days daytime average $\gamma_{NO_2\ ground}$ was calculated using the lower light path NO_2 mixing ratios, molecular speed of NO_2 at 275 K (the average noontime temperature in 2012), and calculated HONO flux.

$$\gamma_{NO_2\ ground,noon} = \frac{FluxHONO}{\frac{1}{4}\times[NO_2]\times\overline{v_{NO_2(275K)}}} \qquad \text{(equation 4.3)}$$

Figure 4.15 shows HONO mixing ratios outputted by the photolytic model run ($\gamma_{NO_2\ ground}$ = 1.4x10^{-5}) for 4 February (red line in February 4.15a) and 27 January (red line in Figure 4.15b).

4.5 Discussion

During UBWOS 2012, the diurnally average mixing ratios of daytime HONO in the 2-70 m vertical height interval (or LP-DOAS upper height interval) ranged from 35 to 81pptv, with an average of 48 pptv (Figure 4.6). These HONO levels are comparable to HONO observed in rural areas (Zhou et al., 2012) but lower than those observed in polluted urban environments (VanderBoer et al., 2013; Wong et al., 2012).

Daytime vertical profiles of HONO (Figure 4.7) show higher levels of HONO near the surface than aloft. This is in agreement with HONO observations made in Boulder, Colorado (VandenBoer et al., 2013) where they measured daytime mixing ratios of about 100±80 pptv at the surface and 35 pptv aloft. Measurements made in Houston, Texas (Wong et al., 2012) also show higher levels of HONO near the surface than aloft. These HONO vertical profiles indicate that there is a ground surface source of daytime

HONO, with the possibility of positive HONO flux from the surface. This theory is supported by our calculated sunny day HONO fluxes, which exhibited noontime upward fluxes ranging from negligible to (4.4±1.6) $x10^{10}$ molec. cm^{-2} s^{-1} with an average of $1.5x10^{10}$ molec. cm^{-2} s^{-1}. Our hourly average HONO flux exhibits a strong daytime variation pattern, with the maximum at solar noon. Zhou et al., (2011) showed similar HONO flux patterns in their study.

Two studies used HONO flux measured with Relaxed Eddy Accumulation (REA) systems to identify potential sources of daytime HONO. Zhou et al., (2011) measured HONO flux at about 11 m above a forest canopy in Michigan during the summer 2008. Their observed HONO flux correlated positively (R^2 = 0.69) with the product of photolysis rate constant of HNO_3 on leaf surfaces and leaf surface nitrate loading, suggesting that the photolysis of nitric acid on forest canopies is a significant daytime source of HONO to the lower atmosphere in low NO_x rural environments. On the other hand, Ren et al., (2011) measured the HONO flux 18 m agl above an agricultural field in Bakersfield California during the spring of 2010. Their daytime HONO flux showed a strong correlation (R^2 = 0.985) with the product of NO_2 concentrations and solar radiation instead. They concluded that the reduction of NO_2 involving sunlight might be an important HONO source in polluted and semi-polluted environments.

Comparison of our calculated HONO flux, with the product of NO_2 mixing ratios and visible solar irradiance, and the product of gas phase HNO_3 mixing ratios and UV solar irradiance (Figure 4.17) show that they have similar variation patterns and that they share the same diurnal variation trend as solar irradiance, that is they peak at solar noon. Positive HONO fluxes point to HONO being formed at the ground (rather than in the gas

phase or on aerosols); therefore, HONO fluxes were compared to solar irradiance instead of photolysis rates (Wong et al., 2012). Because nitrate species absorb in the UV range and UV solar irradiance was not measured in this study, their values were estimated by scaling visible solar irradiance with the measured $jHNO_3$ and jNO_2 ($UVSolarRad = SolarRad \times \frac{j_{HNO_3}}{j_{NO_2}}$). Also, due to the lack of NO_2 and HNO_3 surface measurements, it was assumed that gas-phase and surface NO_2 and HNO_3 were in equilibrium, thus gas phase NO_2 and HNO_3 were used as proxy of surface NO_2 and HNO_3 concentrations.

Daytime HONO flux strongly correlate with both [NO_2] x solar radiation (R^2 = 0.58) (Figure 4.18b) and [HNO_3] x UV solar radiation (R^2 = 0.66) (Figure 4.18a) making it difficult to determine whether the observed HONO flux is from photo-enhanced reduction of NO_2 on the surface, photolysis of surface HNO_3, or both.

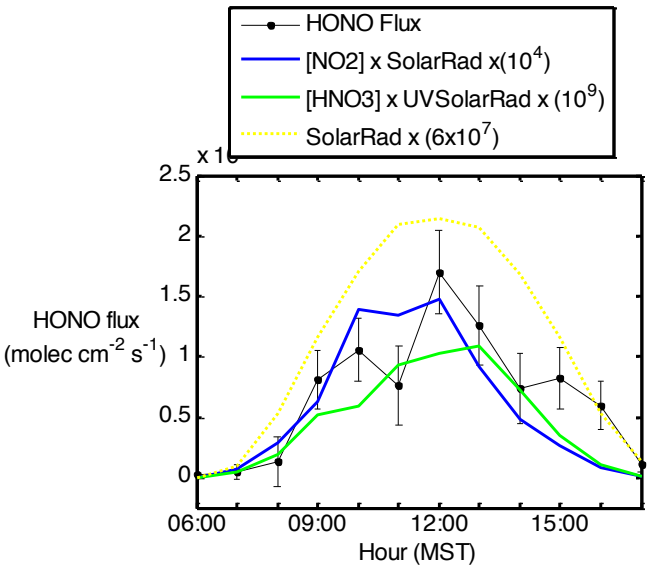

Figure 4.17 shows sunny days hourly average HONO fluxes (black dots and line), product of NO_2 mixing ratios measured in the lowest light path and solar radiation (blue line), product of gas-phase nitric acid and UV solar radiation (green line).

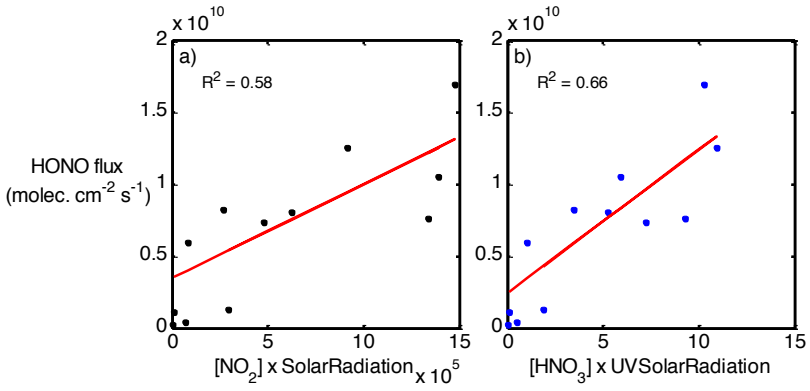

Figure 4.18 Correlation plots of (a) HONO flux vs. [NO_2] x solar radiation and (b) HONO flux vs. [HNO_3] x UV solar radiation.

A large plume event on 4 February at the horse pool site provided us the opportunity to examine the photo-enhanced NO_2 conversion at the ground as a potential HONO formation pathway. Comparison between NO_2 and SO_2 mixing ratios measured in the lower light path (Figure 4.19a) shows tight correlation (R^2 = 0.99; Figure 4.19b) between NO_2 and SO_2 suggesting that the source of the plume produces both of these trace gases. Furthermore, analysis of the composition of this plume shows that the plume had not aged significantly and aircraft measurements (made by GMD) show CO levels consistent with levels observed in coal-fired power plants, hence it was concluded that

the plume came from the Bonanza power plant (Lyman and Shorthill, 2013).

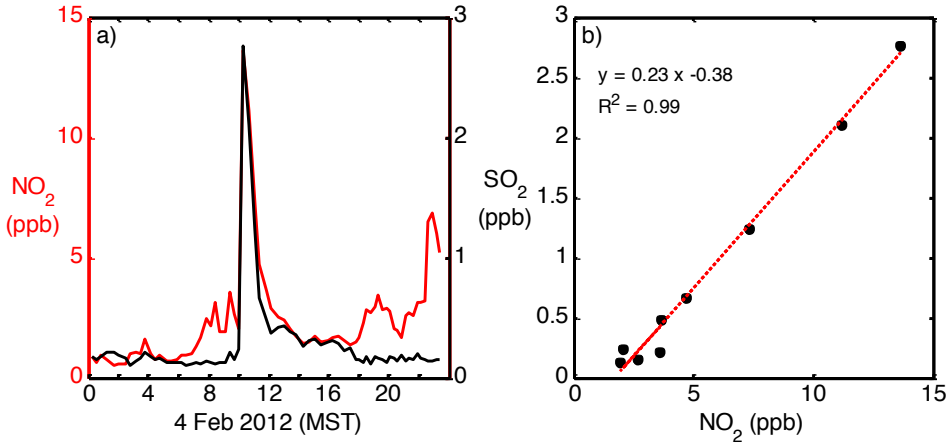

Figure 4.19 LP-DOAS NO_2 and SO_2 lower light path average mixing ratios. (a) Time series of NO_2 (red line) and SO_2 (black line) from 4 February 2012 to 5 February 2012. (b) Correlation plot between NO_2 and SO_2 with linear fit (red line), fit equation, and R^2 displayed on the plot.

We observed a peak of HONO mixing ratios (Figure 4.20c) and HONO flux (Figure 4.20c) that coincided with a peak of NO_2 on 4 February around 1000 hours. The correlation of HONO mixing ratios, HONO flux, and NO_2 mixing ratios and the absence of gas-phase HNO_3 peak at this time suggest that the source of the HONO peak was from the ground and that it involved NO_2 molecules. Furthermore, comparison of measured and modeled (RCAT 8.2 base run - Figure 4.20c blue line) HONO mixing ratios indicate that an additional HONO source is needed to account for the observed HONO peak. To determine whether photo-enhanced conversion of NO_2 on surfaces can explain the observed HONO peak, we compared measured HONO mixing ratios and HONO outputted by the RCAT 8.2 photolytic run (Figure 4.20c red line) and show that they are comparable in magnitude and that they follow similar trend, indicating that photolytic

conversion of NO_2 on ground surfaces was most likely the source of HONO during this time.

An alternate HONO formation mechanism that is proportional to [NO_2] x solar radiation is the daytime displacement of HONO by strong acids. VandenBoer et al., (2014) showed evidence of uptake of HONO on soil surface at night and subsequent HONO displacement from soil by deposition of strong acids, such as HNO_3 and HCl, during the day. They argue that HONO formed through the acid displacement mechanism are proportional to the product of solar radiation and NO_2 concentration as production of HNO_3 is proportional to the concentration of NO_2 and OH, the latter of which is proportional to solar radiation. For this mechanism to contribute significantly to the next daytime HONO surface flux, it requires a substantial deposition of HONO during the previous night. To determine whether this mechanism played an important role in UBWOS 2012, we calculated the total number of HONO molecules/cm^2 deposited during the night of 27 January (by multiplying the HONO uptake frequency and HONO concentration outputted by the lowest box of the 1-D model) and compared it to the total number of HONO molecules/cm^2 released by the daytime HONO surface flux. The integrated HONO molecules/cm^2 from 1900 of the previous night to 0700 hours was about $1.84x10^{14}$, which was slightly lower than the integrated daytime HONO molecules/cm^2 calculated from the HONO flux from 0700 hours to 1700 hours of $2.84x10^{14}$. This shows that displacement of HONO from soils by deposition of acids could account for a large portion of the observed HONO flux under moderate or low NO_2 conditions.

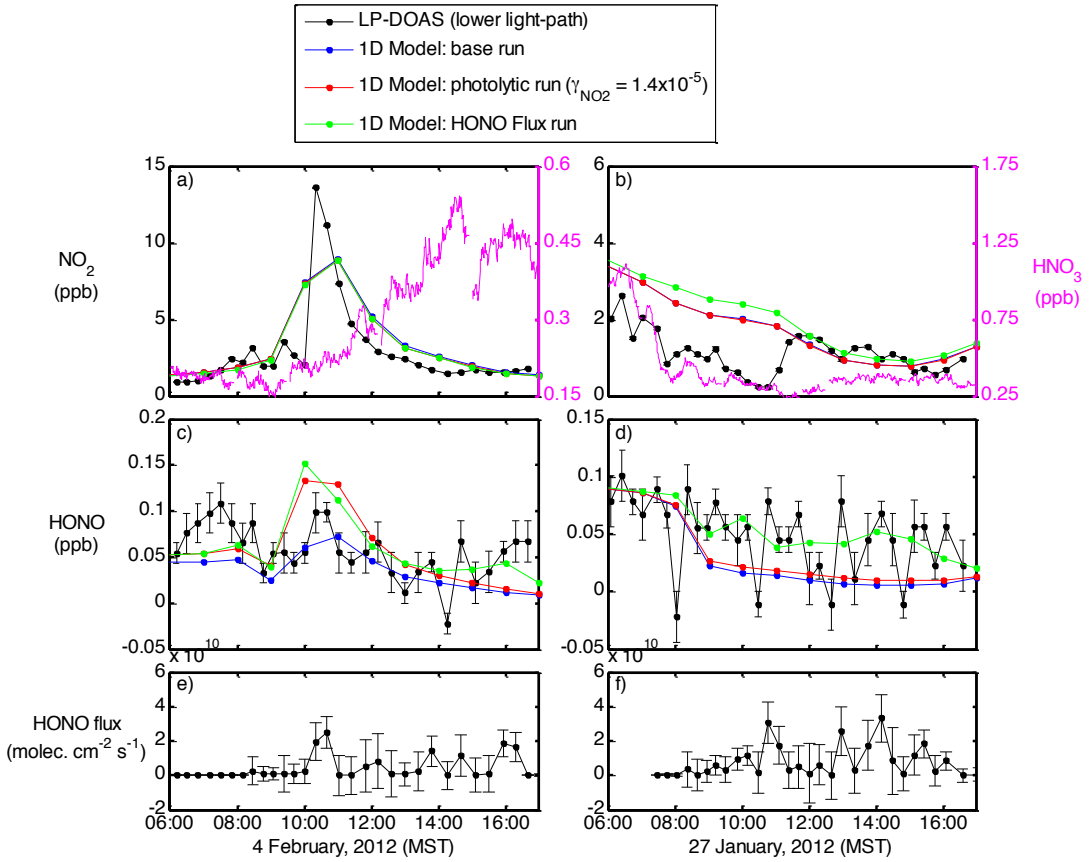

Figure 4.20 Modeled and measured NO_2, HONO, and HNO_3 mixing ratios. NO_2 mixing ratios are shown on the upper panels (a and b), HONO mixing ratios are shown on middle panels (c and d), and HONO fluxes are shown on lower panels (e and f). Left panels show analysis from 4 February 2012 (a, c, and e) and right panel shows analysis from 27 January 2012 (b, d, and f). LP-DOAS lower light path NO_2 and HONO mixing ratios and errors are shown in black, modeled NO_2 and HONO mixing ratios in the lower light path interval using RCAT 8.2 base run are shown in blue, HONO flux run results are shown in green, photolytic run results are shown in red (with NO_2 uptake coefficient of $1x10^{-6}$ for 4 February and $1.4x10^{-5}$ for 27 January). HNO_3 mixing ratios measured by NOAA are shown in magenta lines on the upper panels plots (a and b).

Model simulations for 27 January 2012, a day characterized by average wind speeds and relatively low NO_2 mixing ratios (about 2 ppb) are shown in Figure 4.20. The base run (blue) and photolytic run (red) underestimate measured HONO mixing ratios (black) suggesting that on days of moderate NO_2 levels, photolytic conversion of NO_2 does not seem to play an important role in HONO production. The strong correlation between HONO flux and [HNO_3] x UV solar radiation (Figure 7.18b) suggest that photolysis of surface HNO_3 might explain the observed HONO flux; furthermore, the average daytime HONO flux for 27 Jan (about $7.3x10^9$ molec. cm^{-2} s^{-1}) was close to the average HONO flux measured by Zhou et al., 2011 over a forest canopy ($6.2x10^9$ molec. cm^{-2} s^{-1}). However, without further information, such as concentration of surface adsorbed HNO_3, is not possible to determine whether this mechanism was an important source of missing HONO.

Another HONO formation mechanism that would give rise to positive surface HONO flux is HONO formation from soil nitrite (Sue et al., 2011). Sue et al., (2011) showed that gas-phase HONO released by soil depended strongly on the concentration of nitrite in soil and its pH. They proposed that biological nitrification and denitrification processes are the main sources of nitrite ions in the soil and showed that fertilized soils with low pH appeared to be particularly strong sources of HONO. We believe that emission of HONO from soil nitrite played a minor role in UBWOS 2012 as the soil was expected to be alkaline and cold during this field study. Due to lack of information about the pH and soil temperature in 2012, we inferred these properties from UBWOS 2014 measurements. We are confident that the soil in the UB in 2012 was alkaline as NOAA measured a pH of 8.06 for a soil sample collected in the UB in 2014 and a report by Utah

State University Extension stated that the pH of a large portion of soils in Utah ranged between 7.8 and 8.2. We are also certain that nitrite concentration produced by microbes was not significant during UBWOS 2012. Like most biological reactions, nitrification and denitrification processes are strongly influenced by soil temperatures, with these processes ceasing at soil temperatures below 5°C (Western Fertilizer Handbook, 2012). The hourly average soil temperatures at noon in 2014 was about -4°C (measured at 5 cm below the surface); therefore we can assume that soil temperatures in 2012 were not as cold as in 2014 but cold enough to render nitrite production from biological reactions negligible.

Comparison of the missing source of HONO and HONO surface flux rate (Figure 4.12) shows that HONO surface flux rate (magenta line) accounts for a significant portion of the $P_{unknown}$ (63±32%) throughout the day (from 0900 to 1500 hours). Furthermore, near noontime (from 1100 to 1300 hours), surface flux rate accounts for an average of 90±30% of the $P_{unknown}$, suggesting that photolytic surface sources of HONO, and not HONO formation pathways in the gas phase or on aerosols, were the dominant sources of the unknown HONO in 2012. Under high NO_x events, our HONO flux analysis favors HONO formation mechanisms that are related to solar radiation and NO_2 concentrations, such as photo-enhanced conversion of NO_2 and nighttime uptake of HONO followed by daytime acid displacement. Under moderate or low NO_2 level conditions, photolysis of HNO_3 seems to be the main HONO source. The $P_{unknown}$ peak at 0800 - 0900 hours is probably the result of rapid photolysis of HONO that accumulated in the nocturnal boundary layer and ineffective HONO production (through NO + OH) in the morning.

Preliminary measurements of low level of nitrophenols suggest that photolysis of nitrophenols was not an important source of HONO in UBWOS 2012.

4.6 Summary and conclusion

HONO light path averages were measured during the winter of 2012 in the Uintah Basin, Utah using the UCLA LP-DOAS. The measured light paths averages (2-31 m, 2-45 m, and 2-68 m agl) were used to retrieve HONO vertical profiles using a least square minimization approach. The HONO vertical profiles show higher mixing ratios near the ground than aloft suggesting that a ground surface HONO source was present during the study. HONO fluxes at 19 m agl were calculated using the retrieved vertical profiles and micrometeorological data from NOAA. Sunny day hourly average HONO fluxes show positive fluxes that follow solar radiation trend, with a maximum of 1.5×10^{10} molec. cm^{-2} s^{-1} occurring at noon. A similar value was measured above a forest canopy in Michigan. In this study, the HONO analysis was performed for sunny days, when the photolytic lifetime of HONO was about 13 minutes at noon and the steady state assumption can be applied. Comparison between measured HONO mixing ratios and calculated pseudo-steady state HONO concentrations points toward the presence of an unknown daytime source of HONO. Sunny days surface HONO fluxes correlate well with both [NO_2] x solar radiation ($R^2 = 0.58$) and [HNO_3] x solar radiation ($R^2 = 0.66$), making it difficult to determine which of the possible HONO sources pathways: photo-enhanced reduction of NO_2 on ground surface, HONO deposition at night followed by displacement by acids, or photolysis of surface HNO_3 contributes to the unknown daytime HONO source. A detailed analysis on a plume event that occurred on 4 February indicates that during

periods of high NO_2, photolytic NO_2 is the dominant source of HONO. More data is needed to determine whether photolysis of HNO_3 on surfaces, or other HONO sources, plays an important role in HONO daytime production. Finally, comparison between the unknown production rate of HONO ($P_{unknown}$) and HONO flux rate shows that a large portion of noontime $P_{unknown}$ (about 90%) can be accounted by the surface HONO flux rate suggesting that the HONO sources at noon and around noontime come from the surface and are photolytic.

Chapter 5 HONO STUDY DURING UBWOS 2014

5.1 Introduction

Three consecutive winter studies took place at the Horse Pool site from 2012 to 2014 (UBWOS 2012, UBWOS 2013, and UBWOS 2014). Chapter 4 covers the HONO analysis from UBWOS 2012 and this chapter describes the result from UBWOS 2014. Even though we did not participate in the UBWOS 2013 study, its results, especially regarding HONO, are relevant to our HONO study.

In contrast to UBWOS 2012, snow cover during UBWOS 2013 was abundant and 8-hour-average O_3 concentrations reached up to 142 ppb (Stoeckenius and McNally, 2014). By comparing the results of these two studies, researchers concluded that the development of winter O_3 episodes requires snow cover, calm weather conditions, and emissions of ozone precursors near the ground. Snow cover enhanced ozone production by increasing the total UV flux (about 50% during the winter of 2013) driving photochemical reactions that lead to ozone formation. Snow cover also stabilized the

lower boundary layer promoting strong inversion layers that trapped ozone and its precursors in a low layer above the surface.

A critical result from the UBWOS 2013 study was the measurement of very high HONO levels during the day (measurements were made by NOAA's Acids NI-PT-CIMS). The average daytime HONO mixing ratio in 2013 was 0.55 ± 0.58 ppb (Figure 5.1 left panel), significantly larger than mixing ratios measured in 2012 (0.05 ± 0.04 ppb; Figure 5.1 left panel). The HONO mixing ratios in 2013 peaked around solar noon suggesting a photochemical source (Figure 5.1 middle panel). The diurnal variations of HONO in 2013 show higher levels of HONO during the day than during the night, in contrast to 2012, when HONO levels were higher during the night than day, the later being the type of diurnal profile typically found in polluted urban areas (Figure 5.1 right panel).

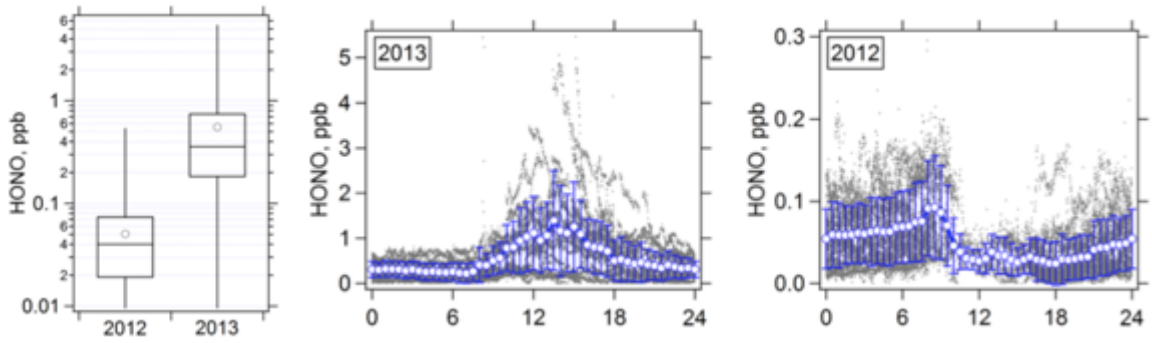

Figure 5.1 Left panel shows comparison of the concentration of HONO measured in 2012 and 2013 at Horse Pool site. Middle and right panels show diurnal variations of HONO in 2012 (middle panel) and 2013 (right panel) at Horse Pool site. Adapted from Stoeckenius and McNally (2014).

Further analysis and results from wintertime O_3 models raised questions about the accuracy and representativeness of the 2013 HONO measurements. Tests made in the laboratory after the end of the field study, show that the presence of HO_2NO_2 in the inlet could produce a positive interference in the detection of HONO, indicating that a fraction of the observed daytime HONO might have been from HO_2NO_2. Furthermore, O_3 models in the Upper Green River Basin Wyoming (Carter and Seinfeld, 2012), and for UBWOS 2013 (Edwards et al., 2014) show that when these high daytime HONO levels are included, the models substantially over predict O_3 levels. These results indicate that the role of HONO in promoting ozone formation during winter episodes was still uncertain and that additional measurements were needed to address this issue.

One of the main objectives of the winter 2014 study was to resolve the uncertainties about the magnitude and temporal pattern of HONO and the role of HONO in winter ozone formation. Five instruments, four in-situ instruments and one remote sensing system, were deployed to measure HONO at the Horse Pool site during UBWOS 2014: ACES (Airborne Cavity Enhanced Spectroscopy), iCIMS (iodide ion Chemical Ionization Mass Spectrometry), LOPAP (Long Path Absorption Photometer), Acid CIMS (Acid Chemical Ionization Mass Spectrometry), and LP DOAS (Long Path Differential Optical Absorption Spectroscopy). Description of these instruments can be found in Chapter 2. Supporting meteorological and chemical measurements were also included in the UBWOS 2014 study. The details and results of these measurements are described in the subsequent sections of this thesis.

The 2014 Horse Pool site consisted of a sampling tower and four trailers with three of them clustered around the sampling tower. The tower and instrument enclosures

were similar to the ones used in 2012 (Figure 5.2, photo on the left). For convenience, the UCLA LP DOAS instrument was housed inside a trailer instead of a tent in 2014 (Figure 5.2, photo in the right). The trailer was set up about 18 m northwest of the location of the 2012 tent. The UBWOS 2014 measurement period started at the beginning of January and ended in mid February 2014.

Figure 5.2 Left photo shows Horse Pool site during UBWOS 2014 looking from North to South (left panel). Right photo shows the trailer that housed the UCLA LP-DOAS in 2014.

5.2 Ancillary measurements

The instruments and their arrangements were very similar to those used in UBWOS 2012. Meteorological data, which include temperature, relative humidity, and wind speed, were measured the same way as in 2012. A summary of all the measurements made during UBWOS 2014 can be found in the work of Stoeckenius (2015).

5.3 Results

5.3.1 Meteorology during UBWOS 2014

In contrast to UBWOS 2012, when snow cover was almost absent, weather conditions during UBWOS 2014 were more characteristic of wintertime, with snow-covered ground and a shallow cold-pool layer. A large weather event led to significant snow formation in early December in the UB but little additional snow fell for the rest of the winter (Stoeckenius, 2015). As winter advanced, snow gradually melted reducing surface reflectivity (Figure 5.3 green line); by the end of the field study, no snow remained (Figure 5.3 blue line).

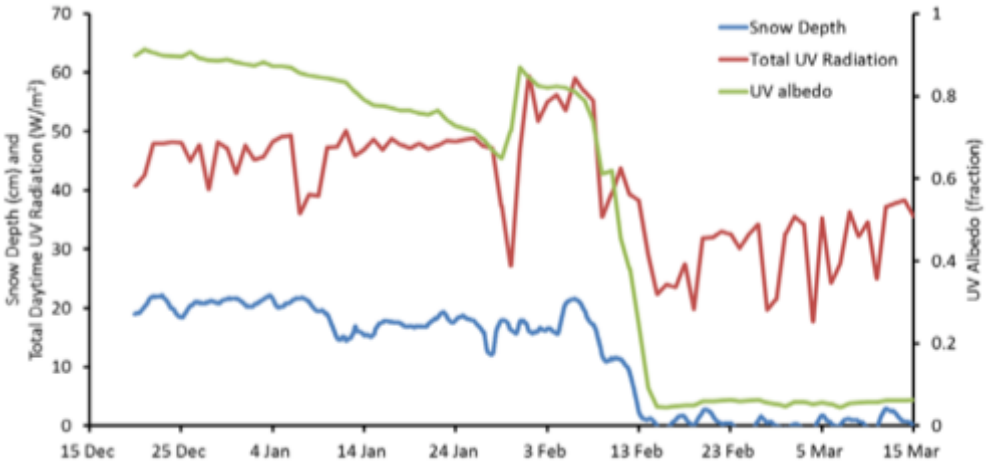

Figure 5.3 Time series of snow depth (blue line), total UV radiation (sum of upwelling and downwelling UV-A and UV-B) radiation (red line), and average UB-A and UV-B albedo (green line) during winter 2013-2014 at Horse Pool site. Adapted from Stoeckenius (2015).

Temperatures at the Horse Pool site ranged between 257 K and 283 K with hourly average temperatures ranging from 266 K in the early morning to 273 K in the mid afternoon (Figure 5.4a red line) throughout the study. On the other hand, temperatures during UBWOS 2014 were on average 3.6 K lower than temperatures measured during

UBWOS 2012 (Figure 5.4a black line). RH during UBWOS 2014 was on average 20% higher than those measured during 2012 (Figure 5.4c red line) and fluctuated between 34% and 100% with hourly average RH ranging between 86% in the early morning and 64% around early afternoon. UBWOS 2014 was dominated by weak-wind periods with average wind speeds of about 2 m s^{-1} throughout the study; 2014 wind speeds were slightly lower than those measured in 2012 (Figure 5.4b black line), ranging from below the detection limit to 11 m s^{-1} (Figure 5.4b red line).

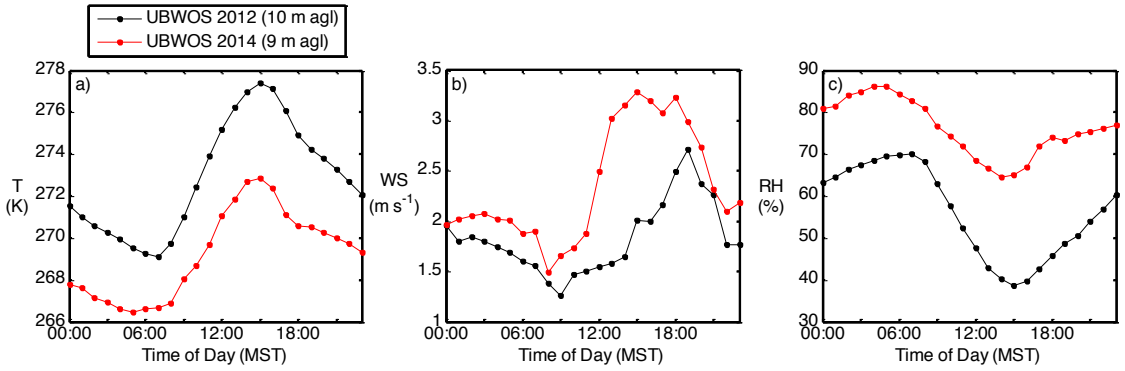

Figure 5.4 Hourly average meteorological data measured during UBWOS 2014 at 10 m agl (shown in red) and UBWOS 2012 measured at 9 m agl (shown in black). (a) shows temperature (K), (b) shows wind speed (m s^{-1}), and (c) shows relative humidity.

5.3.2 NO_2, O_3, and HONO light path average mixing ratios

NO_2, O_3, and HONO were measured continuously on all three light paths from 22 January to 15 February 2014 except for time periods when the instrument was

misaligned, the light source had to be changed, or the visibility was low due to fog.

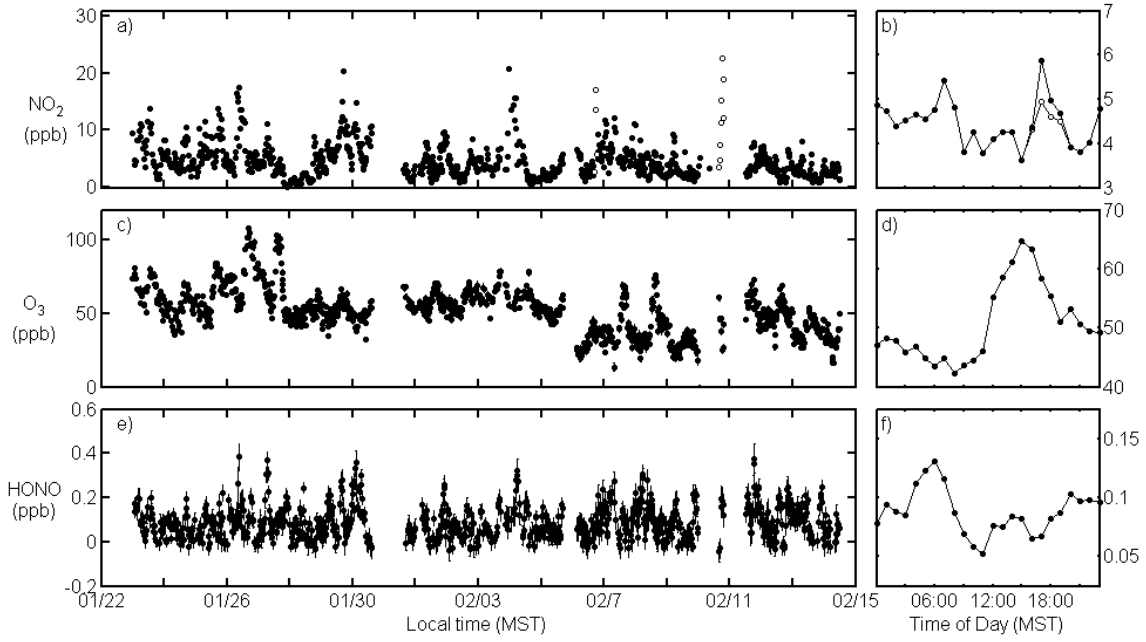

Figure 5.5 LP-DOAS lower light path time series of (a) NO_2, (c) O_3, and upper light path time series of (e) HONO measured during UBWOS 2014. Hourly average mixing ratios of (b) NO_2, (d) O_3, and (f) HONO measured during UBWOS 2014 on the lowest light path (NO_2 and O_3) and upper light path (HONO). Empty circles in plot (a) represent the NO_2 mixing ratios that correlate with SO_2 peaks measured on the lower light path. Empty circles in plot (b) show the hourly average NO_2 mixing ratios calculated without the NO_2 mixing ratios that correlated with SO_2.

NO_2 mixing ratios measured on the lowest light path (2 – 27 m agl) ranged from 0.092 ± 0.12 ppb to 22.7 ± 0.2 ppb throughout the field study (Figure 5.5a) with hourly average NO_2 mixing ratios varying between 3.6 ppb (at 1500 hours) and 5.9 ppb (at 1700 hours) (Figure 5.5b). The hourly average NO_2 peak observed at 1700 was significantly

influenced by two NO_2 peaks (shown in Figure 5.5b in open circles) that correlated with SO_2 mixing ratios measured on the lowest light path (Figure 5.6a). The tight correlation between NO_2 and SO_2 suggest that the NO_2 peaks were the result of plumes, most probably from the Bonanza power plant, crossing through the main site. The exclusion of these NO_2 peaks reduced the hourly average mixing ratios of NO_2 at 1700 hours from 5.9 ppb to 5 ppb. The lowest levels of NO_2 during the field project occurred in the evening of 27 January (Figure 5.6a and Figure 5.7a) and late afternoon of 4 February (Figure 5.6a and Figure 5.7b), when two high wind episodes took place (Figure 5.6d). Figure 5.7a shows that on 27 January at about 1900 hours, NO_2 mixing ratios fell from 3.8 ± 0.1 to 0.21 ± 0.09 ppb within an hour. Coincidently, wind speed increased from 1.25 m s^{-1} up to 11.2 m s^{-1} and wind direction changed from about 100 degrees to 10 degrees within the same time frame (Figure 5.7e-g). A similar trend was observed on 4 February at about 1400 hours when NO_2 mixing ratios dropped from 2.16 ± 0.09 to 0.48 ± 0.09 ppb while wind speed increased from 0.92 m s^{-1} to 8.1 m s^{-1} and wind direction changed from about 300 to about 35 degrees (Figure 5.7b-d-f-g) These measurements indicate that during these two time periods, strong winds flushed NO_2 and other pollutants out of Horse Pool site and its surroundings.

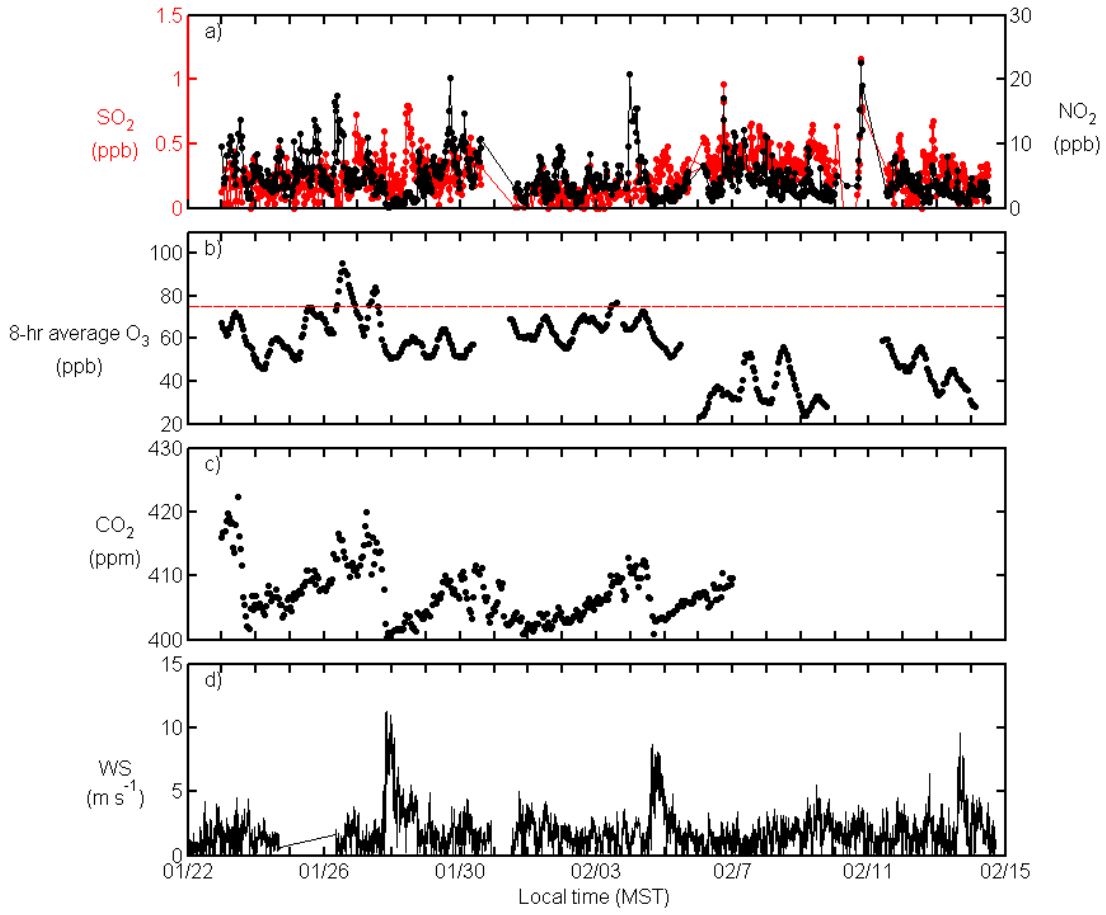

Figure 5.6 Time series of SO_2, NO_2, 8-hr average O_3, CO_2, and wind speed measured at the Horse Pool site. (a) LP-DOAS lower light path SO_2 mixing ratios in red and NO_2 mixing ratios in black. (b) LP-DOAS lower light path 8-hr average O_3 mixing in black. Red line represents the NAAQS O_3 standard (75 ppb) of winter of 2014. (c) CO_2 mixing ratios measured by NOAA. (d) Wind speed measured at 9 m agl.

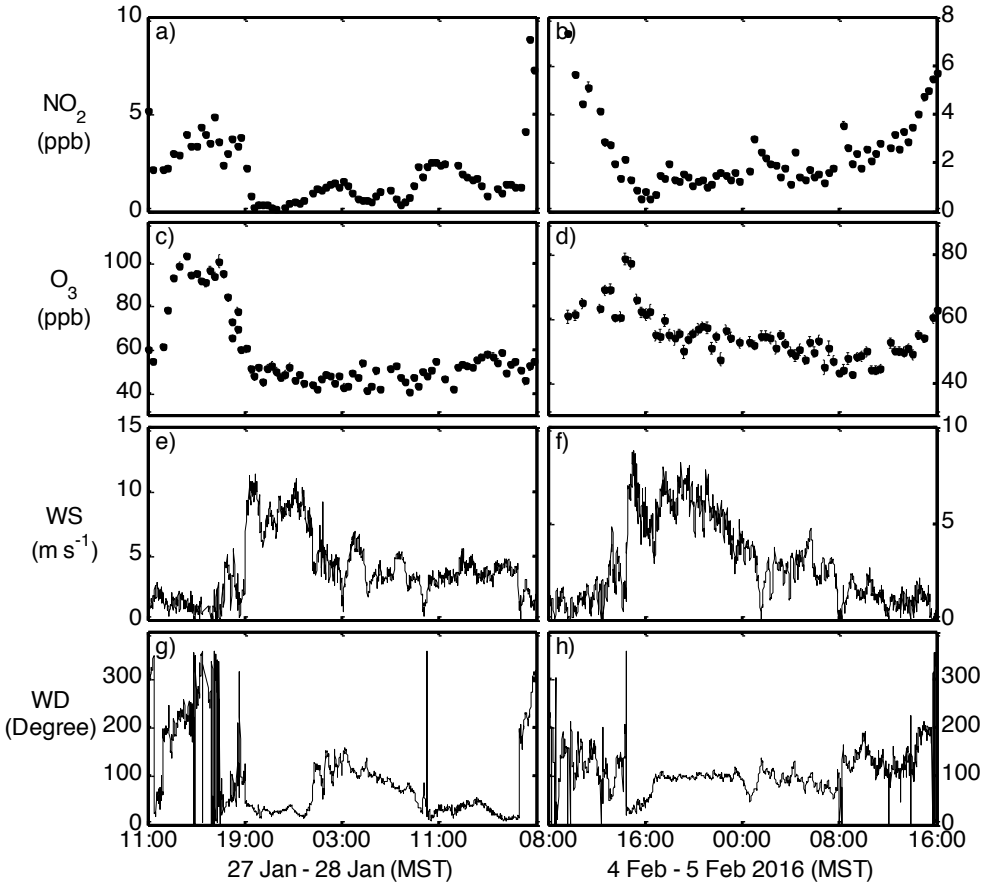

Figure 5.7 NO_2 (a and b), O_3 (c and d), wind speed (e and f), and wind directions (g and h) measured at the Horse Pool site on 27 January 2014 (left panels) and 4 February 2014 (right panels).

Figure 5.8 compares the lower light path average mixing ratios (Figure 5.8, left panel plots) and diurnal profile (Figure 5.8, right panel plots) of NO_2, O_3, and HONO measured in 2012 (in red) and 2014 (in black). NO_2 levels were comparable between these two years, with diurnal averages of 4.5 ppb for both data sets (Figure 5.8a and 5.8b). Figure 5.8b shows that between midnight and noontime, 2012 NO_2 was up to 1.8 ppb larger than 2014 NO_2 levels and between noontime and late evening, 2012 NO_2 was

up to 3 ppb lower than 2014 NO_2. NO_x mixing ratios measured by NOAA show similar NO_x levels in the 2012, 2013, and 2014 studies, with daytime NO_x slightly higher in 2014 than the other two years (Figure 5.9).

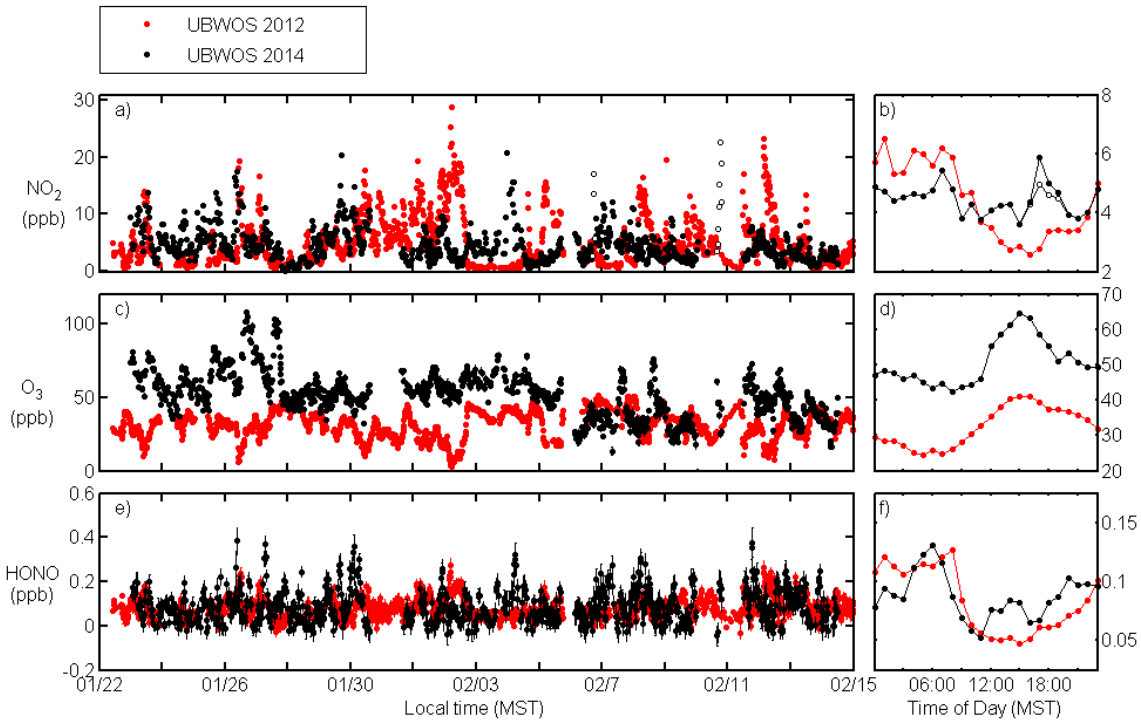

Figure 5.8 LP-DOAS lower light path time series of (a) NO_2, (c) O_3, and (e) HONO measured during UBWOS 2012 (black) and UBWOS 2014 (red). Hourly average mixing ratios of (b) NO_2, (d) O_3, and (f) HONO measured during UBWOS 2012 and 2014 on the lowest light path. Empty circles (a) represent NO_2 mixing ratios that correlate with SO_2 mixing ratios measured by LP-DOAS on the lower light path. Empty circles in plot (b) show the hourly average NO_2 mixing ratios calculated without the empty circles shown in plot (a).

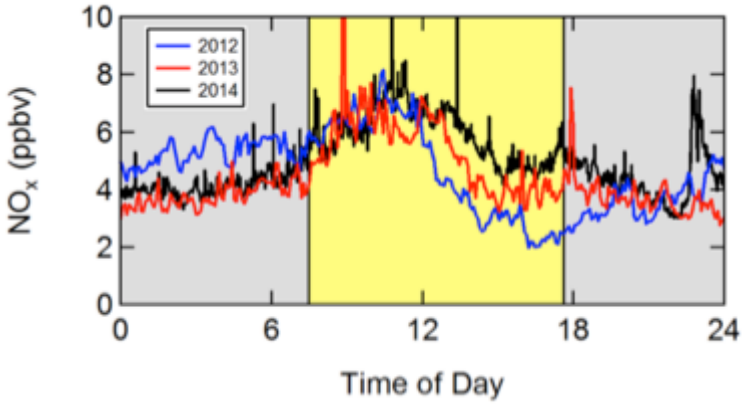

Figure 5.9 Average NO_x mixing ratios measured at the Horse Pool site versus time of day for the three UBWOS intensive studies. Adapted from Stoeckenius (2015).

O_3 mixing ratios measured on the lowest light path ranged between 13 ± 3 ppb and 108 ± 2 ppb throughout the study (Figure 5.5c) with hourly average mixing ratios varying from 46 ppb at 0800 hours to 67 ppb at 1500 hours on the lower light path (Figure 5.5d). Comparison of UBWOS 2012 and UBWOS 2014 measurements show higher O_3 levels during 2014, especially in the first two-thirds of the study (Figure 5.8b). On average, hourly average O_3 mixing ratios were 18 ppb higher in 2014 than in 2012 (Figure 5.8d). The elevated O_3 levels were mainly attributed to snow cover, an element that was almost absent during 2012. 8-hr average O_3 mixing ratios calculated from the lower light path observations show three days on which O_3 exceeded the NAAQS (NAAQS during UBWOS 2014 was 75 ppb), two of the days were in late January (26-27 January) and one in early February (3 February) (Figure 5.6b). Measurements show a steady daily increase of O_3 and CO_2 starting on 24 January, two days prior to the 26-27 January high O_3 episodes (Figure 5.6b and Figure 5.6c). These measurements suggest that O_3, CO_2, and other trace gases accumulated in the basin as a result of strong inversions

that persisted during these periods. Weak winds (< 4 m s^{-1}) were observed from 24 January to 27 January. On 27 January, winds speeds increased significantly removing O_3, NO_2, and CO_2 (Figure 5.6a, Figure 5.6b, and Figure 5.6c) from the basin. Measurements of O_3, CO_2, and wind speed show similar trends for the 4 February O_3 episode.

The retrieval of UBWOS 2014 HONO data resulted in significantly more negative data (or outliers) (about 10%) than in previous years. Most of the outliers were found near noontime in the lower and middle light paths. Outliers were probably caused by turbulence, which reduced the light intensity detected by the instrument. The detection limits for HONO during 2014 were almost twice that of 2012 and the data set had more measurement gaps. Figure 5.10 shows the time series of HONO measured in the lower, middle, and upper light paths. The white circles show the positive data and negative data within 2 σ error of the respective measurement. Filled circles show the negative data that are smaller than the negative 2 σ error, which were interpreted here as outliers. The red line is the zero line. The plots on the right panel show hourly average mixing ratios of HONO in each respective light path. Two sets of hourly average HONO mixing ratios were calculated: in the first set, negative HONO smaller than 2 σ error (or outliers) were removed from the data before calculating the hourly averages (Figure 5.10b-d-f in black line and markers); in the second data set, the outliers were replaced with zero before the HONO hourly averages were calculated (Figure 5.10b-d-f in red line and markers). The hourly average HONO calculated from the second data set is essentially the lower bound of our measured HONO data. I will be using the hourly average HONO mixing ratios calculated from the first data set throughout this study.

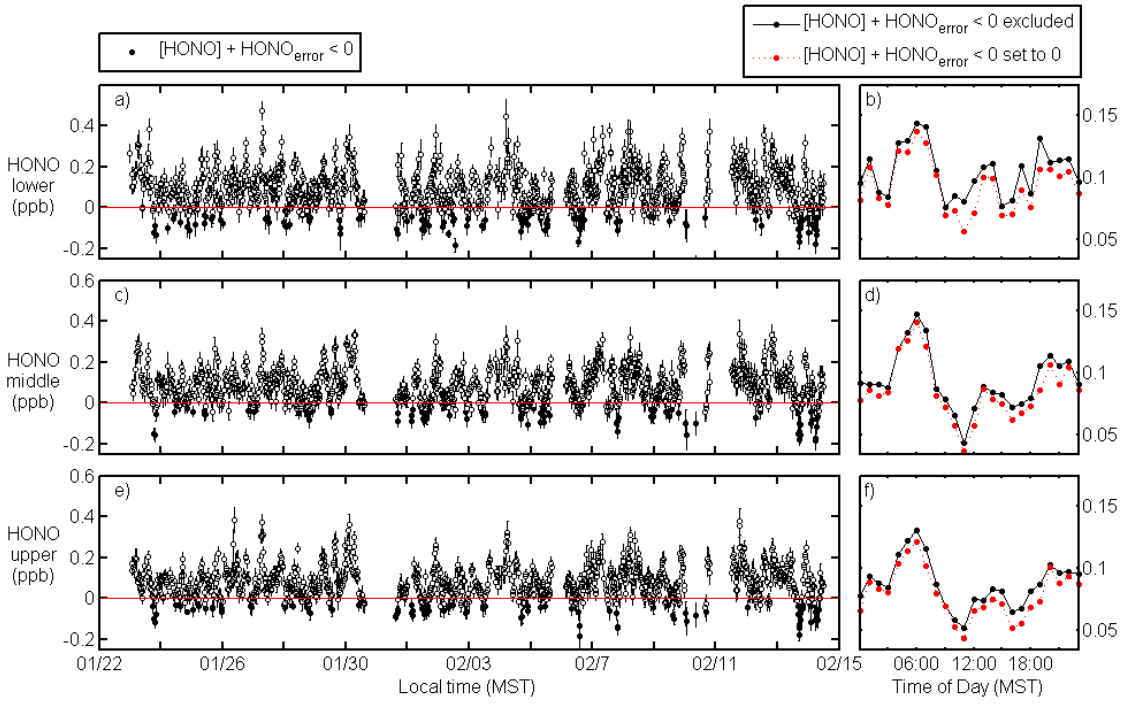

Figure 5.10 Time series of LP-DOAS measurements of HONO on the (a) lower light path, (c) middle light path, and (e) upper light path. Filled circles represent outliers, open circles represent positive HONO and negative data within the 2σ error of the respective measurement. The red line shows zero. Hourly average HONO mixing ratios calculated from (b) lower, (d) middle, and (f) upper light paths data sets in which outliers were removed (black markers and line) or outliers were substituted by zero (red markers and line).

HONO mixing ratios measured in the lower, middle, and upper light paths ranged from below the detection limits to 0.47 ± 0.04, 0.34 ± 0.06, and 0.38 ± 0.06 ppb, respectively throughout the study (Figure 5.10a, Figure 5.10c, and Figure 5.10e). Hourly average HONO mixing ratios varied between 77 ppt at 0900 to 144 ppt at 0600 hours on the lower light path (Figure 5.10b), 44 ppt at 1100 to 148 ppt at 0600 hours on the middle

light path (Figure 5.10d), and 52 ppt at 1100 to 131 ppt at 0600 on the upper light path (Figure 5.10f) throughout the study. Even though comparison of UBWOS 2012 and UBWOS 2014 data show that daytime HONO mixing ratios measured in 2014 were higher (up to about 60 ppt) than daytime HONO levels in 2012, they are still significantly lower than HONO levels (550 ± 580 ppt) measured in 2013.

5.3.3 HONO measurement comparison

One of the main objectives of the UBWOS 2014 study was to determine the validity of high daytime HONO levels measured recently over snow surfaces impacted by oil and gas activities (Rappengluck et al., 2014; Stoeckenius and McNally, 2014). Four in-situ instruments and the UCLA LP-DOAS were deployed to measure HONO during UBWOS 2014. The in-situ instruments were placed in a small container mid-way of the measuring tower (Figure 5.11) at about 9.1 m agl and the LP-DOAS was set up in a container northeast of the tower (Figure 5.11). Table 5.1 shows the time resolution and detection limits of the HONO measurements of each instrument.

Figure 5.11 The Horse Pool HONO measurement site as configured during the 2014 intensive study. Adapted from Stoeckenius (2015).

Table 5.1 Summary of the HONO measurements during UBWOS 2014.

Instrument	**Principle of Operation**	**Time Resolution**	**Detection Limit (pptv)**
ACES	Broad-band Cavity Enhanced Spectroscopy	1 min	200
ACIMS	Acetate ion NI-PT-CIMS	1 – 10 sec	10
ICIMS	Iodide Ion Chemical Ionization Mass Spectrometry	1-5 sec	5
LOPAP	Chemical Derivatization UV-Absorption	3 min	10
LP DOAS	Long-Path Differential Optical Absorption Spectroscopy	24 min (for each vertical profile)	75 (average) 28 (best)

Figure 5.12 shows the time series of HONO measurements corresponding to a period of about 5 days during which all in-situ instrument inlets were placed at the same height (9.1 m agl). As stated in Stoeckenius and McNally (2014), the time series shows great variability among the HONO measurements, with the DOAS HONO mixing ratios generally being lower than the in-situ measurements (Figure 5.12). Comparison of results by correlation with DOAS (Figure 5.13) also shows that DOAS HONO levels were generally lower. A possible explanations for the discrepancy between the DOAS and in-situ measurements is the different measurement set up, i.e., the DOAS data were spatially (measured on light paths of about 5 km) and temporary (time resolution was about 8 minute) averaged. Also, interferences in the in-situ measurements can explain some of the high HONO values in the in-situ data. LOPAP measurements made at a cold polar environment (Legrand et al., 2014) show an overestimation of HONO due to PNA (HO_2NO_2). Their lab experiments estimated an increase of HONO by ~ 15pptv in the presence of 100 pptv of PNA.

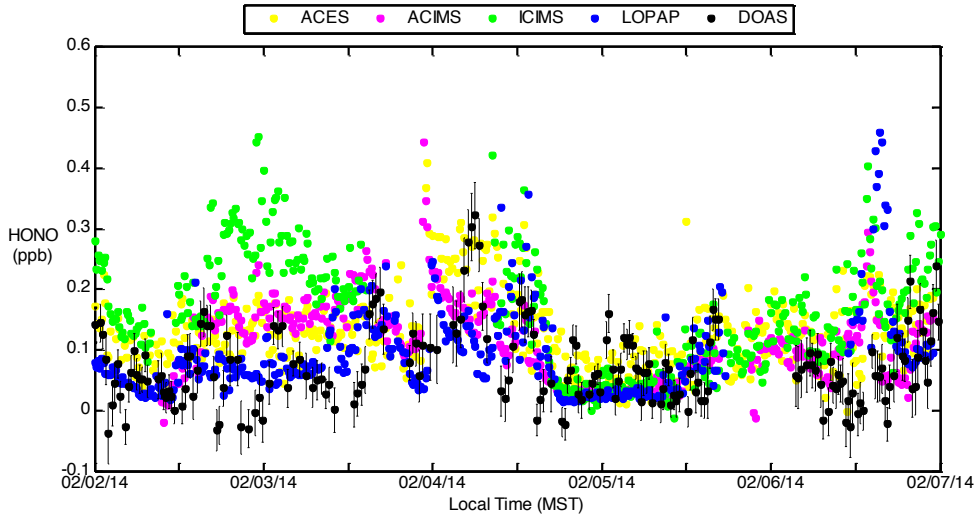

Figure 5.12 Comparison of the four in situ and DOAS upper light path HONO measurements in the 'common period'.

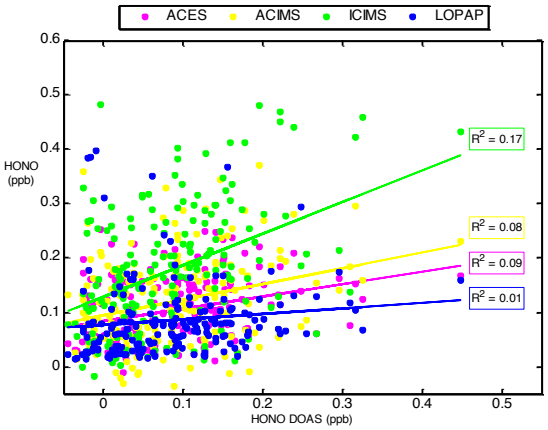

Figure 5.13 Correlation of the four in situ with DOAS lower light path HONO measurements in the 'common period'.

NOAA scientists tested PNA interferences on HONO using iCIMS measurements. The test consisted of detecting PNA and HONO by alternating between a short inlet (3 m, set at room temperature) and a long inlet (20 m, set at 30°C) for two days

(Figure 5.14). While high levels of HONO and low levels of PNA were detected through the long warm inlet, low levels of HONO and high levels of PNA were measured in the short inlet suggesting that inlet effects can result in PNA being detected as HONO. NOAA measurements show that the average PNA concentration reached a maximum of 120 ppt around 1400 hours.

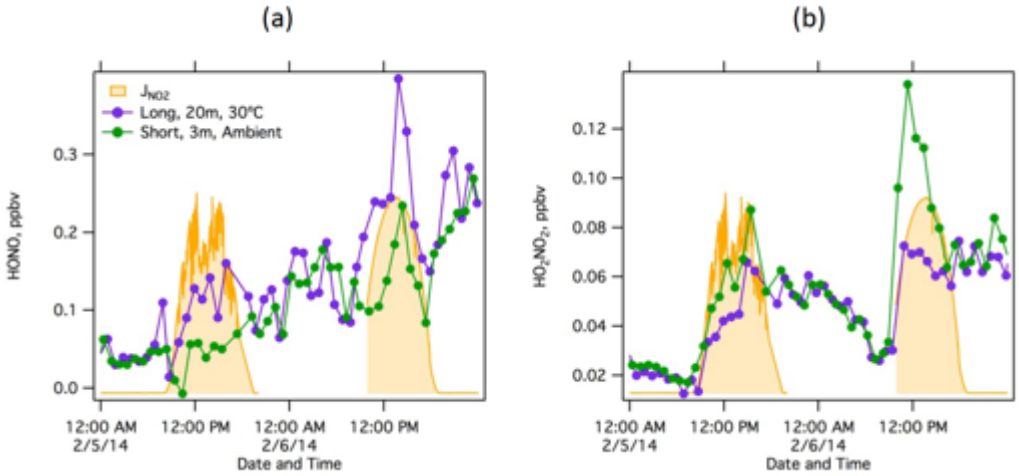

Figure 5.14 Timelines of the short and long inlets tests performed with the iCIMS for (a) HONO and (b) HO_2NO_2. Adapted from Stoeckenius (2015).

Acid CIMS HONO measurements from UBWOS 2014 also suggest a direct HONO interference due to PNA. The weak bonds of HO_2-NO_2 and O_2-NO_2 can lead to the formation of NO_2^-, which results in interferences in the Acid CIMS measurements (Stoeckenius, 2015). Under the assumption that the good correlation between Acid CIMS HONO and iCIMS PNA (Figure 5.15) is a measurement of PNA interference in the inlet and a detection of 1:1 of PNA as HONO occurs, then Acid CIMS HONO measurements become comparable to the DOAS measurements (Figure 5.16) (Personal communication

with Roberts and Veres). However, the true extent of the PNA interference on Acid CIMS measurements still needs to be quantified.

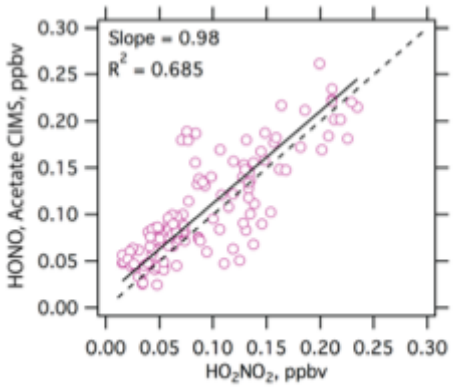

Figure 5.15 Correlation plot between daytime ACIMS HONO and iCIMS PNA in UBWOS 2014. Adapted from Stoeckenius (2015).

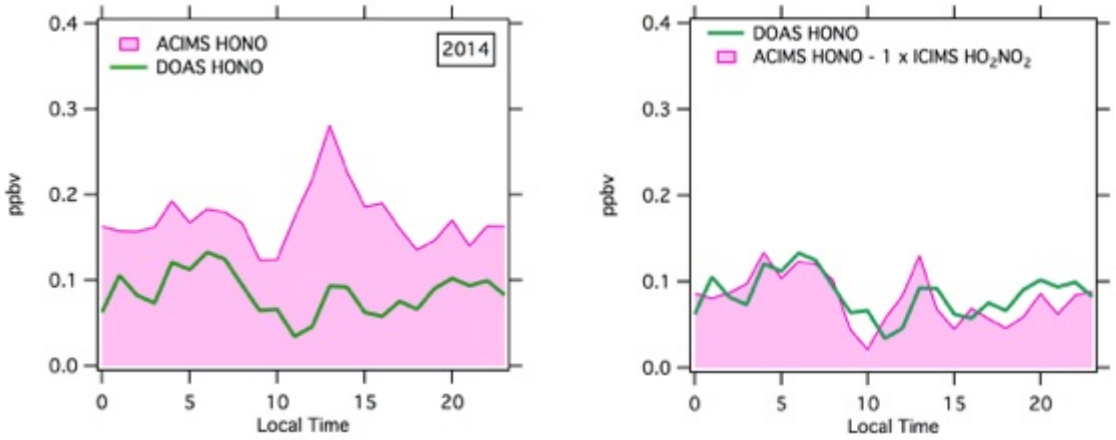

Figure 5.16. Left panel shows the diurnal profile of ACIMS HONO (pink) and DOAS HONO (green). Right panel shows the diurnal profile of ACIMS HONO minus PNA (assuming 1:1 PNA to HONO conversion) in pink, compared to DOAS HONO (green). Adapted from P. Veres, personal communication, 26 November 2014.

LOPAP measurements observed during UBWOS 2014 were also suspected of suffering from PNA interferences, as comparison of average diurnal profile of LOPAP

with iCIMS PNA shows a similar temporal trend (Figure 5.17 left panel; Stoeckenius, 2015). Under the assumption that PNA is detected as HONO (with a 1:1 ratio), then LOPAP HONO measurements also become comparable to the DOAS HONO measurements (Figure 5.17 right panel) (Personal communication with Roberts and Veres). However, further laboratory experiments are needed to verify this.

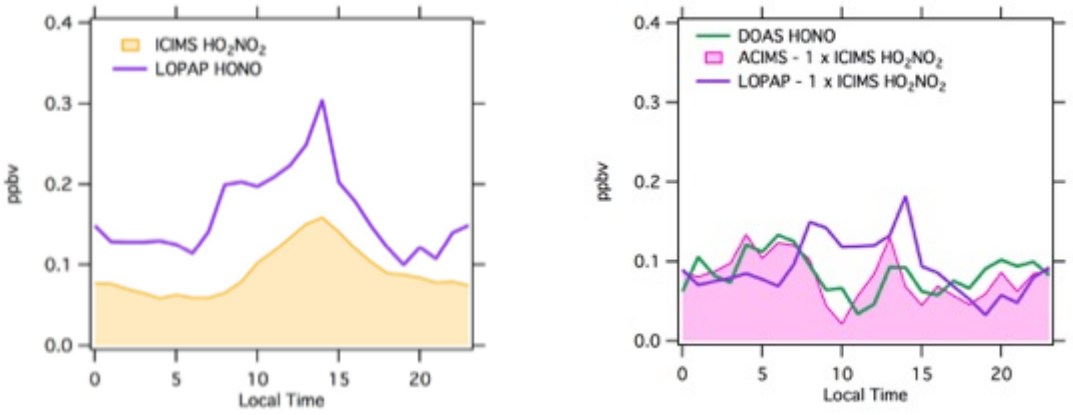

Figure 5.17 Left panel shows average diurnal profiles of HONO observed by the LOPAP (in purple), and PNA observed by the iCIMS (yellow). Right panel shows diurnal profile of corrected ACIMS HONO, corrected LOPAP HONO, and DOAS HONO (green). The corrected ACIMS and LOPAP HONO were determined by subtracting PNA to HONO concentrations. Adapted from P. Veres, personal communication, 26 November 2014.

The LP-DOAS was the reference instrument for HONO measurements during UBWOS 2014 because it was not sensitive to PAN or other chemical interferences as it measures in the open atmosphere.

5.3.4 NO_2, O_3, and HONO mixing ratios light path gradients

The 2012 and 2014 diurnal profiles of O_3, NO_2, and HONO, on each light path, are shown in Figure 5.18. On the one hand, lower mixing ratios of NO_2 (Figure 5.18a) and O_3 (Figure 5.18c) were measured on the lower light path during the night and no vertical gradients was observed during the day in 2012. On the other hand, 2014 observations show higher mixing ratios of NO_2 (Figure 5.18b) and O_3 (Figure 5.18d) on the lower light path both during the day and night. The negative gradients observed in 2014 were the result of a more stable surface layer, due to the presence of snow cover in 2014, which slowed vertical transport accumulating O_3 and O_3 precursors near the ground surface.

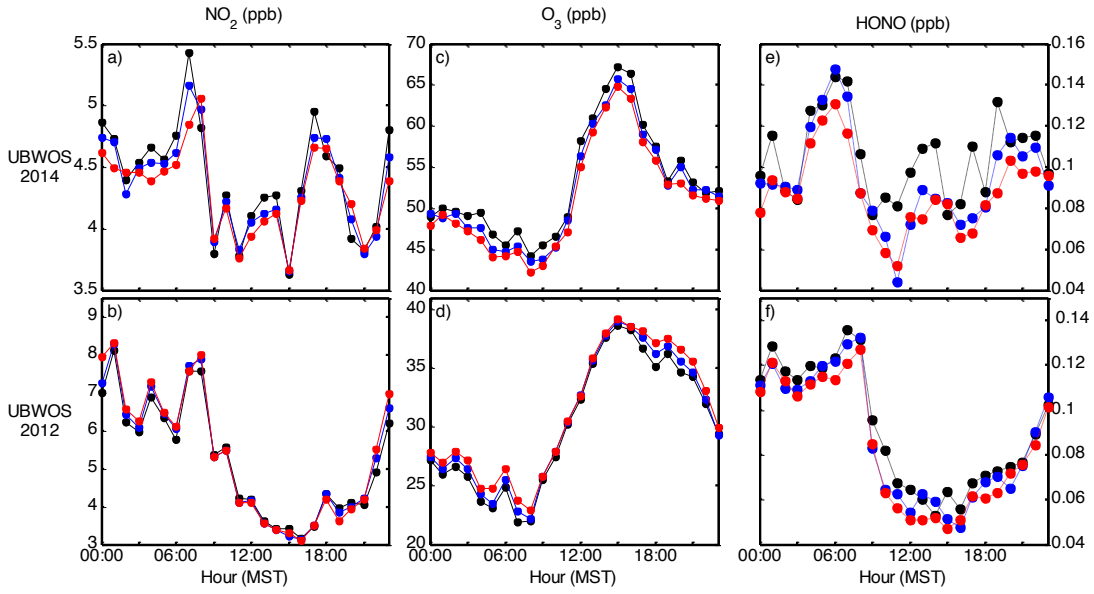

Figure 5.18 Hourly average light path average mixing ratios of (a) O_3, (b) NO_2, and (c) HONO in the lower (black), middle (blue), and upper (red) light paths throughout the study.

The 2012 and 2014 HONO diurnal profiles follow a similar temporal trend from midnight to noontime. After noontime, 2012 HONO mixing ratios stay relatively low during the day (below 70 ppt on all three light paths) (Figure 5.18e), while 2014 HONO significantly increases (above 100 ppt on the lower light path) between 1100 and 1600 hours (Figure 5.18c).

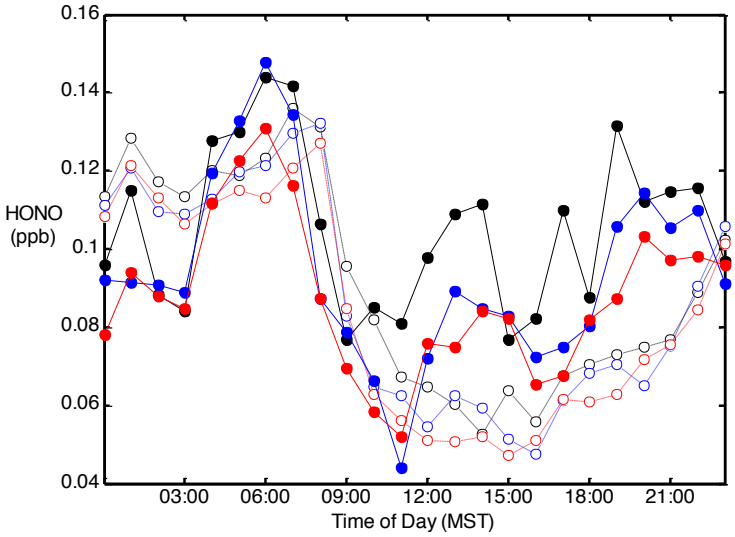

Figure 5.19 Hourly average light path averages mixing ratios of HONO in the lower (black), middle (blue), and upper (red) light paths measured in 2012 (empty circles) and 2014 (filled circles).

The 2012 and 2014 diurnal profiles (Figure 5.19) also show that HONO mixing ratios on the lower light path were higher than those measured in the middle and upper light paths. The HONO gradients were larger in 2014 than 2012; with the maximum difference between the upper and lower light path hourly average HONO mixing ratios of 14 ppt (at 1300 hours) in 2012 and 34 ppt (at 1200 hours) in 2014. The 2014 negative HONO gradient indicates that there is a daytime ground source of HONO in the UB.

5.3.5 HONO vertical profiles

HONO vertical profiles were retrieved using the least square minimization method described in section 3.1. The retrieved vertical profiles of HONO for sunny days were averaged hourly (from 0900 to 1500 hours) and plotted in Figure 5.20. HONO vertical profiles show higher HONO mixing ratios near the surface than aloft and a rapid decay of HONO mixing ratios above 30 m agl.

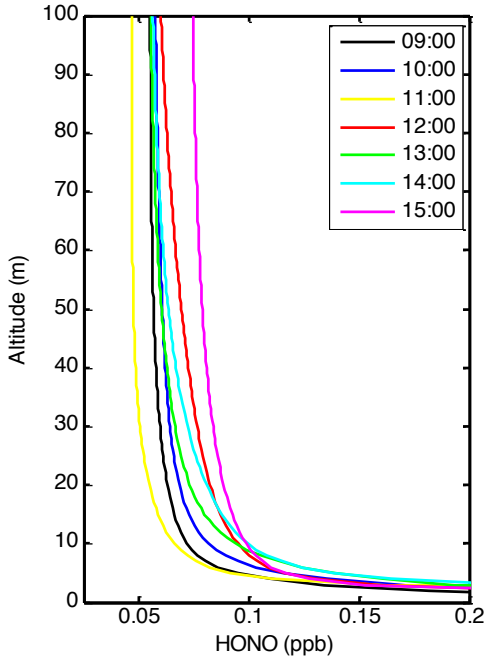

Figure 5.20 Sunny days hourly average retrieved vertical profiles of HONO using least square fitting methodology (section 3.1).

The 2014 HONO analysis, similar to the 2012 HONO study, was based on data collected on sunny days (27 January, 4 February, 6 February, 7 February, and 18 February). The average photolytic lifetime of HONO on these days was about 7 minutes at noon; allowing us to apply the steady state assumption on these days. As in 2012, the

lifetimes of HONO on sunny days increased significantly before 0900 (from about 33 minutes to about 11 minutes between 0800 and 0900 hours) and after 1500 (from about 12 minutes to 30 minutes from 1500 to 1600 hours). The sunny days photolytic lifetime of HONO in 2014 was almost half of that in 2012 (13 minutes) due mainly to the snow enhanced HONO photolysis rates in 2014.

5.3.6 HONO fluxes

HONO fluxes were calculated using the gradient method described in section 3.2. Eddy diffusivity coefficients (K) and HONO gradients were calculated at 19 m agl using friction velocities (u^*) and Monin Obhukov lengths (L) observed by NOAA. Comparison of 2012 and 2014 hourly average u^* and L shows lower daytime u^* (average daytime of 0.083 m s^{-1}) and L (-average daytime of -2.64 m) in 2014. This agrees with the stronger stability encountered in 2014.

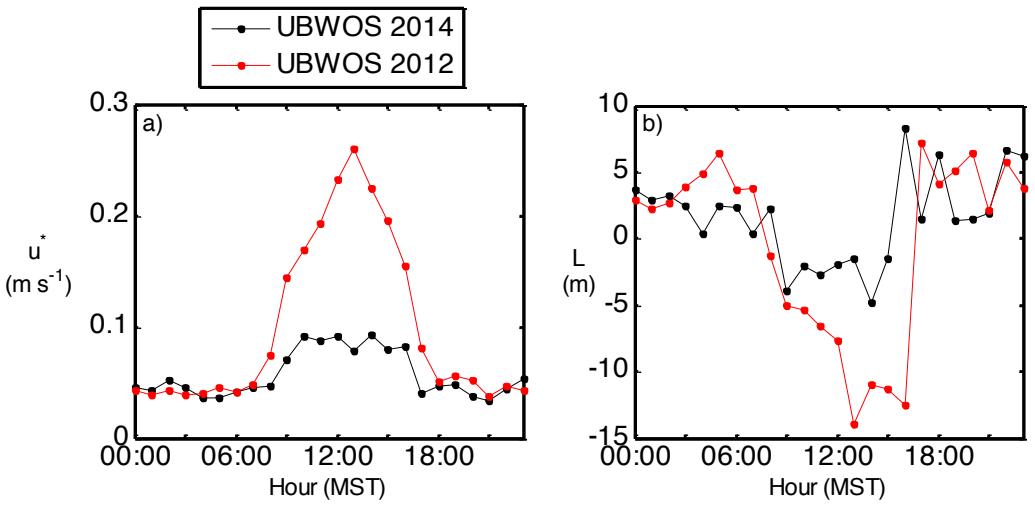

Figure 5.21 Hourly median micrometeorological data measured at 16 m agl: (a) Friction velocity, and (b) Monin Obukhov lengths.

The eddy diffusivity coefficient (K), HONO gradient, and HONO fluxes calculated for one of the sunny days (27 January, 2014) are shown in Figure 5.21. The HONO flux shows a peak around 1100 hours of $(3.1\pm0.2)\text{x}10^{10}$ molec. $\text{cm}^{-2}\ \text{s}^{-1}$ (Figure 5.22). Figure 5.23 shows the 2014 hourly average sunny days HONO fluxes (black line and dots). The average sunny days HONO fluxes roughly follow solar irradiance, with a maximum of $(1.7\pm0.3)\text{x}10^{10}$ molec. $\text{cm}^{-2}\ \text{s}^{-1}$ occurring at 1100 hours. Comparison of sunny days hourly average fluxes show that the 2012 and 2014 fluxes follow similar temporal trend but 2014 HONO surface fluxes were smaller (average difference of $2.73\text{x}10^{9}$ molec. $\text{cm}^{-2}\ \text{s}^{-1}$ between 0600 and 1700 hours). Despite of the considerable variation in the flux, it is clear that upward HONO fluxes were observed during sunny days supporting the idea of HONO formation at the ground.

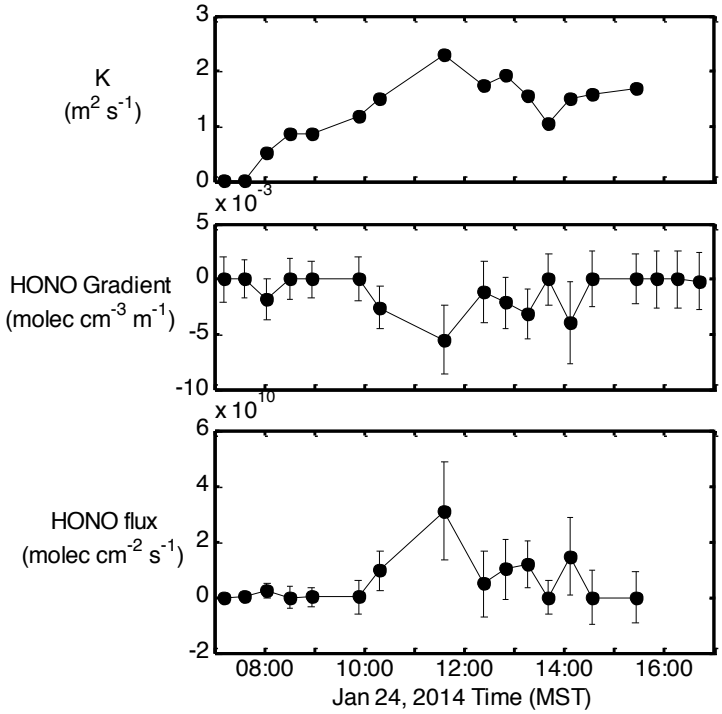

Figure 5.22 HONO fluxes on 24 January 2014. Top panel shows eddy diffusivity coefficients calculated using equation 3.5, middle panel shows HONO gradients calculated using equation 3.8, and lower panel shows HONO fluxes calculated using equation 3.4.

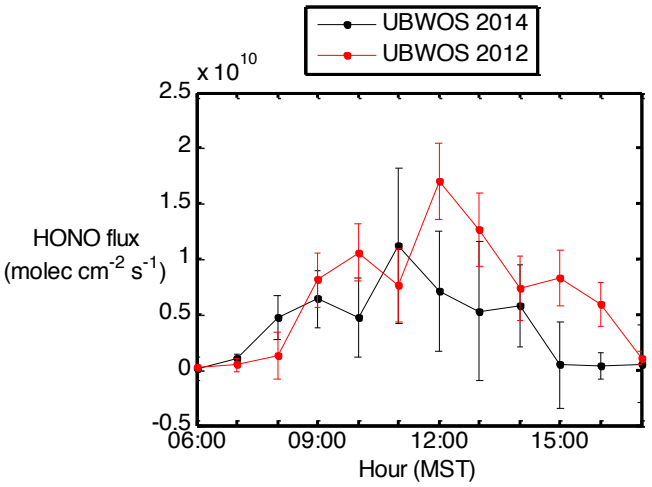

Figure 5.23 Sunny days hourly average HONO fluxes in 2014 (black dots and line) and 2012 (red dots and line).

5.3.7 HONO daytime sources

Comparison of steady state HONO concentrations ($HONO_{ss}$) (Figure 5.24 red line) and lower light path HONO mixing ratios (Figure 5.24 black line) points towards the presence of an unknown daytime source of HONO on sunny days. On average, measured HONO mixing ratios were about 91 pptv higher than $HONO_{ss}$ between 0600 and 1700 hours. The production rate of the unknown daytime source ($P_{unknown}$) was calculated using the approach described in section 3.3.

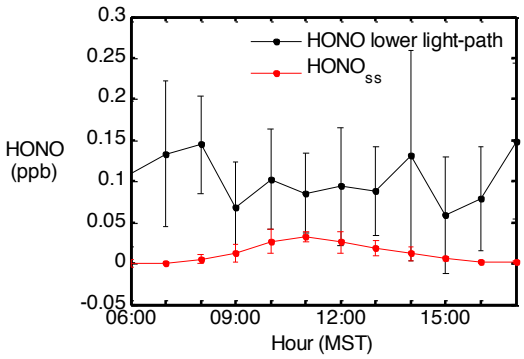

Figure 5.24 HONO mixing ratios measured on the lower light path (black dot and line) and calculated $HONO_{ss}$ (red line and dots).

The HONO production and loss rates were calculated using in-situ NO (NOAA), jHONO (NOAA), and lower light path DOAS HONO measurements. $P_{unknown}$ was calculated using the pseudo steady state approach described in section 3.3. Due to the lack of measured and modeled OH mixing ratios in 2014, we used the surface OH mixing

ratios output by a box model that simulated ozone pollution events during UBWOS 2013 (Edwards et al., 2014). The OH mixing ratios used in the 2014 study was an average of the six days that was model for UBWOS 203. The uncertainty of the OH mixing ratios was the percent difference between highest and lowest noontime HONO. The uncertainties of the formation and loss rates of HONO and $P_{unknown}$ were calculated by propagating the uncertainties of their rate constants and measurements errors.

Figure 5.25 shows the sunny day hourly average of $HONO_{formation}$ (red line, equation 3.8a), $HONO_{photolysis}$ (green line, equation 3.8b), $HONO_{oxidation}$ (blue line, equation 3.8c), and $P_{unknown}$ (black line). To determine whether surface fluxes of HONO can explain the calculated $P_{unknown}$, the sunny days HONO fluxes were (Figure 5.25) converted into column HONO flux rates (Figure 5.25, magenta line) by dividing HONO fluxes by H, the height at which the influence of HONO surface fluxes on the total HONO column becomes negligible (equation 3.9).

To determine H, a simple RCAT 8.2 simulation was performed based on one of the 2012 sunny days HONO flux run (27 January). The purpose of this model simulation was to examine the effect of atmospheric stability on HONO vertical profiles rather than to model the HONO boundary layer chemical system, the latter being an unrealistic task, as RCAT 8.2 does not include a snow module. For this study, the only changes made to the UBWOS 2012 model run were the photolysis rates and eddy diffusivity coefficients, which were modified based on measured and calculated data (Figure 5.26). Figure 5.26 shows that the 2014 sunny days eddy diffusivities are about half of their 2012 counterpart (Figure 5.26a) and that the 2014 sunny days HONO photolysis rates are a factor of about 2.5 higher than the 2012 HONO photolysis rates. As expected, the smaller eddy

diffusivity coefficients and greater HONO photolysis rates reduced H, as HONO release from the ground surface is rapidly photolyzed while being slowly vertically transported (Figure 5.27). While H in 2012 was about 273±113 m agl, H in 2014 was 86±8 m agl.

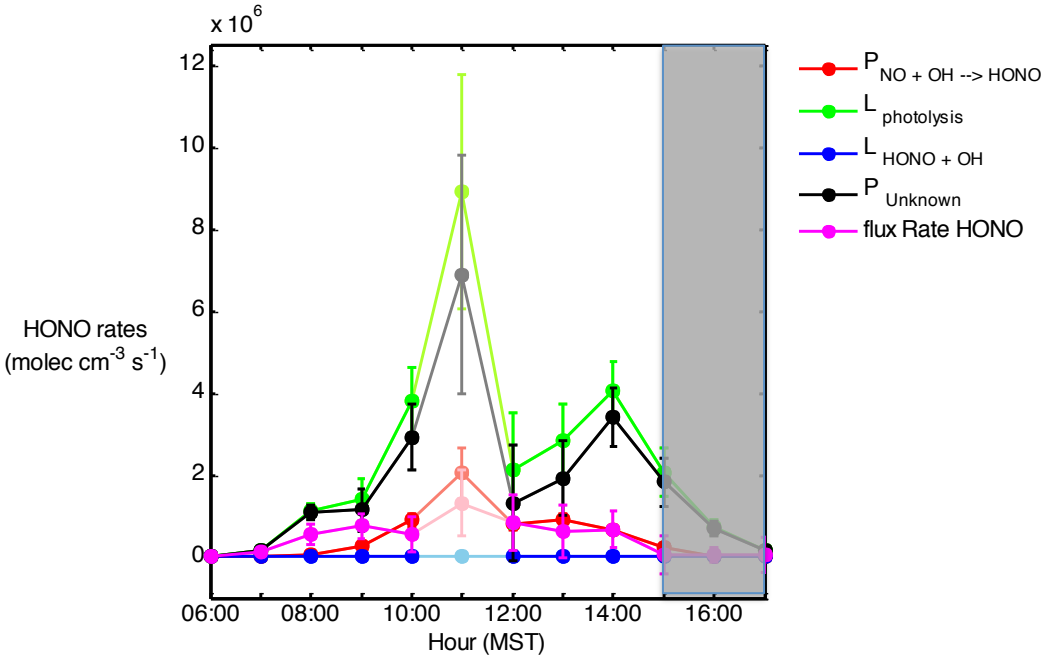

Figure 5.25 Sunny days hourly average 2014 HONO rates. HONO production (red line, equation 3.13a), HONO photolysis (green line, equation 3.13b), HONO oxidation (blue line, equation 3.13c), $P_{unknown}$ (black line, equation 3.11) and HONO flux rate (magenta line, equation 3.11). Grey box highlights the time when HONO lifetimes are too long to assume pseudo steady state conditions.

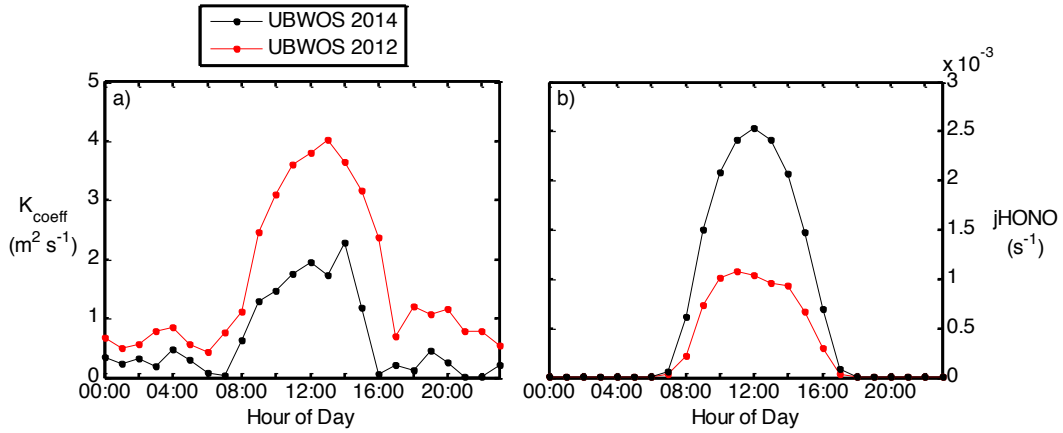

Figure 5.26 Comparison of 2012 (red dots and line) and 2014 (black dots and line) sunny days hourly average (a) eddy diffusivity coefficients and (b) HONO photolysis rates.

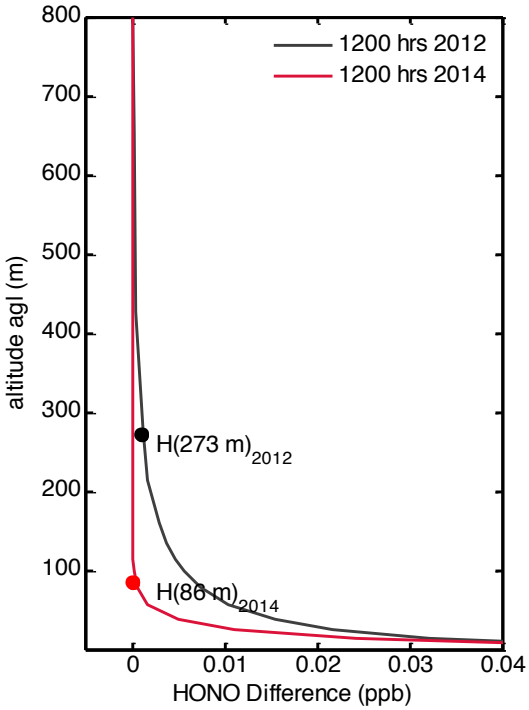

Figure 5.27 Height H for 2012 (black dot) and for 2014 (red dot). The vertical profiles are the differences between HONO mixing ratios modeled with HONO surface flux and the HONO mixing ratios modeled without HONO surface flux.

The HONO formation and loss rates at 1100 hours in Figure 5.25 are shown in a different shade because at this hour, due to missing data, only one data point was used to calculate the respective HONO rates.

Figure 5.25 shows one of the main findings in this study, i.e. when the steady-state approach is valid, the daytime HONO flux and missing HONO source agree within the errors near noontime, indicating that missing daytime HONO is formed through a photolytic formation pathway at the ground.

5.4 Discussion and conclusion

The recent discovery of high wintertime ozone episodes in snow covered areas influenced by oil and gas drilling activities led scientists to investigate HONO and the role it plays in the production of wintertime ozone. Few HONO observations were made in this type of environment, Rappengluck et al., 2014 measured a maximum HONO median of 1.096 ppbv around noontime in Wyoming and Stoeckenius and McNally (2014) reported about 0.55±0.58 ppbv of daytime HONO observed in the UB in 2013. HONO studies in Polar Regions show that in-situ measurements might overestimate HONO concentrations due to interferences with PNA (Legrand et al., 2014). In order to resolve the uncertainties revolving the accuracy of HONO measurements, an inter-comparison involving four in-situ instruments (AcidCIMS, iCIMS, LOPAP, and ACES)

and the LP-DOAS DOAS was carried out in the UB in 2014. The inter-comparison shows that the LP-DOAS consistently measured lower levels of HONO than the in-situ instruments. While the average daytime HONO measured by the LP-DOAS was about 80 ppt near noontime on the lower light path, in-situ instruments measured between 150 ppt and 300 ppt of HONO near noontime. Interference comparison studies during UBWOS 2014 show that in-situ HONO measurements tend to suffer from PNA interferences overestimating the amount of measured HONO (Stoeckenius, 2014). Because the DOAS technique uniquely identifies HONO and measures in the open atmosphere, it does not suffer from chemical interferences. Our UBWOS 2014 HONO measurements indicate that extremely high levels of HONO (as seen in UBWOS 2013) are probably the result of instrument errors.

Most HONO flux studies over snow were carried out in Polar Regions. Legrand et al., 2014 estimated a mean diurnal HONO snow emission ranging between 0.5 $x10^{9}$ molecules cm^{-2} s^{-1} and $0.8x10^{9}$ molecules cm^{-2} s^{-1} in Antarctica, Honrath et al. (2002) measured 24-hours average HONO emission of $4.64x10^{7}$ molecules cm^{-2} s^{-1} in Greenland, and Zhou et al. (2001) estimated HONO flux to be $6.69x10^{8}$ molecules cm^{-2} s^{-1} within 2 hours of noontime in the Arctic. In contrast, HONO fluxes calculated during UBWOS 2014 were higher ($7.86\pm6.24x10^{9}$ molecules cm^{-2} s^{-1} near noontime) than Polar Regions HONO fluxes, most likely due to much higher NO_x levels encountered in the UB. Beine et al. (2008) measured peak emissions fluxes of about $3x10^{10}$ molecules cm^{-2} s^{-1} from the Sierra Nevada snow packs, but their emissions combined NO, NO_2, and HONO fluxes.

Similar to HONO fluxes measured in Polar Regions, UBWOS 2014 HONO fluxes follow solar irradiance. The dependency of HONO fluxes on solar radiation was investigated using a similar approach to that used in UBWOS 2012 (Chapter 4). Sunny day hourly average daytime HONO fluxes were plotted against [NO_2] x solar radiation and [HNO_3] x UV solar radiation (Figure 5.28). The proposed HONO sources, photolysis of nitrate and photo-enhanced conversion of NO_2 on humic acids, both within or on the snow, are active in different wavelength ranges and are expected to correlate with [HNO_3] x UV solar radiation and [NO_2] x solar radiation, respectively. The UV solar radiation was calculated by multiplying solar radiation with $jHNO_3/jNO_2$. The gas phase NO_2 and HNO_3 concentrations were used as a proxy of NO_2 and HNO_3/NO_3^- concentrations on the surface and in the snow interstitial air, where HONO production was expected.

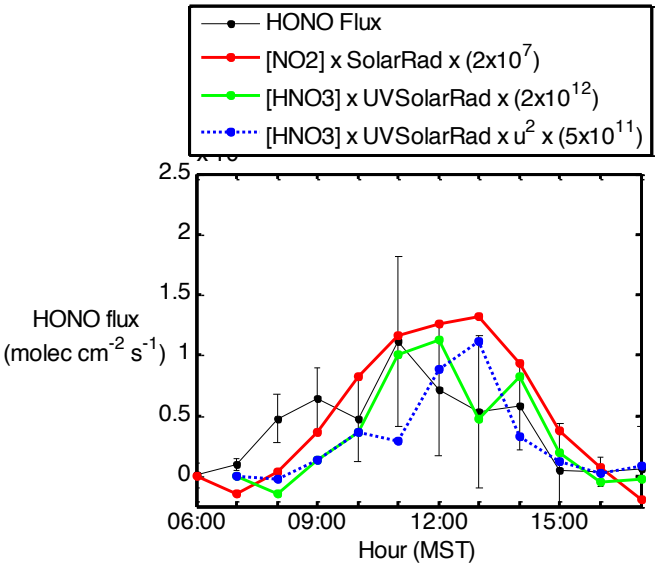

Figure 5.28 Sunny days hourly average HONO fluxes (black dots and line), product of NO_2 mixing ratios measured in the lowest light path and solar radiation (red line),

product of gas-phase nitric acid and UV solar radiation (green line), product of gas-phase nitric acid, UV solar radiation, and wind speed squared.

Correlation plots show that HONO flux correlates with both [NO_2] x solar radiation (R^2 = 0.59) and [HNO_3] x UV solar radiation (R^2 = 0.48) (Figure 5.29) making it impossible to determine which pathway dominated during UBWOS 2014.

Two model studies, one based on a coupled atmosphere-snow model that was validated with data from GSHOX (Greenland Summit Halogen-HOx experiment) (Thomas et al., 2011), and the other based on a 1-D air-snowpack model of HONO at the south pole (Liao et al., 2008), show that HONO concentrations above the snowpack are sensitive to wind pumping, which transports HONO emitted in the firn to the air above the snow surface. Thomas et al., (2012) determined that wind pumping is proportional to u^2 (square of wind speed) and parameterized the vertical wind pumping using:

$$U_{pumping} = \frac{6k\rho_{air}}{\pi\mu\lambda_{surf}} \frac{h}{\lambda_{surf}} \frac{\sqrt{\alpha^2+1}}{\alpha} u_{10}^2 \exp\left(\frac{-2\pi\sqrt{\alpha^2+1}\,z}{\alpha\lambda_{surf}}\right)$$

(equation 5.1; Cunningham and Waddington, 1993)

Results from Thomas et al., (2012) show that HONO formed within the snowpack seems to photolyze before it can reach the atmosphere, thus they conclude that the observed HONO mixing ratios in Polar boundary layers would have to involve a HONO source on particles, in the gas phase, or at the top of the snowpack.

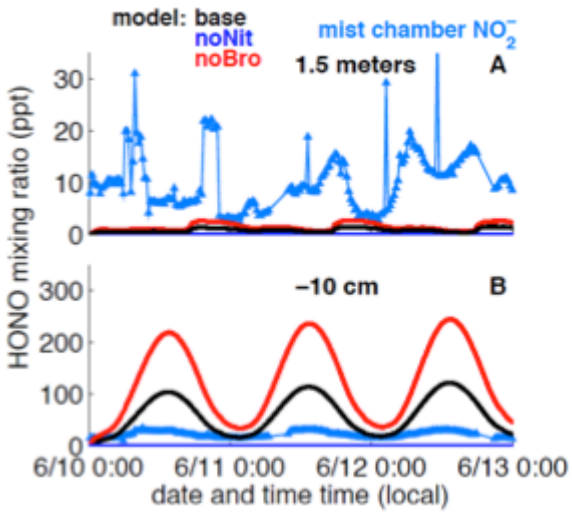

Figure 5.29 Comparison of model predicted HONO for three day model run (10 – 13 June 2008) for the base run ($3.3x10^{-4}$ of Br^- and $8.8x10^{-3}$ NO_3^- in QLL), noNit (no nitrate in QLL), and noBro (no bromine in QLL) cases with mist chamber measurements of soluble nitrite with one inlet 1.5 m above the snow surface (upper panel) and one inlet 10 cm below the snow surface (lower panel). Adapted from Thomas et al. (2012)

To assess whether HONO was transported from within the firn or formed on the surface of the snow, HONO fluxes were compared to $[NO_2]$ x solar radiation x u^2 and $[HNO_3]$ x UV solar radiation x u^2 where u represents the wind speed at 10 m agl (equation 5.1). The poor correlation of $[NO_2]$ x solar radiation x u^2 and $[HNO_3]$ x UV solar radiation x u^2 with HONO flux show that wind pumping did not play an important role in the production of HONO over snow, hence our results agree with Thomas et al., 2012 findings in that the observed HONO was most likely formed at the top of the snowpack and not in the snow interstitial air. We did not consider emissions of HONO from soil nitrite as an important source of HONO as nitrite production from biological reaction was inefficient due to low soil temperatures (about -4°C).

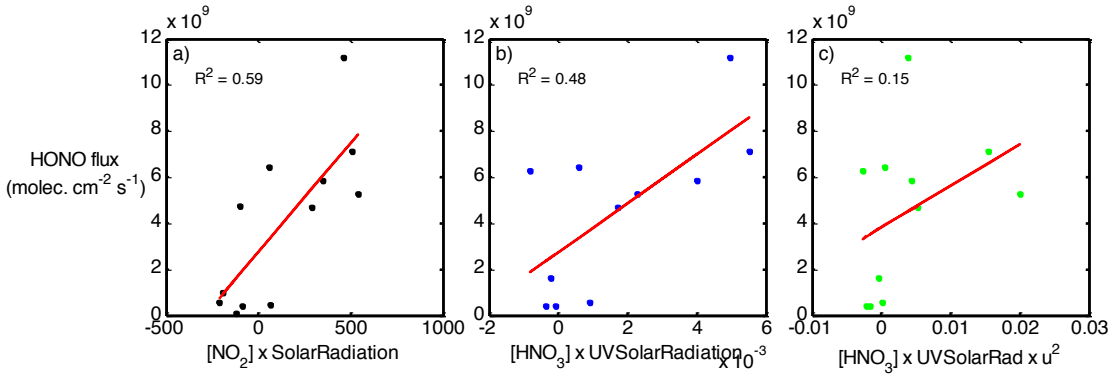

Figure 5.30 Correlation plot of (a) sunny days hourly average HONO flux vs. $[NO_2]$ x solar radiation, (b) sunny days hourly average HONO flux vs. $[HONO_3]$ x UV solar radiation, and (c) sunny days hourly average HONO flux vs. $[HNO_3]$ x UV solar radiation x u^2.

Comparison between the unknown production rate of HONO ($P_{unknown}$) and HONO flux rate shows that about half (54±% 15) of the noontime and early morning $P_{unknown}$ can be explained by the surface HONO flux rate, suggesting that a large portion of the HONO sources at noon and early morning come from the surface. The strong correlation of HONO flux and $[NO_2]$ x solar radiation suggests that photo-enhanced conversion of NO_2 on surfaces might have played an important role on daytime HONO formation at noontime. The calculated noontime uptake coefficient for the photo-enhanced conversion of NO_2 on surfaces (γ_{NO2}) was lower ($7.2x10^{-6}$) than the uptake coefficient obtained by Stemmler et al., (2006) for the light-induced reaction of NO_2 with surface humic acids ($2x10^{-5}$), however, our calculated γ_{NO2} is close to the coefficient calculated by Stemmler et al., (2007) for aerosol surfaces ($6x10^{-6}$). In the early morning, photo-enhanced conversion of NO_2 does not explain the observed HONO flux (Figure

5.28). At this time, other non-photolytic surface HONO sources, such as deposition of HONO at night and re-emission during the day, might have played an important role, however, there are no studies of HONO formation by acid displacement over snow. Soil nitrite release is not expected be a dominant source of HONO due to the low temperatures and the alkaline soil. In the afternoon, as HONO flux underestimates $P_{unknwon}$, other non-surface sources might have played a more important role, most likely such as gas phase chemistry or heterogeneous chemistry on aerosols.

Chapter 6 CONCLUSION AND OUTLOOK

6.1 Conclusion

Despite of decades of research, the formation mechanism of daytime HONO is still not fully understood and there is no consensus on whether daytime HONO is formed on the ground, aerosol surfaces, or through gas phase reactions. Furthermore, little is known about daytime HONO behavior over soil and snow surfaces in polluted rural areas, as most measurements were made in urban, semi-urban, polar, or forested regions. The recent discovery of high wintertime ozone episodes in snow covered areas influenced by oil and gas drilling activities has led to the investigation of HONO chemistry in these environments and the role that HONO plays in the production of wintertime ozone. HONO measurements in the UGRB, Wyoming, and UB, Utah, two regions heavily affected by oil and gas drilling activities, show high levels of daytime HONO (above 500 pptv) during the wintertime. However, questions were raised about the reliability of wintertime HONO observations as recent studies show that many in-situ HONO

measurement methods suffer from PNA interferences, that lead to an overestimate of HONO concentrations by as much as 15% (Legrand et al., 2014).

The UCLA LP-DOAS instrument measured HONO and HONO gradients in the Uintah Basin, located in the northeast corner of Utah, in 2012 and 2014 (as part of UBWOS 2012 and UBWOS 2014 field studies) in the wintertime (from about mid-January to mid-February). The Uintah Basin is highly impacted by oil and gas activities, with about 10,000 active oil and gas wells. The LP-DOAS measured HONO on three light paths of ~2.5 km length covering height intervals from 2 m to 31, 45, and 68 m agl. Meteorological conditions were different between 2012 and 2014. While snow cover was almost absent in 2012, snow depths of up to 0.15 m were observed in 2014. Snow-covered grounds play an important role in determining the HONO budget as snow's high albedo increase UV actinic flux, thus enhancing photolysis of HONO. In addition, snow can promote strong temperature inversions influencing HONO chemistry near the ground.

HONO mixing ratios on the lower light path ranged from below detection limits to 270± 20 ppt with an average of 74 ppt in 2012. These levels are lower than HONO measured in polluted urban areas but comparable to levels measured in rural environments. Distinct daytime negative vertical gradients of HONO were observed in 2012, with higher levels of HONO measured on the lower than upper light paths. These gradients indicate that surface observations of HONO are not representative of the entire boundary layer, thus care must be taken when interpreting HONO surface data.

HONO vertical profiles were retrieved using a novel least square minimization approach, where the average mixing ratios of HONO along the light paths were simulated

using a height dependent exponential function. HONO vertical profiles show higher HONO mixing ratios near the surface than aloft and a rapid decay of HONO mixing ratios above 20 m agl in 2012, indicating that HONO has a surface source.

The retrieved HONO vertical profiles and NOAA micrometeorological data were used to calculate HONO fluxes (at 19 m agl) using the gradient method described in Businger (1986). The sunny days hourly average HONO fluxes were positive with a maximum HONO flux at noontime of (1.7±0.3) $x10^{10}$ molec. cm^{-2} s^{-1}. The sunny days hourly average HONO fluxes follow the temporal trend of solar irradiance, i.e., they peaked near noontime, supporting the idea of a photolytic surface HONO source in 2012. Sunny days were days when the photolytic lifetime of HONO was about 13 minutes at noon and the steady state assumption was applied.

Photo-enhanced conversion of NO_2 to HONO on surfaces and photolysis of surface adsorbed HNO_3 yielding HONO are active in different wavelength ranges and were expected to correlate with [NO_2] x solar radiation and [HNO_3] x UV solar radiation, respectively. Sunny days HONO flux correlated strongly with both [NO_2] x solar radiation (R^2 = 0.58) and [HNO_3] x UV solar radiation (R^2 = 0.66) making it difficult to determine which formation pathway dominated in 2012. Analysis of a plume event characterized by a sudden and concurrent increase of NO_2, HONO mixing ratios, and HONO flux allowed us to determine that under conditions of high NO_2 levels, conversion of NO_2 on ground surfaces is most likely the source of daytime HONO. These conclusions were obtained by running a 1D box model under two scenarios: one that included a photolytic NO_2 ground source (Wong et al., 2012), and one that did not. While the model simulation without the photolytic NO_2 ground source under-predicted observed

HONO mixing ratios, HONO mixing ratios from the photolytic NO_2 model were comparable to the observed HONO, indicating that during NO_2 plume events, or under high NO_2 conditions, photo-enhanced conversion of NO_2 on surfaces is potentially a dominant source of HONO. When the same model, which included the photolytic NO_2 ground source, was run for a day with moderate NO_2 levels (~2 ppb), it under predicted HONO mixing ratios, indicating that on days of moderate NO_2 levels, photolytic conversion of NO_2 is not the dominant HONO formation pathway and photolysis of HNO_3 adsorbed on the ground might play an important role, as shown by the strong correlation between HONO flux and [HNO_3] x UV solar radiation. However, additional measurements, such as concentration of surface nitrate/HNO_3, are needed to confirm this theory. An alternate HONO formation mechanism that is proportional to [NO_2] x solar radiation is the daytime displacement of HONO by strong acids, such as HNO_3 and HCl (VandenBoer et al., 2014). To determine if this HONO formation mechanism was viable during UBWOS 2012, we compared the total number of HONO deposited at night (calculated using HONO uptake frequency and HONO concentrations output by the lowest box of a 1-D model for 27 January, 2012) and total number of HONO molecules cm^{-2} released by the daytime HONO surface flux. The integrated HONO molecules cm^{-2} of the previous night ($1.84x10^{14}$ molecules cm^{-2}) was slightly lower than the integrated daytime HONO molecules cm^{-2} ($2.84x10^{14}$ molecules cm^{-2}), indicating that displacement of acid could also explain the observed HONO flux under low NO_2 conditions. Another HONO formation mechanism that would result in positive surface HONO flux is HONO formation from soil nitrite (Sue et al. 2011). However, emission of HONO through this

pathway likely played a minor role, as the alkaline and cold soil would render this HONO formation mechanism unimportant.

In order to assess the importance of the photolytic ground surface source to the total HONO budget, we calculated the formation rate of HONO, due to HONO flux, by dividing the sunny days HONO flux by H (273 m agl), the height at which the influence of HONO surface flux on the total HONO column becomes negligible. Comparison of the missing source of HONO ($P_{unknwon}$) and HONO surface flux rate shows that HONO surface flux rate accounts for (63±32%) of the $P_{unknown}$ throughout the day, and 90±30% of the $P_{unknown}$ near noontime, indicating that photolytic surfaces sources of HONO, instead of HONO formation pathways in the gas phase or on aerosols, were the dominant sources of HONO in 2012.

HONO mixing ratios measured on the lower light path ranged from below detection limits to 470 ± 40 ppt with a field study average of 96 ppt in 2014. The relatively low levels of HONO measured in 2014 were surprising, as previous measurements in regions with active oil and gas wells showed high levels of HONO released from the snow (above 500 ppt). Comparison of DOAS HONO measurements with four in-situ instruments shows that the DOAS system consistently measured the lowest HONO levels. Analysis of PNA interferences shows that some in-situ measurements overestimate HONO concentrations in the presence of PNA (Legrand et al., 2014; J. Roberts and P. Veres, personal communication, 2014). The DOAS technique does not suffer from chemical interferences because it uniquely identifies HONO and measures in the open atmosphere, therefore the DOAS 2014 HONO observations were considered as the reference measurements for the UBWOS 2014 study. A model study

carried out by NOAA (Edward et al., 2014) support our HONO measurements as high levels of HONO, such as the ones measured by NOAA's AcidCIMS in 2013 (~ 500 ppt daytime HONO), greatly overestimated O_3 production (up to 20 ppb) in the UB.

2014 HONO vertical profiles and HONO fluxes were retrieved using the same approach as in 2012. HONO vertical profiles also show higher HONO mixing ratios near the surface and a rapid decay of HONO mixing ratios with height. The sunny days hourly average HONO fluxes were also positive with a maximum HONO flux near noontime of $(1.1\pm0.7)x10^{10}$ molec. cm^{-2} s^{-1}. The sunny days hourly average HONO fluxes also follow a similar temporal trend as solar irradiance, supporting the hypothesis of a photolytic surface HONO source in 2014.

The proposed photolytic surface HONO sources on the snow surface and in the firn include photo-enhanced conversion of NO_2 and nitrate photolysis (which is expected to correlate with $[HNO_3]$ x UV solar radiation). Correlation between 2014 HONO flux with $[NO_2]$ x solar radiation (R^2 = 0.59) and HONO flux with $[HNO_3]$ x UV solar radiation (R^2 = 0.48) were also strong. Unfortunately, the lack of high NO_2 events, insufficient ancillary data, and absence of snow module in the 1-D model, prevented us to determine which photolytic surface HONO formation pathway dominated in 2014. However, we were able to determine if HONO was formed on the snow surface or in the firn by comparing the calculated HONO fluxes with wind speeds. Model studies (Liao et al., 2008; Thomas et al., 2011, 2012) have shown that HONO concentrations above the snowpack are sensitive to wind pumping, which transports HONO emitted in the firn to the air above the snow surface. Wind pumping is characterized by u^2 (where u is the wind speed at 10 m agl). The poor correlation between HONO flux with $[NO_2]$ x solar

radiation x u^2 and HONO flux with [HNO_3] x UV solar radiation x u^2 indicate that wind pumping did not play an important role in the observed HONO over snow, leading us to conclude that the observed HONO was formed at the top of the snowpack. This result is supported by the surprisingly similar HONO fluxes measured in 2012 and 2014, which indicate the HONO formation mechanisms during these two years were probably very similar.

The HONO surface flux rate was calculated by dividing the HONO flux by H (86 m agl) , the height at which the influence of HONO surface flux on the total HONO column becomes negligible. Comparison of the missing source of HONO ($P_{unknwon}$) and HONO surface flux rate shows that HONO surface flux rate accounts for (54±% 15) of the $P_{unknown}$ in the early morning and noontime, suggesting that HONO sources at noon and early morning are light dependent and are produced on the snow surface.

To summarize, this dissertation shows that in oil and gas production regions, like in many other environments, photolytic surface HONO formation pathways, on both soil and snow, are the dominant source of daytime HONO. Our results also show that previous measurements of HONO over snow (in Polar Regions and polluted rural areas) were overestimated most likely due to chemical interferences in the inlet. Nitrate photolysis, the HONO formation pathway currently assumed to be the dominant HONO formation pathway over snow, is not important in polluted rural environments.

6.2 Outlook

As shown in this dissertation, and other HONO studies, obtaining accurate measurements of HONO and determining its daytime formation source/s are challenging

tasks. In-situ HONO measurements in cold environments tend to suffer from PNA interferences, overestimating the amount of HONO that is measured. Comparison between DOAS HONO measurements with in-situ observations showed that DOAS consistently measured lower HONO levels in 2014 confirming that in-situ measurements suffered from chemical interferences. This finding questions the HONO studies that have previously been carried out in Polar Regions, as these HONO measurements were made with in-situ instruments. It is very probable that HONO was overestimated in these studies and the proposed HONO source over snow, nitrate photolysis, is not as important as these studies suggest. Therefore, previous HONO measurements over snow need to be reevaluated by taking into account PNA interferences or new measurements of HONO, with techniques that do not suffer from interferences, need to be carried out. Also, as my dissertation proposes that HONO is formed on the surface and not in the snow firn, I believe that laboratory and field studies should also focus on determining where the HONO production takes place. This can be achieved through tests that look into the efficiency of HONO photolysis in the firn (i.e., if HONO produced in the firn is photolyzed before leaving the firn) and determining if HONO produced in the firn can be efficiently transported to the snow surface. As for improving the understanding of HONO formation pathways over snow, a number of measurements should be carried out, such as uptake of HONO over snow, concentrations of humic acid or organics on the snow surface, and fluxes of NO_2 and HNO_3 on snow.

Another challenge in determining the daytime formation mechanism of HONO, as concluded in this dissertation and other recent studies, is that daytime HONO is formed through different formation mechanisms. Hence, to fully understand the daytime HONO

budget, measurements pertaining to all the potential mechanisms are needed. For instance, to better assess the daytime HONO budget in a polluted rural environment, measurements of nocturnal uptake of HONO and daytime surface fluxes of HNO_3 and other strong acids would be needed to quantify HONO formation through acid displacement. Measurements of soil nitrite concentrations would be needed to confirm the significance of soil emissions as a HONO source. To determine the significance of photolysis of surface adsorbed HNO_3 acid, measurements of surface adsorbed nitric acid and photolysis of nitric acid on soil would be needed. As for the photo-enhanced conversion of NO_2 on ground surfaces, NO_2 surface flux and uptake of NO_2 on the ground would be needed to quantify this formation pathway. Uptake of NO_2 and HNO_3 on aerosols and nitro-phenol measurements would also be needed to determine the importance of heterogeneous and gas phase chemistry play as a HONO source. In addition, more HONO flux and/or HONO concentration profiles measurements near the surface are needed. HONO vertical transport is a key parameter in determining the HONO budget as HONO levels significantly decrease with height, something that needs to be taken into consideration when looking at HONO budgets to avoid over-predicting or under-predicting the effects of HONO in the lower troposphere.

REFERENCES

Ahmadov, R., McKeen, S., Trainer, M., Banta, R., Brewer, A., Brown, S., . . . Zamora, R. (2015). Understanding high wintertime ozone pollution events in an oil- and natural gas-producing region of the western US. *Atmospheric Chemistry and Physics, 15*(1), 411-429. doi:10.5194/acp-15-411-2015

Alicke, B., Geyer, A., Hofzumahaus, A., Holland, F., Konrad, S., Patz, H. W., . . . Platt, U. (2003). OH formation by HONO photolysis during the BERLIOZ experiment. *Journal of Geophysical Research-Atmospheres, 108*(D4). doi:10.1029/2001jd000579

Alicke, B., Platt, U., and Stutz, J. (2002). Impact of nitrous acid photolysis on the total hydroxyl radical budget during the Limitation of Oxidant Production/Pianura Padana Produzione di Ozono study in Milan. *Journal of Geophysical Research-Atmospheres, 107*(D22). doi:10.1029/2000jd000075

Ammann, M., Kalberer, M., Jost, D. T., Tobler, L., Rossler, E., Piguet, D., . . . Baltensperger, U. (1998). Heterogeneous production of nitrous acid on soot in polluted air masses. *Nature, 395*(6698), 157-160. doi:10.1038/25965

AndresHernandez, M. D. (1996). A DOAS study on the origin of nitrous acid at urban and non-urban sites (vol 30, pg 175, 1996). *Atmospheric Environment, 30*(23), 4103-4103.

Arnorosoa, A., Beine, H. J., Sparapani, R., Nardino, M., and Allegrini, I. (2006). Observation of coinciding arctic boundary layer ozone depletion and snow surface emissions of nitrous acid. *Atmospheric Environment, 40*(11), 1949-1956. doi:10.1016/j.atmosenv.2005.11.027

Aubin, D. G., and Abbatt, J. P. D. (2007). Interaction of NO2 with hydrocarbon soot: Focus on HONO yield, surface modification, and mechanism. *Journal of Physical Chemistry A, 111*(28), 6263-6273. doi:10.1021/jp068884h

Barret, M., Domine, F., Houdier, S., Gallet, J. C., Weibring, P., Walega, J., . . . Richter, D. (2011). Formaldehyde in the Alaskan Arctic snowpack: Partitioning and physical processes involved in air-snow exchanges. *Journal of Geophysical Research-Atmospheres, 116*. doi:10.1029/2011jd016038

Bartels-Rausch, T., Brigante, M., Elshorbany, Y. F., Ammann, M., D'Anna, B., George, C., . . . Kleffmann, J. (2010). Humic acid in ice Photo-enhanced conversion of nitrogen dioxide into nitrous acid. *Atmospheric Environment, 44*(40), 5443-5450. doi:10.1016/j.atmosenv.2009.12.025

Bedjanian, Y., and El Zein, A. (2012). Interaction of NO2 with TiO2 Surface Under UV Irradiation: Products Study. *Journal of Physical Chemistry A, 116*(7), 1758-1764. doi:10.1021/jp210078b

Beine, H., Colussi, A. J., Amoroso, A., Esposito, G., Montagnoli, M., and Hoffmann, M. R. (2008). HONO emissions from snow surfaces. *Environmental Research Letters, 3*(4). doi:10.1088/1748-9326/3/4/045005

Beine, H. J., Amoroso, A., Domine, F., King, M. D., Nardino, M., Ianniello, A., and France, J. L. (2006). Surprisingly small HONO emissions from snow surfaces at Browning Pass, Antarctica. *Atmospheric Chemistry and Physics, 6*, 2569-2580.

Beine, H. J., Amoroso, A., Esposito, G., Sparapani, R., Ianniello, A., Georgiadis, T., . . . Domine, F. (2005). Deposition of atmospheric nitrous acid on alkaline snow surfaces. *Geophysical Research Letters, 32*(10). doi:10.1029/2005gl022589

Beine, H. J., Domine, F., Simpson, W., Honrath, R. E., Sparapani, R., Zhou, X. L., and King, M. (2002). Snow-pile and chamber experiments during the Polar Sunrise Experiment 'Alert 2000': exploration of nitrogen chemistry. *Atmospheric Environment, 36*(15-16), 2707-2719. doi:10.1016/s1352-2310(02)00120-6

Beine, H. J., Honrath, R. E., Domine, F., Simpson, W. R., and Fuentes, J. D. (2002). NOx during background and ozone depletion periods at Alert: Fluxes above the snow surface. *Journal of Geophysical Research-Atmospheres, 107*(D21). doi:10.1029/2002jd002082

Bejan, I., Abd El Aal, Y., Barnes, I., Benter, T., Bohn, B., Wiesen, P., and Kleffmann, J. (2006). The photolysis of ortho-nitrophenols: a new gas phase source of HONO. *Physical Chemistry Chemical Physics, 8*(17), 2028-2035. doi:10.1039/b516590c

Bey, I., Aumont, B., and Toupance, G. (1997). The nighttime production of OH radicals in the continental troposphere. *Geophysical Research Letters, 24*(9), 1067-1070. doi:10.1029/97gl00889

Bogumil, K., Orphal, J., Homann, T., Voigt, S., Spietz, P., Fleischmann, O. C., . . . Burrows, J. P. (2003). Measurements of molecular absorption spectra with the SCIAMACHY pre-flight model: instrument characterization and reference data for atmospheric remote-sensing in the 230-2380 nm region. *Journal of Photochemistry and Photobiology a-Chemistry, 157*(2-3), 167-184. doi:10.1016/s1010-6030(03)00062-5

Boxe, C. S., Colussi, A. J., Hoffmann, M. R., Murphy, J. G., Wooldridge, P. J., Bertram, T. H., and Cohen, R. C. (2005). Photochemical production and release of gaseous NO2 from nitrate-doped water ice. *Journal of Physical Chemistry A, 109*(38), 8520-8525. doi:10.1021/jp0518815

Broske, R., Kleffmann, J., and Wiesen, P. (2003). Heterogeneous conversion of NO2 on secondary organic aerosol surfaces: A possible source of nitrous acid (HONO) in the atmosphere? *Atmospheric Chemistry and Physics, 3*, 469-474.

Burkholder, J. B., Mellouki, A., Talukdar, R., and Ravishankara, A. R. (1992). Rae coefficeints for the reaction of OH with HONO between 298-K and 373-K. *International Journal of Chemical Kinetics, 24*(8), 711-725. doi:10.1002/kin.550240805

Businger, J. A. (1986). Evaluation of the accuracy with which dry deposition can be measured with current micrometeorological techniques. *Journal of Climate and Applied Meteorology, 25*(8), 1100-1124. doi:10.1175/1520-0450(1986)025<1100:eotaww>2.0.co;2

Butler, J. R., and England, J. L. (1979). *Vegetation map of the southeastern Uinta Basin, Utah and Colorado*. Retrieved from

Calvert, J. G., Yarwood, G., and Dunker, A. M. (1994). An evaluation of the mechanism of nitrous-acid formation in the urban atmosphere. *Research on Chemical Intermediates, 20*(3-5), 463-502. doi:10.1163/156856794x00423

Carter, W., and Seinfeld, J. (2012). Winter ozone formation and VOC incremental reactivities in the Upper Green River Basin of Wyoming. *Elsevier, 50*, 255-266.

Chance, K., and Orphal, J. (2011). Revised ultraviolet absorption cross sections of H2CO for the HITRAN database. *Journal of Quantitative Spectroscopy and Radiative Transfer, 112*(9), 1509-1510. doi:10.1016/j.jqsrt.2011.02.002

Chen, G., Davis, D., Crawford, J., Nowak, J. B., Eisele, F., Mauldin, R. L., . . . Blake, D. (2001). An investigation of South Pole HOx chemistry: Comparison of model results with ISCAT observations. *Geophysical Research Letters, 28*(19), 3633-3636. doi:10.1029/2001gl013158

Chu, L., and Anastasio, C. (2007). Temperature and wavelength dependence of nitrite photolysis in frozen and aqueous solutions. *Environmental Science and Technology, 41*(10), 3626-3632. doi:10.1021/es062731q

Coleman, T. F., and Li, Y. (1994). On the convergence of interior-reflective Newton methods for nonlinear minimization subject to bounds. *Mathematical Programming, 67*(1), 189-224. doi:10.1007/bf01582221

Coleman, T. F., and Li, Y. Y. (1996). An interior trust region approach for nonlinear minimization subject to bounds. *Siam Journal on Optimization, 6*(2), 418-445. doi:10.1137/0806023

Crosson, E. R. (2008). A cavity ring-down analyzer for measuring atmospheric levels of methane, carbon dioxide, and water vapor. *Applied Physics B-Lasers and Optics, 92*(3), 403-408. doi:10.1007/s00340-008-3135-y

Cunningham, J., and Waddington, E. D. (1993). Air-flox and dry deposition of non-sea salt sulfate in Polar firn - Paleoclimatic implications. *Atmospheric Environment Part a-General Topics, 27*(17-18), 2943-2956. doi:10.1016/0960-1686(93)90327-u

Dearellano, J. V. G., Duynkerke, P. G., and Zeller, K. F. (1995). Atmospheric surface-layer similarity theory applied to chemically reactive species. *Journal of Geophysical Research-Atmospheres, 100*(D1), 1397-1408. doi:10.1029/94jd02434

DeMore, W. B., Sander, S. P., Golden, D. M., Hampson, R. F., Kurylo, M. J., and Howard, C. J. (1997). Chemical Kinetics and Photochemical Data for Use in Stratospheric Modeling. Evaluation No. 12. Pasadena, CA: NASA/JPL.

Dibb, J. E., Arsenault, M., Peterson, M. C., and Honrath, R. E. (2002). Fast nitrogen oxide photochemistry in Summit, Greenland snow. *Atmospheric Environment, 36*(15-16), 2501-2511. doi:10.1016/s1352-2310(02)00130-9

Donaldson, M. A., Berke, A. E., and Raff, J. D. (2014). Uptake of Gas Phase Nitrous Acid onto Boundary Layer Soil Surfaces. *Environmental Science and Technology, 48*(1), 375-383. doi:10.1021/es404156a

Döppenschmidt, A., and Butt, H.-J. (2000). Measuring the Thickness of the Liquid-like Layer on Ice Surfaces with Atomic Force Microscopy. Langmuir, 16(16), 6709–6714. doi:10.1021/la990799w

Dubowski, Y., adn Hoffmann, M. R. (2000). Photochemical transformations in ice: Implications for the fate of chemical species. Geophysical Research Letters, 27(20), 3321–3324. doi:10.1029/2000gl011701

Edwards, P. M., Brown, S. S., Roberts, J. M., Ahmadov, R., Banta, R. M., deGouw, J. A., . . . Zamora, R. (2014). High winter ozone pollution from carbonyl photolysis in an oil and gas basin. *Nature, 514*(7522), 351-+. doi:10.1038/nature13767

Elshorbany, Y. F., Kurtenbach, R., Wiesen, P., Lissi, E., Rubio, M., Villena, G., . . . Kleffmann, J. (2009). Oxidation capacity of the city air of Santiago, Chile. *Atmospheric Chemistry and Physics, 9*(6), 2257-2273.

Elshorbany, Y. F., Steil, B., Bruhl, C., and Lelieveld, J. (2012). Impact of HONO on global atmospheric chemistry calculated with an empirical parameterization in the EMAC model. *Atmospheric Chemistry and Physics, 12*(20), 9977-10000. doi:10.5194/acp-12-9977-2012

Fally, S., Vandaele, A. C., Carleer, M., Hermans, C., Jenouvrier, A., Merienne, M. F., . . . Colin, R. (2000). Fourier transform spectroscopy of the O-2 Herzberg bands. III. Absorption cross sections of the collision-induced bands and of the Herzberg continuum. *Journal of Molecular Spectroscopy, 204*(1), 10-20. doi:10.1006/jmsp.2000.8204

Fitzjarrald, D. R., and Lenschow, D. H. (1983). Mean concentration and flux propfiles for chemically reactive species in the atmospheric surface-layer. *Atmospheric Environment, 17*(12), 2505-2512. doi:10.1016/0004-6981(83)90076-8

Flocke, F. M., Weinheimer, A. J., Swanson, A. L., Roberts, J. M., Schmitt, R., and Shertz, S. (2005). On the measurement of PANs by gas chromatography and electron capture detection. *Journal of Atmospheric Chemistry, 52*(1), 19-43. doi:10.1007/s10874-005-6772-0

Fried, A., Wang, Y. H., Cantrell, C., Wert, B., Walega, J., Ridley, B., . . . Ehhalt, D. (2003). Tunable diode laser measurements of formaldehyde during the TOPSE 2000 study: Distributions, trends, and model comparisons. *Journal of Geophysical Research-Atmospheres, 108*(D4). doi:10.1029/2002jd002208

Fuchs, N., and Sutugin, A. (1970). Highly Dispersed Aerosols 1970. *Ann Arbor: Ann Arbor Science Publishers*.

Geiger, H., Barnes, I., Bejan, I., Benter, T., and Spittler, M. (2003). The tropospheric degradation of isoprene: an updated module for the regional atmospheric chemistry mechanism. *Atmospheric Environment, 37*(11), 1503-1519. doi:10.1016/s1352-2310(02)01047-6

George, C., Strekowski, R. S., Kleffmann, J., Stemmler, K., and Ammann, M. (2005). Photoenhanced uptake of gaseous NO2 on solid-organic compounds: a photochemical source of HONO? *Faraday Discussions, 130*, 195-210. doi:10.1039/b417888m

Gerecke, A., Thielmann, A., Gutzwiller, L., and Rossi, M. J. (1998). The chemical kinetics of HONO formation resulting from heterogeneous interaction of NO2 with flame soot. *Geophysical Research Letters, 25*(13), 2453-2456. doi:10.1029/98gl01796

Gilman, J. B., Burkhart, J. F., Lerner, B. M., Williams, E. J., Kuster, W. C., Goldan, P. D., . . . de Gouw, J. A. (2010). Ozone variability and halogen oxidation within the Arctic and sub-Arctic springtime boundary layer. *Atmospheric Chemistry and Physics, 10*(21), 10223-10236. doi:10.5194/acp-10-10223-2010

Goldan, P. D., Kuster, W. C., Williams, E., Murphy, P. C., Fehsenfeld, F. C., and Meagher, J. (2004). Nonmethane hydrocarbon and oxy hydrocarbon measurements during the 2002 New England Air Quality Study. *Journal of Geophysical Research-Atmospheres, 109*(D21). doi:10.1029/2003jd004455

Grannas, A. M., Jones, A. E., Dibb, J., Ammann, M., Anastasio, C., Beine, H. J., . . . Zhu, T. (2007). An overview of snow photochemistry: evidence, mechanisms and impacts. *Atmospheric Chemistry and Physics, 7*(16), 4329-4373.

Grannas, A. M., Shepson, P. B., Guimbaud, C., Sumner, A. L., Albert, M., Simpson, W., . . . Zhou, X. L. (2002). A study of photochemical and physical processes affecting carbonyl

compounds in the Arctic atmospheric boundary layer. *Atmospheric Environment, 36*(15-16), 2733-2742. doi:10.1016/s1352-2310(02)00134-6

Gustafsson, R. J., Kyriakou, G., and Lambert, R. M. (2008). The molecular mechanism of tropospheric nitrous acid production on mineral dust surfaces. *Chemphyschem, 9*(10), 1390-1393. doi:10.1002/cphc.200800259

Gutzwiller, L., Arens, F., Baltensperger, U., Gaggeler, H. W., and Ammann, M. (2002). Significance of semivolatile diesel exhaust organics for secondary HONO formation. *Environmental Science and Technology, 36*(4), 677-682. doi:10.1021/es015673b

Hamba, F. (1993). A modified K-model for chemically reactive species in the planetary boundary-layer. *Journal of Geophysical Research-Atmospheres, 98*(D3), 5173-5182. doi:10.1029/92jd02511

Harrison, R. M., Peak, J. D., and Collins, G. M. (1996). Tropospheric cycle of nitrous acid. *Journal of Geophysical Research-Atmospheres, 101*(D9), 14429-14439. doi:10.1029/96jd00341

Honrath, R. E., Lu, Y., Peterson, M. C., Dibb, J. E., Arsenault, M. A., Cullen, N. J., and Steffen, K. (2002). Vertical fluxes of NOx, HONO, and HNO3 above the snowpack at Summit, Greenland. *Atmospheric Environment, 36*(15-16), 2629-2640. doi:10.1016/s1352-2310(02)00132-2

Honrath, R. E., Peterson, M. C., Guo, S., Dibb, J. E., Shepson, P. B., and Campbell, B. (1999). Evidence of NOx production within or upon ice particles in the Greenland snowpack. *Geophysical Research Letters, 26*(6), 695-698. doi:10.1029/1999gl900077

Jacobi, H.-W., and Hilker, B. (2007). A mechanism for the photochemical transformation of nitrate in snow. Journal of Photochemistry and Photobiology A: Chemistry, 185(2-3), 371–382. doi:10.1016/j.jphotochem.2006.06.039

Jacobi, H. W., Bales, R. C., Honrath, R. E., Peterson, M. C., Dibb, J. E., Swanson, A. L., and Albert, M. R. (2004). Reactive trace gases measured in the interstitial air of surface snow at Summit, Greenland. *Atmospheric Environment, 38*(12), 1687-1697. doi:10.1016/j.atmosenv.2004.01.004

Jacobi, H. W., Frey, M. M., Hutterli, M. A., Bales, R. C., Schrems, O., Cullen, N. J., . . . Koehler, C. (2002). Measurements of hydrogen peroxide and formaldehyde exchange between the atmosphere and surface snow at Summit, Greenland. *Atmospheric Environment, 36*(15-16), 2619-2628. doi:10.1016/s1352-2310(02)00106-1

Jankowski, J. J., Kieber, D. J., and Mopper, K. (1999). Nitrate and nitrite ultraviolet actinometers. *Photochemistry and Photobiology, 70*(3), 319-328. doi:10.1562/0031-8655(1999)070<0319:nanua>2.3.co;2

Khalizov, A. F., Cruz-Quinones, M., and Zhang, R. Y. (2010). Heterogeneous Reaction of NO2 on Fresh and Coated Soot Surfaces. *Journal of Physical Chemistry A, 114*(28), 7516-7524. doi:10.1021/jp1021938

Kleffmann, J., Becker, K. H., and Wiesen, P. (1998). Heterogeneous NO2 conversion processes on acid surfaces: Possible atmospheric implications. *Atmospheric Environment, 32*(16), 2721-2729. doi:10.1016/s1352-2310(98)00065-x

Kleffmann, J., Gavriloaiei, T., Hofzumahaus, A., Holland, F., Koppmann, R., Rupp, L., . . . Wahner, A. (2005). Daytime formation of nitrous acid: a major source of OH radicals in a forest. *Geophysical Research Letters, 32*(5), 4 pp.-4 pp. doi:10.1029/2004gl021732

Kleffmann, J., Heland, J., Kurtenbach, R., Lorzer, J., and Wiesen, P. (2002). A new instrument (LOPAP) for the detection of nitrous acid (HONO). *Environmental Science and Pollution Research*, 48-54.

Knoll, H., Stich, R., Hennig, H., and Stufkens, D. J. (1990). Spectroscopic studies on the mechanism of photolysis of PT(N3)2(P(C6H5)3)2. *Inorganica Chimica Acta, 178*(1), 71-76. doi:10.1016/s0020-1693(00)88136-0

Lammel, G., and Cape, N. (1996). Nitrous Acid and Nitrite in the Atmosphere. *Chemical Society Reviews*.

Langridge, J. M., Gustafsson, R. J., Griffiths, P. T., Cox, R. A., Lambert, R. M., and Jones, R. L. (2009). Solar driven nitrous acid formation on building material surfaces containing titanium dioxide: A concern for air quality in urban areas? *Atmospheric Environment, 43*(32), 5128-5131. doi:10.1016/j.atmosenv.2009.06.046

Legrand, M., Preunkert, S., Frey, M., Bartels-Rausch, T., Kukui, A., King, M. D., . . . Jourdain, B. (2014). Large mixing ratios of atmospheric nitrous acid (HONO) at Concordia (East Antarctic Plateau) in summer: a strong source from surface snow? *Atmospheric Chemistry and Physics, 14*(18), 9963-9976. doi:10.5194/acp-14-9963-2014

Lehmann. (2008). DOASIS tutorial. Germany.

Levy, H. (1972). Photochemistry of the lower troposphere (Vol. 21, pp. 575-591): Planet. Space Sci.

Li, S., Matthews, J., and Sinha, A. (2008). Atmospheric hydroxyl radical production from electronically excited NO2 and H2O. *Science, 319*(5870), 1657-1660. doi:10.1126/science.1151443

Logan, J. A. (1983). Nitrogen-oxides in the troposphere - global and regional budgets. *Journal of Geophysical Research-Oceans and Atmospheres, 88*(NC15), 785-807. doi:10.1029/JC088iC15p10785

Logan, J. A. (1989). Ozone in rural-areas of the United-States. *Journal of Geophysical Research-Atmospheres, 94*(D6), 8511-8532. doi:10.1029/JD094iD06p08511

Lyman, S., and Shorthill, H. (2013). *Final Report 2012 Uintah Basin Winter Ozone and Air Quality Study*. Retrieved from

Mack, J., and Bolton, J. R. (1999). Photochemistry of nitrite and nitrate in aqueous solution: a review. *Journal of Photochemistry and Photobiology a-Chemistry, 128*(1-3), 1-13. doi:10.1016/s1010-6030(99)00155-0

Madronich, S. (1987). Photodissociation in the atmosphere. 1. Actinic flux and the effects of ground reflections and clouds. *Journal of Geophysical Research-Atmospheres, 92*(D8), 9740-9752. doi:10.1029/JD092iD08p09740

Martin, R., Moore, K., Mansfield, M., Hill, S., Harper, K., and Shorthill, H. (2011). Final report: Uintah Basin winter ozone and air quality study, December 2010 - March 2011. (Vol. EDL/11-039). Utah: Energy Dynamics Laboratory, Utah State University Research Foundation.

Meller, R., and Moortgat, G. K. (2000). Temperature dependence of the absorption cross sections of formaldehyde between 223 and 323 K in the wavelength range 225-375 nm. *Journal of Geophysical Research-Atmospheres, 105*(D6), 7089-7101. doi:10.1029/1999jd901074

Min, K. E., Washenfelder, R. A., Dube, W. P., Langford, A. O., Edwards, P. M., Zarzana, K. J., . . . Brown, S. S. (2016). A broadband cavity enhanced absorption spectrometer for aircraft measurements of glyoxal, methylglyoxal, nitrous acid, nitrogen dioxide, and water vapor. *Atmospheric Measurement Techniques, 9*(2), 423-440. doi:10.5194/amt-9-423-2016

Ndour, M., D'Anna, B., George, C., Ka, O., Balkanski, Y., Kleffmann, J., . . . Ammann, M. (2008). Photoenhanced uptake of NO2 on mineral dust: Laboratory experiments and model simulations. *Geophysical Research Letters, 35*(5). doi:10.1029/2007gl032006

Olaguer, E. P., Rappengluck, B., Lefer, B., Stutz, J., Dibb, J., Griffin, R., . . . Pinto, J. P. (2009). Deciphering the Role of Radical Precursors during the Second Texas Air Quality Study. *Journal of the Air and Waste Management Association, 59*(11), 1258-1277. doi:10.3155/1047-3289.59.11.1258

Paulson, S., and Orlando, J. (1996). The reactions of ozone with alkenes: An important source of HOx in the boundary layer. *Geophysical Research Letters, 23*(25), 3727-3730.

Perner, D., and Platt, U. (1979). Detection of nitrous-acid in the atmosphere by Differential Optical-Absorption. *Geophysical Research Letters, 6*(12), 917-920. doi:10.1029/GL006i012p00917

Persson, P. O. G., Fairall, C. W., Andreas, E. L., Guest, P. S., and Perovich, D. K. (2002). Measurements near the Atmospheric Surface Flux Group tower at SHEBA: Near-surface

conditions and surface energy budget. *Journal of Geophysical Research-Oceans, 107*(C10). doi:10.1029/2000jc000705

Pinto, J. P., Dibb, J., Lee, B. H., Rappengluck, B., Wood, E. C., Levy, M., . . . Zheng, J. (2014). Intercomparison of field measurements of nitrous acid (HONO) during the SHARP campaign. *Journal of Geophysical Research-Atmospheres, 119*(9), 5583-5601. doi:10.1002/2013jd020287

Pitts, J. N., Sanhueza, E., Atkinson, R., Carter, W. P. L., Winer, A. M., Harris, G. W., and Plum, C. N. (1984). An investigation of the dark formation of nitrous-acid in environmental chambers. *International Journal of Chemical Kinetics, 16*(7), 919-939. doi:10.1002/kin.550160712

Platt, U. (1979). Dry deposition of SO2 - Reply. *Atmospheric Environment, 13*(7), 1065-1065. doi:10.1016/0004-6981(79)90028-3

Platt, U., and Stutz, J. (2008). *Differential optical absorption spectroscopy principles and applications Physics of earth and space environments,* (pp. xv, 597 p). Retrieved from SpringerLink. http://dx.doi.org/10.1007/978-3-540-75776-4

Rappenglueck, B., Ackermann, L., Alvarez, S., Golovko, J., Buhr, M., Field, R. A., . . . Keslar, C. (2014). Strong wintertime ozone events in the Upper Green River basin, Wyoming. *Atmospheric Chemistry and Physics, 14*(10), 4909-4934. doi:10.5194/acp-14-4909-2014

Ren, X., Sanders, J. E., Rajendran, A., Weber, R. J., Goldstein, A. H., Pusede, S. E., . . . Cohen, R. C. (2011). A relaxed eddy accumulation system for measuring vertical fluxes of nitrous acid. *Atmospheric Measurement Techniques, 4*(10), 2093-2103. doi:10.5194/amt-4-2093-2011

Roberts, J. M., Veres, P., Warneke, C., Neuman, J. A., Washenfelder, R. A., Brown, S. S., . . . de Gouw, J. (2010). Measurement of HONO, HNCO, and other inorganic acids by negative-ion proton-transfer chemical-ionization mass spectrometry (NI-PT-CIMS): application to biomass burning emissions. *Atmospheric Measurement Techniques, 3*(4), 981-990. doi:10.5194/amt-3-981-2010

Sakamaki, F., and Akimoto, H. (1988). HONO formation as unknown radical source in photocheical smog chdamber. *International Journal of Chemical Kinetics, 20*(2), 111-116. doi:10.1002/kin.550200204

Sakamaki, F., Hatakeyama, S., and Akimoto, H. (1983). Formation of nitrous acid and nitric oxide in the heterogeneous dark reaction of nitrogen dioxide and water vapor in a smog chamber. *International Journal of Chemical Kinetics, 15*(10), 1097-4601.

Saliba, N. A., Yang, H., and Finlayson-Pitts, B. J. (2001). Reaction of gaseous nitric oxide with nitric acid on silica surfaces in the presence of water at room temperature. *Journal of Physical Chemistry A, 105*(45), 10339-10346. doi:10.1021/jp012330r

Sander, S. P., Abbott, J., Barker, J. R., Burkholder, J. B., Fried, R. R., Golden, D. M., . . . Wine, P. H. (2011). Chemical Kinetics and Photochemical Data for Use in Atmospheric Studies (Evaluation No. 17 ed., Vol. 17, pp. 10 - 16). Jet Propulsion Laboratory, Pasadena: JPL Publication.

Schnell, R. C., Oltmans, S. J., Neely, R. R., Endres, M. S., Molenar, J. V., and White, A. B. (2009). Rapid photochemical production of ozone at high concentrations in a rural site during winter. *Nature Geoscience, 2*(2), 120-122. doi:10.1038/ngeo415

Serdyuchenko, A., Gorshelev, V., Weber, M., Chehade, W., and Burrows, J. P. (2014). High spectral resolution ozone absorption cross-sections - Part 2: Temperature dependence. *Atmospheric Measurement Techniques, 7*(2), 625-636. doi:10.5194/amt-7-625-2014

Sillman, S. (1999). The relation between ozone, NOx and hydrocarbons in urban and polluted rural environments. *Atmospheric Environment, 33*(12), 1821-1845. doi:10.1016/s1352-2310(98)00345-8

Simon, H., Kimura, Y., McGaughey, G., Allen, D. T., Brown, S. S., Osthoff, H. D., . . . Lee, D. (2009). Modeling the impact of ClNO2 on ozone formation in the Houston area. *Journal of Geophysical Research-Atmospheres, 114*. doi:10.1029/2008jd010732

Simpson, W. R., King, M. D., Beine, H. J., Honrath, R. E., and Petersen, M. C. (2002). Atmospheric photolysis rates during the Polar Sunrise Experiment ALERT2000 (vol 36, pg 2471, 2002). *Atmospheric Environment, 36*(36-37), 5749-5749. doi:10.1016/s1352-2310(02)00685-4

Soergel, M., Regelin, E., Bozem, H., Diesch, J. M., Drewnick, F., Fischer, H., . . . Zetzsch, C. (2011). Quantification of the unknown HONO daytime source and its relation to NO2. *Atmospheric Chemistry and Physics, 11*(20), 10433-10447. doi:10.5194/acp-11-10433-2011

Stanhill, G. (1969). A Simple Instrument for the Field Measurement of Turbulent Diffusion Flux. *Journal of Applied Meteorology, 8*, 509-513.

Stark, H., Brown, S. S., Wong, K. W., Stutz, J., Elvidge, C. D., Pollack, I. B., . . . Parrish, D. D. (2011). City lights and urban air. *Nature Geoscience, 4*(11), 730-731.

Stemmler, K., Ammann, M., Donders, C., Kleffmann, J., and George, C. (2006). Photosensitized reduction of nitrogen dioxide on humic acid as a source of nitrous acid. *Nature, 440*(7081), 195-198. doi:10.1038/nature04603

Stemmler, K., Ndour, M., Elshorbany, Y., Kleffmann, J., D'Anna, B., George, C., . . . Ammann, M. (2007). Light induced conversion of nitrogen dioxide into nitrous acid on submicron humic acid aerosol. *Atmospheric Chemistry and Physics, 7*(16), 4237-4248.

Stockwell, W. R., Kirchner, F., Kuhn, M., and Seefeld, S. (1997). A new mechanism for regional atmospheric chemistry modeling. *Journal of Geophysical Research-Atmospheres, 102*(D22), 25847-25879. doi:10.1029/97jd00849

Stoeckenius, T. (2015). Final Report 2014 Uinta Basin Winter Ozone Study (Vol. P-415-899-0700). California: Environ. http://www.deq.utah.gov/locations/U/uintahbasin/ozone/docs/2015/02Feb/UBWOS_2014_Final.pdf

Stoeckenius, T., & McNally, D. (2014). Final Report 2013 Uinta Basin Winter Ozone Study. http://www.deq.utah.gov/location/uintahBasin/studies/UBOS-2013.htm.

Stull, R. B. (1988). *An introduction to boundary layer meteorology*. Dordrecht ; Boston: Kluwer Academic Publishers.

Stutz, J., Alicke, B., Ackermann, R., Geyer, A., White, A., and Williams, E. (2004). Vertical profiles of NO3, N2O5, O-3, and NOx in the nocturnal boundary layer: 1. Observations during the Texas Air Quality Study 2000. *Journal of Geophysical Research-Atmospheres, 109*(D12). doi:10.1029/2003jd004209

Stutz, J., Alicke, B., and Neftel, A. (2002). Nitrous acid formation in the urban atmosphere: Gradient measurements of NO2 and HONO over grass in Milan, Italy. *Journal of Geophysical Research-Atmospheres, 107*(D22). doi:10.1029/2001jd000390

Stutz, J., Kim, E. S., Platt, U., Bruno, P., Perrino, C., and Febo, A. (2000). UV-visible absorption cross sections of nitrous acid. *Journal of Geophysical Research-Atmospheres, 105*(D11), 14585-14592. doi:10.1029/2000jd900003

Stutz, J., and Platt, U. (1996). Numerical analysis and estimation of the statistical error of differential optical absorption spectroscopy measurements with least-squares methods. *Applied Optics, 35*(30), 6041-6053. doi:10.1364/ao.35.006041

Su, H., Cheng, Y., Oswald, R., Behrendt, T., Trebs, I., Meixner, F. X., . . . Poeschl, U. (2011). Soil Nitrite as a Source of Atmospheric HONO and OH Radicals. *Science, 333*(6049), 1616-1618. doi:10.1126/science.1207687

Su, H., Cheng, Y. F., Shao, M., Gao, D. F., Yu, Z. Y., Zeng, L. M., . . . Wiedensohler, A. (2008). Nitrous acid (HONO) and its daytime sources at a rural site during the 2004 PRIDE-PRD experiment in China. *Journal of Geophysical Research-Atmospheres, 113*(D14). doi:10.1029/2007jd009060

Svensson, R., Ljungstrom, E., and Lindqvist, O. (1987). Kinetics of the reaction between nitrogen-dioxide and water-vapor. *Atmospheric Environment, 21*(7), 1529-1539. doi:10.1016/0004-6981(87)90315-5

Telford, J. W., and Businger, J. A. (1986). VonKarman constant in atmospehric boundary-layer flow - reevaluated - comments. *Journal of the Atmospheric Sciences, 43*(19), 2127-2130. doi:10.1175/1520-0469(1986)043<2127:cokcia>2.0.co;2

Thomas, J. L., Dibb, J. E., Huey, L. G., Liao, J., Tanner, D., Lefer, B., . . . Stutz, J. (2012). Modeling chemistry in and above snow at Summit, Greenland - Part 2: Impact of snowpack chemistry on the oxidation capacity of the boundary layer. *Atmospheric Chemistry and Physics, 12*(14), 6537-6554. doi:10.5194/acp-12-6537-2012

Thomas, J. L., Stutz, J., Lefer, B., Huey, L. G., Toyota, K., Dibb, J. E., and von Glasow, R. (2011). Modeling chemistry in and above snow at Summit, Greenland - Part 1: Model description and results. *Atmospheric Chemistry and Physics, 11*(10), 4899-4914. doi:10.5194/acp-11-4899-2011

Trainer, M., Williams, E. J., Parrish, D. D., Buhr, M. P., Allwine, E. J., Westberg, H. H., . . . Liu, S. C. (1987). Models and observations of the impact of natural hydrocarbons on rural ozone. *Nature, 329*(6141), 705-707. doi:10.1038/329705a0

Tsai, C., Wong, C., Hurlock, S., Pikelnaya, O., Mielke, L. H., Osthoff, H. D., . . . Stutz, J. (2014). Nocturnal loss of NOx during the 2010 CalNex-LA study in the Los Angeles Basin. *Journal of Geophysical Research-Atmospheres, 119*(22), 13004-13025. doi:10.1002/2014jd022171

Vandaele, A. C., Hermans, C., Simon, P. C., Carleer, M., Colin, R., Fally, S., . . . Coquart, B. (1998). Measurements of the NO2 absorption cross-section from 42 000 cm(-1) to 10 000 cm(-1) (238-1000 nm) at 220 K and 294 K. *Journal of Quantitative Spectroscopy and Radiative Transfer, 59*(3-5), 171-184. doi:10.1016/s0022-4073(97)00168-4

Vandaele, A. C., Simon, P. C., Guilmot, J. M., Carleer, M., and Colin, R. (1994). SO2 Absorption cross-section measurement in the UV using a Fourier-Transform spectrometer. *Journal of Geophysical Research-Atmospheres, 99*(D12), 25599-25605. doi:10.1029/94jd02187

VandenBoer, T. C., Brown, S. S., Murphy, J. G., Keene, W. C., Young, C. J., Pszenny, A. A. P., . . . Roberts, J. M. (2013). Understanding the role of the ground surface in HONO vertical structure: High resolution vertical profiles during NACHTT-11. *Journal of Geophysical Research-Atmospheres, 118*(17), 10155-10171. doi:10.1002/jgrd.50721

VandenBoer, T. C., Markovic, M. Z., Petroff, A., Czar, M. F., Borduas, N., and Murphy, J. G. (2012). Ion chromatographic separation and quantitation of alkyl methylamines and ethylamines in atmospheric gas and particulate matter using preconcentration and suppressed conductivity detection. *Journal of Chromatography A, 1252*, 74-83. doi:10.1016/j.chroma.2012.06.062

VandenBoer, T. C., Markovic, M. Z., Sanders, J. E., Ren, X., Pusede, S. E., Browne, E. C., . . . Murphy, J. G. (2014). Evidence for a nitrous acid (HONO) reservoir at the ground surface in Bakersfield, CA, during CalNex 2010. *Journal of Geophysical Research-Atmospheres, 119*(14), 9093-9106. doi:10.1002/2013jd020971

VandenBoer, T. C., Young, C. J., Talukdar, R. K., Markovic, M. Z., Brown, S. S., Roberts, J. M., and Murphy, J. G. (2015). Nocturnal loss and daytime source of nitrous acid through reactive uptake and displacement. *Nature Geoscience, 8*(1), 55-60. doi:10.1038/ngeo2298

Veres, P., Roberts, J. M., Warneke, C., Welsh-Bon, D., Zahniser, M., Herndon, S., . . . de Gouw, J. (2008). Development of negative-ion proton-transfer chemical-ionization mass spectrometry (NI-PT-CIMS) for the measurement of gas-phase organic acids in the atmosphere. *International Journal of Mass Spectrometry, 274*(1-3), 48-55. doi:10.1016/j.ijms.2008.04.032

Villena, G., Wiesen, P., Cantrell, C. A., Flocke, F., Fried, A., Hall, S. R., . . . Kleffmann, J. (2011). Nitrous acid (HONO) during polar spring in Barrow, Alaska: A net source of OH radicals? *Journal of Geophysical Research-Atmospheres, 116*. doi:10.1029/2011jd016643

Voigt, S., Orphal, J., and Burrows, J. P. (2002). The temperature and pressure dependence of the absorption cross-sections of NO2 in the 250-800 nm region measured by Fourier-transform spectroscopy. *Journal of Photochemistry and Photobiology a-Chemistry, 149*(1-3), 1-7. doi:10.1016/s1010-6030(01)00650-5

Volkamer, R., Sheehy, P., Molina, L. T., and Molina, M. J. (2010). Oxidative capacity of the Mexico City atmosphere - Part 1: A radical source perspective. *Atmospheric Chemistry and Physics, 10*(14), 6969-6991. doi:10.5194/acp-10-6969-2010

Wang, S., Ackermann, R., and Stutz, J. (2006). Vertical profiles of O-3 and NOx chemistry in the polluted nocturnal boundary layer in Phoenix, AZ: I. Field observations by long-path DOAS. *Atmospheric Chemistry and Physics, 6*, 2671-2693.

Williams, J., Roberts, J. M., Bertman, S. B., Stroud, C. A., Fehsenfeld, F. C., Baumann, K., . . . Williams, E. J. (2000). A method for the airborne measurement of PAN, PPN, and MPAN. *Journal of Geophysical Research-Atmospheres, 105*(D23), 28943-28960. doi:10.1029/2000jd900373

Wong, K. W., Tsai, C., Lefer, B., Grossberg, N., and Stutz, J. (2013). Modeling of daytime HONO vertical gradients during SHARP 2009. *Atmospheric Chemistry and Physics, 13*(7), 3587-3601. doi:10.5194/acp-13-3587-2013

Wong, K. W., Tsai, C., Lefer, B., Haman, C., Grossberg, N., Brune, W. H., . . . Stutz, J. (2012). Daytime HONO vertical gradients during SHARP 2009 in Houston, TX. *Atmospheric Chemistry and Physics, 12*(2), 635-652. doi:10.5194/acp-12-635-2012

Wu, T., Chen, W., Fertein, E., Cazier, F., Dewaele, D., and Gao, X. (2012). Development of an open-path incoherent broadband cavity-enhanced spectroscopy based instrument for simultaneous measurement of HONO and NO2 in ambient air. *Applied Physics B-Lasers and Optics, 106*(2), 501-509. doi:10.1007/s00340-011-4818-3

Young, C. J., Washenfelder, R. A., Roberts, J. M., Mielke, L. H., Osthoff, H. D., Tsai, C., . . . Brown, S. S. (2012). Vertically Resolved Measurements of Nighttime Radical Reservoirs; in Los Angeles and Their Contribution to the Urban Radical Budget. *Environmental Science and Technology, 46*(20), 10965-10973. doi:10.1021/es302206a

Zhang, N., Zhou, X., Shepson, P. B., Gao, H., Alaghmand, M., and Stirm, B. (2009). Aircraft measurement of HONO vertical profiles over a forested region. *Geophysical Research Letters, 36*. doi:10.1029/2009gl038999

Zheng, W., Flocke, F. M., Tyndall, G. S., Swanson, A., Orlando, J. J., Roberts, J. M., . . . Tanner, D. J. (2011). Characterization of a thermal decomposition chemical ionization mass spectrometer for the measurement of peroxy acyl nitrates (PANs) in the atmosphere. *Atmospheric Chemistry and Physics, 11*(13), 6529-6547. doi:10.5194/acp-11-6529-2011

Zhou, X., Zhang, N., TerAvest, M., Tang, D., Hou, J., Bertman, S., . . . Stevens, P. S. (2011). Nitric acid photolysis on forest canopy surface as a source for tropospheric nitrous acid. *Nature Geoscience, 4*(7), 440-443. doi:10.1038/ngeo1164

Zhou, X. L., Beine, H. J., Honrath, R. E., Fuentes, J. D., Simpson, W., Shepson, P. B., and Bottenheim, J. W. (2001). Snowpack photochemical production of HONO: a major source of OH in the Arctic boundary layer in springtime. *Geophysical Research Letters, 28*(21), 4087-4090. doi:10.1029/2001gl013531

Zhou, X. L., Civerolo, K., Dai, H. P., Huang, G., Schwab, J., and Demerjian, K. (2002). Summertime nitrous acid chemistry in the atmospheric boundary layer at a rural site in New York State. *Journal of Geophysical Research-Atmospheres, 107*(D21). doi:10.1029/2001jd001539

Zhou, X. L., Gao, H. L., He, Y., Huang, G., Bertman, S. B., Civerolo, K., and Schwab, J. (2003). Nitric acid photolysis on surfaces in low-NOx environments: Significant atmospheric implications. *Geophysical Research Letters, 30*(23). doi:10.1029/2003gl018620